DISSERTATION

MULTI-SCALE TRAFFIC PERFORMANCE MODELING OF TRANSPORTATION SYSTEMS SUBJECTED TO MULTIPLE HAZARDS

Submitted by

Guangyang Hou

Department of Civil and Environmental Engineering

In partial fulfillment of the requirements

For the Degree of Doctor of Philosophy

Colorado State University

Fort Collins, Colorado

Fall 2019

Doctoral Committee:

Advisor: Suren Chen

John van de Lindt
Rebecca Atadero
Craig Trumbo

ABSTRACT

MULTI-SCALE TRAFFIC PERFORMANCE MODELING OF TRANSPORTATION SYSTEMS SUBJECTED TO MULTIPLE HAZARDS

Transportation systems are very vulnerable to natural or manmade hazards, such as earthquakes, floods, hurricanes, tsunamis, terrorism, etc. In the past years, extreme hazards have caused significant physical and functional damages to transportation systems around the world. Disruption of transportation systems by multiple hazards will impede social and commercial activities, and hamper the post-disaster emergency response and long-term recovery of the damaged community. The main purpose of this dissertation is to develop advanced performance assessment techniques of transportation systems subjected to multiple hazards in the link level and network level. It is expected that the developed techniques in this dissertation will help stakeholders to make risk-informed decisions in terms of effective prevention and preparation measures to enhance and facilitate resilience of transportation systems. A suite of simulation methodologies are developed to evaluate the performance of critical transportation components (e.g. bridges and road segments) and transportation networks subjected to multiple hazards in this dissertation. Firstly, an advanced traffic flow simulation framework is developed to predict the post-hazard performance of a typical highway system under hazardous conditions. Secondly, a simulation methodology is developed to study the traffic performance of degraded road links being partially blocked following extreme events. Thirdly, a new approach is proposed to develop travel time functions of partially blocked roads in urban areas through microscopic traffic simulation. Fourthly, an integrated model is developed to assess single-vehicle traffic

safety performance of stochastic traffic flow under hazardous driving conditions. Finally, an integrated probabilistic methodology is developed to model the performance of disrupted infrastructures due to fallen urban trees subjected to extreme winds.

ACKNOWLEDGEMENTS

I would first like to express my great gratitude to my advisor Dr. Suren Chen, for his consistent guidance, patience and encouragement throughout my PhD study. I appreciate him for giving me the opportunity to work on my dissertation research projects. He has been a great mentor and a good friend over the past five years. His invaluable advice and unconditional support helped me overcome many difficulties in my research and life. Without his excellent supervision, this dissertation would not have been possible.

I am also thankful to the distinguished committee members, Dr. John van de Lindt, Dr. Rebecca Atadero and Dr. Craig Trumbo. Their invaluable suggestions and comments have greatly improved the quality of this dissertation.

I would also like to thank my former and current fellow graduate students at Colorado State University, Dr. Yufen Zhou, Dr. Xiaoxiang Ma, Luke Chen, Yangyang Wu, Qiling Zou, Shangbo Tong, Jingze Ren, Wei Liang, et al. It was my great pleasure and honor to study and work with them at CSU. Their excellent expertise and scientific attitude in doing research have influenced me a lot. My special thanks also go to Dr. Huoyue Xiang for his advice in my research direction, and Dr. Yulong Bao for his assistance in data collection.

I also like to acknowledge the financial support for my research provided by the Center for Risk-based Community Resilience Center sponsored by National Institute of Standards and Technology (NIST) (Award No. 70NANB15H044), and the Mountain-Plains Consortium, a University Transportation Center funded by the U.S. Department of Transportation.

Last but not the least, I would like to thank my parents and parents-in-law for their support financially and emotionally. My deepest and heartfelt gratitude goes to my wife, Sufang and my two children, Elsa and Eric for their continuous support, encouragement, accompany and love.

DEDICATION

To my wife Sufang

for her love and devotion to our family

TABLE OF CONTENTS

LIST OF TABLES

LIST OF FIGURES

CHAPTER 1 INTRODUCTION

1.1 Background

Transportation systems play an important role in modern society by providing the movement of people and goods between different places, and therefore have significant influence on the political, social, economic development of nations. About 11% of income of Americans is spent on transportation, which directly contributes about 10% of the gross domestic product of US (BTS 2017). However, with development of urban cities and fast growth of population and vehicles, transportation-related problems (e.g. traffic congestion, vehicle accidents and air pollution) are becoming increasingly serious throughout the world. It becomes a primary concern for city planners and traffic engineers to develop efficient, safe, and convenient transportation systems.

Transportation systems are very vulnerable to natural or manmade hazards, such as earthquakes, floods, hurricanes, tsunamis, terrorism, etc. In the past years, extreme hazards, such as 2004 Indian Ocean tsunami in Indonesia, 2005 Hurricane Katrina in the USA, 2008 Sichuan earthquake in China, and 2010 Haiti earthquake in Haiti, have caused significant physical and functional damages to transportation systems around the world. Transportation systems play a vital role before, during and after hazards by evacuating people and supporting emergency response and various post-hazard restoration efforts. Disruption of transportation systems will not only affect the emergency and rescue operations immediately after hazards, but also inhibit the effort to restore other lifeline infrastructures (e.g. transmission lines, water pipes), and further aggravate the loss of impacted communities. Therefore, it is imperative to develop efficient tools to model the impact of hazards through performance evaluations so that the stakeholders can make risk-informed decisions in terms of effective prevention and preparation measures to reduce the risk and vulnerability of transportation systems and further improve the resilience of the whole community subjected to hazards.

1.2 Literature review

1.2.1 Traffic flow theory and modeling

1.2.1.1 Traffic flow characteristics

Traffic flow theory describes the interactions between the vehicles and infrastructure in a mathematical way. Traffic flow theory and modeling started in 1930s by Bruce Greenshields (Greenshields 1934, 1935). However, with the rapid development of computing power and significant increase of traffic demand, traffic flow theory and modeling have received enormous attention since the 1990s (Treiber and Kesting 2013).

In the microscopic level, a time-space diagram shows graphically the movement of individual vehicles in a traffic flow in both space and time (Fig. 1.1). Typically, time is displayed along the horizontal axis, and distance is shown along the vertical axis. Each line in the time-space diagram represents the trajectory of an individual vehicle. Vehicles follow each other along a lane, so there are a number of parallel trajectories in a time-space diagram. The slope of a trajectory line is the instantaneous speed of the vehicle. Curved parts of a trajectory indicate there are speed variations due to vehicle acceleration or deceleration.

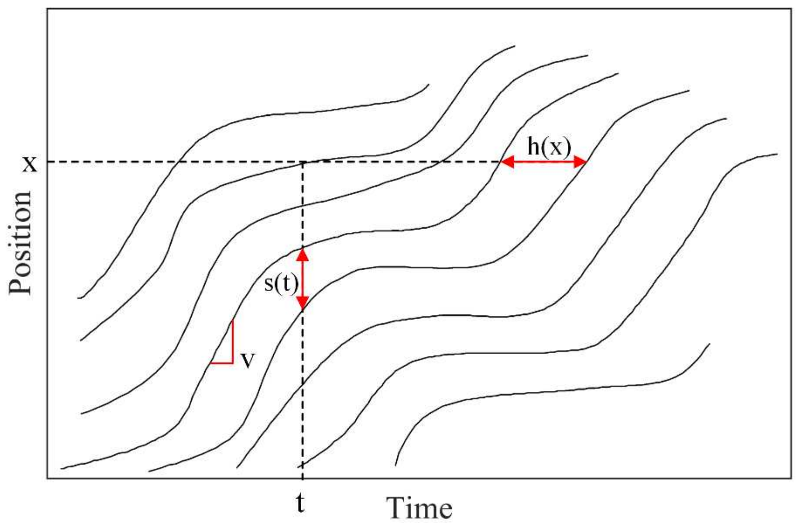

Figure 1.1 Time-space diagram

In the macroscopic level, traffic flow can be described with three main variables: speed, density and flow. Because it is hard to measure the speed of every vehicle in traffic accurately, it is common to obtain the average speed of some sample vehicles. Time mean speed and space mean speed are two commonly used average speeds. The time-mean speed is the arithmetic average speed of all vehicles for a specified period of time (Eq. (1.1)). In practice, it is measured at a reference point on the roadway. For example, loop detectors are usually used to detect vehicles passing a certain point and measure their speeds. The space-mean speed is the average speed of vehicles traveling a given segment of roadway during a specified period of time, which is calculated with the roadway segment length and average travel time (Eq. (1.2)). For example, Bluetooth technology has been recently used to collect vehicle travel time in a roadway segment by tracking the Bluetooth ID of passing vehicles. An average travel time is calculated from individual vehicle travel times. Then, the space mean speed is computed by dividing the distance between two Bluetooth devices by the average travel time.

$$v_t = \frac{1}{m}\sum v_i \tag{1.1}$$

$$v_s = \frac{L}{\frac{\sum t_i}{m}} = \frac{L*m}{\sum t_i} \tag{1.2}$$

where v_t is the time mean speed; v_s is the space mean speed; m is the number of observations; v_i is the speed of the ith vehicle; L is the length of roadway segment; t_i is the travel time of the ith vehicle. The time-mean speed is associated with a point over time, whereas the space-mean speed is associated with a section of roadway.

Density is defined as the number of vehicles observed on a unit length of road, which is expressed by Eq. (1.3). Density can also be expressed by the inverse of spacing with Eq. (1.4), which is the distance between two vehicles.

$$\rho = \frac{N}{L} \tag{1.3}$$

$$\rho = \frac{1}{\bar{s}} \tag{1.4}$$

where ρ is density; N is the number of observed vehicles; L is the road length; $\bar{s}$ is the average spacing between two adjacent vehicles.

Flow is defined as the number of vehicles passing a reference point per unit of time, which has a common unit of vehicles per hour. The inverse of flow is time headway, which corresponds to the time between passages of the front ends of two successive vehicles, as shown Eq. (1.5). There is a relationship between flow, speed and density given in Eq. (1.6), which is called the fundamental equation. It can be seen from Eq. (1.6) that the flow depends on both the speed and density.

$$q = \frac{1}{h} \tag{1.5}$$

$$q = v * \rho \tag{1.6}$$

where q is flow; h is time headway; v is speed.

Fundamental diagrams, as shown in Fig. 1.2 (Immers and Logghe 2002), describe the relationship between speed, flow, and density of traffic, which are primary tools to study traffic flow. There are three different two-dimensional graphs consisted in fundamental diagrams: flow-density, speed-flow, and speed-density. A diagram describes the relationship between two of three variables and the third variable can always be recovered by means of Eq. (1.6). Typically, fundamental diagrams are developed by plotting observed field data points and fitting those data points with mathematical expressions. Many mathematical models have been developed for the fundamental diagrams, such as Greenshield model, triangular shaped model (Elefteriadou 2014).

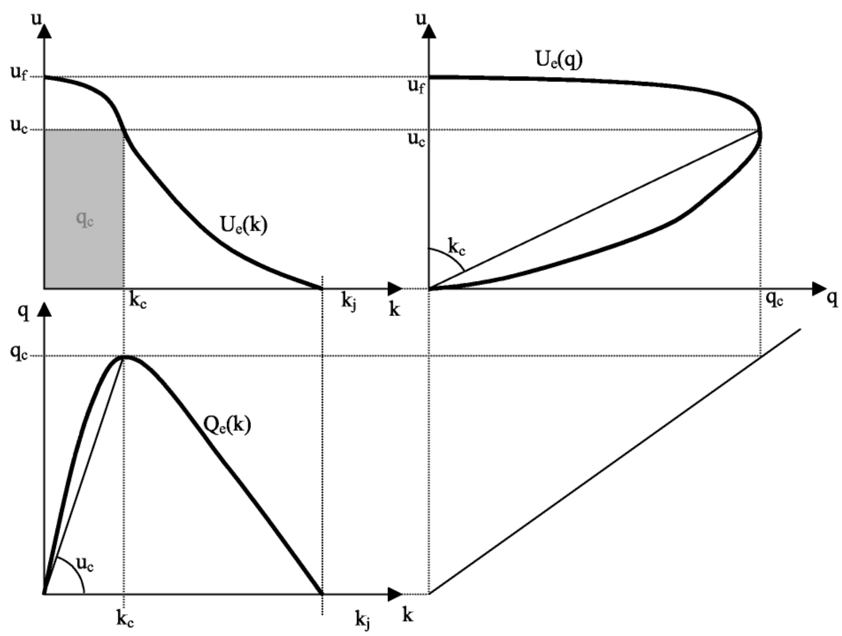

Figure 1.2 Fundamental diagrams (Immers and Logghe 2002)

1.2.1.2 <u>Traffic flow simulation</u>

Generally, traffic flow simulation model can be classified into two types: macroscopic and microscopic simulation models. Macroscopic models regard traffic flow as liquids or gases in motion by assuming the aggregate homogeneous behavior of drivers. In contrast, microscopic simulation examines traffic flow by modeling the behavior of individual vehicles. In microscopic models, each vehicle and its driver are treated as a single unit, whose movement is replicated by considering dynamic interactions with surrounding traffic. Car-following model and cellular automaton (CA) model are two famous microscopic models. Many microscopic simulation programs have been developed and widely used for traffic analysis, such as VISSIM, SUMO, TRANSIMS, CORSIM, AIMSUN, INTEGRATION, Paramics and SimTraffic.

As a stochastic microscopic traffic flow simulation model, CA model is able to simulate the traffic flow realistically. Because of its high efficiency and simplicity, CA model is one of the most widely used microscopic traffic simulation methods. At each time step, the velocity and position of each vehicle are updated through the single-lane forwarding rules (i.e. acceleration, deceleration, random brake, and movement) and the lane-changing rules. Fig. 1.3 shows the forwarding rules in the well-known one-lane NaSch's CA model (Nagel and Schreckenberg 1992).

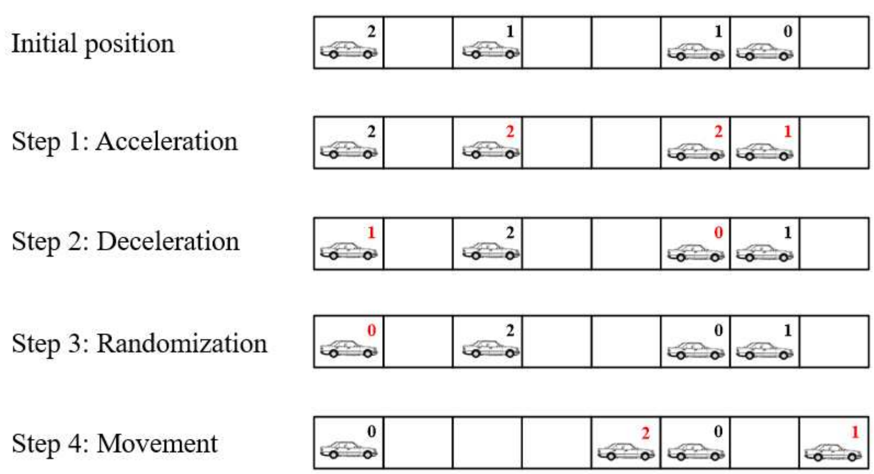

Figure 1.3 Forwarding rules in the one-lane NS CA model

1.2.2 Simulation of traffic flow under hazardous driving conditions

A typical highway system consists of bridges, connecting roadways and moving traffic. For many years, simulation of the traffic moving over a bridge had been greatly simplified. In many studies, a single vehicle, uniformly distributed vehicle platoon or random vehicle pattern with the assumption of certain distributions were often adopted for both short- and long-span bridges (Cai and Chen 2004; Chen and Cai 2007; Xu and Guo 2003; O'Connor and O'Brien 2005). It was not until recently that advanced traffic flow simulation on a microscopic scale has been adopted in the field of bridge engineering by offering detailed time-dependent vehicle information and considering realistic traffic rules and speed limits. For example, the CA traffic flow simulation technique was adopted to study the live load on a long-span bridge from the stochastic traffic (Chen and Wu 2011) and applied on investigating the dynamic performance of the bridge (Chen and Wu 2010; Zhou and Chen 2015a). As the first-time effort on incorporating microscopic traffic flow simulation in studying bridge performance, such a model (Chen and Wu 2011) was primarily developed for normal driving conditions.

Moving vehicles in a highway system do not only impose external loads on the infrastructure (i.e. bridges) from the vehicle self-weight, but also in the meantime, are supported by the infrastructure to stay safe and move smoothly. The resilience of a highway system subjected to various hazards depends on not only post-hazard integrity of infrastructure, but also safe driving of vehicles through the system during and immediately after hazards (Chen and Chen 2010). On the one hand, post-hazard traffic by panicking drivers can easily cause local congestion and concentrating loads on bridges. Although such load concentration may not be critical to bridges in normal conditions, it may be disastrous to those bridges that have already been severely damaged by hazards. On the other hand, the accident risks of vehicles following hazards may considerably increase because of more irrational driving behavior and traffic congestion. These accidents may further cause severe congestion and traffic disruption, which can be critical to the emergency response and evacuation efforts through the highway system.

In recent years, based on the well-known NaSch's model (Nagel and Schreckenberg 1992), several extended CA models have been introduced to incorporate more realistic driving behaviors. Li et al. (2006) revised the symmetric lane-changing rules (Chowdhury et al. 1997) to take into account the aggressive lane-changing behavior of fast vehicles. Xie and Zhao (2013) considered different driving behaviors in the deceleration step by anticipating the velocity of the preceding vehicle. Zamith et al. (2015) used the probability density function of the Beta distribution to model three types of driving behavior when determining the effective distance and effective velocity of a vehicle at next time step. Zhao et al. (2016) defined aggressive driving behavior with larger maximum speed and higher lane-changing probability.

1.2.3 Simulation of disrupted traffic flow

Following some natural hazards, transportation systems play a critical role in evacuating people and supporting emergency response and various post-hazard restoration efforts. In addition to direct impacts from hazards (e.g. damaged bridges or roads), post-hazard traffic networks are often disrupted due to those indirect impacts originated from interdependent nature with other infrastructure systems and environments (Ouyang 2014; Fotouhi et al. 2017; Edrissi et al. 2015). For example, traffic networks especially those in urban areas may suffer from blockage of debris from adjacent buildings, fallen trees or light poles (Anastassiadis and Argyroudis 2007; Argyroudis et al. 2015). In addition to long-term (e.g. bridge or pavement damage) and short-term disruptions (e.g. major debris) following natural hazards, some minor incidents (e.g. vehicle accidents) can also fully or partially block the roads temporarily, causing considerable traffic delay (Calvert and Snelder 2015). A rational prediction of traffic performance of degraded roads, such as travel capacity, speed and delay, is critical to hazard resilience research of not only individual transportation networks but also the whole community (Sullivan et al. 2009; Mattsson and

Jenelius 2015).

In contrast to abundant historical traffic data under normal conditions, one primary challenge for degraded roads is that existing post-hazard traffic data on disrupted scenarios are very rare and simulation-based approaches have become the primary option. Different from traffic studies on intact roads which have been extensively explored, existing traffic simulations on disrupted roads with sufficient details are very limited and most were focused on the connectivity studies about fully-blocked scenarios. Following some natural hazards, some partially-blocked roads and bridges often remain open to vehicles supporting emergency response, early recovery, evacuation and general traffic. Due to the limited resources following some major hazards, clearing some debris from all roads in a community often take days to months. In addition, some critical bridges with minor or moderate damages may open a limited number of lanes following hazards to maximize the emergency response, recovery and evacuation efficiency. For all these scenarios with degraded roads and bridges following some extreme events, traffic capacity and travel time are very different from those with intact road infrastructure, which can only be rationally predicted in a microscopic scale.

During the past years, there have been some limited simulation-based studies of disrupted traffic flow in a microscopic scale with CA models and car-following models (Huang and Huang 2002; Pottmeier et al. 2002). These studies include multi-lane traffic flow simulation with a partially closed lane induced by various traffic bottlenecks, e.g., accidents, work zone, and lane reduction (Kurata and Nagatani 2003; Nassab et al. 2006; Zhu et al. 2009; Jia et al. 2003Hou and Chen 2019a). Lan et al. (2009) proposed a CA model with piecewise-linear speed variation and limited deceleration and implemented the model to simulate the traffic flow at highway work zone. Various traffic control schemes (e.g. setting various reduced speed limits and reduced speed zone lengths) were investigated.

Chen et al. (2014) investigated the influence of car accident location on three-lane traffic flow. In the study by Weng and Meng (2011), the randomization probability parameter in their CA model was formulated as a function of some parameters related to the work zone based on the calibration data sets, and the model was validated with the work zone data microscopically and macroscopically. To simulate realistic merging behaviors in a work zone, Fei et al. (2016) applied different lane-changing rules and position update rules for vehicles in different areas, i.e., the normal area, merging area, and work zone.

1.2.4 Travel time function for disrupted urban arterials

Travel time functions are usually developed based on measured or simulated traffic data. It is a traditional approach to estimate travel time functions by calibrating empirical travel time models based on observed traffic data (Davis and Xiong 2007), which can be collected with various techniques, such as floating car, license plate matching, ITS probe vehicle, loop detector and radar (Gastaldi and Rossi 2011). In addition to the well-known Bureau of Public Roads (BPR) function, there are other common empirical travel time estimate models, such as conical travel time function, Akcelik model, Singapore model, Skabardonis-Dowling model and HCM formula (Moses et al. 2013). Mtoi and Moses (2014) calibrated four volume delay functions with archived detector data for different facility types (e.g. freeway, toll road, HOV lane, and arterial). It was found in their study that each volume delay function is suitable for a particular facility type. Kucharski and Drabicki (2017) estimated the travel time function of a three-lane arterial road by calibrating the BPR function with field data collected by a loop detector. Zhang and Waller (2018) studied the link performance function for contiguous High Occupancy Vehicle (HOV) lanes on freeways with real traffic data.

However, it is often very difficult and expensive to gather real traffic data under all different traffic conditions, such as various volumes and vehicle compositions. With the rapid development of computing power and computing technology, many microscopic traffic simulation models have been developed to provide an alternative to collected data. Microscopic traffic simulators, such as VISSIM, SUMO, TRANSIMS, CORSIM, AIMSUN, INTEGRATION, Paramics and SimTraffic, are popular for generating traffic data under various conditions, which otherwise cannot be easily obtained through data collection in real world (Tian et al. 2002). Several researchers developed travel time functions based on the simulated traffic data. Lu (2010) proposed an analytical travel time function for urban arterials and calibrated the parameters based on microscopic simulation data from CORSIM. Lu et al. (2016) estimated travel time functions for different vehicle types in heterogeneous freeway traffic flow based on the simulated data with VISSIM.

Compared to freeways, travel time on arterials is influenced by more factors, such as traffic signals, lane width, lane utilization, parking maneuvers, and pedestrians. Travel time on an arterial link includes running time and signal delay. Since the total link travel time is significantly affected by the signal delay, traffic signal information such as cycle length, effective green ratio and vehicle arrival type should be considered when estimating travel time on arterials. Travel time functions of arterials have been investigated extensively in several existing studies: speed-flow functions of urban arterials with four classes were developed based on the micro-simulation results by Yun et al. (2005). Davis and Xiong (2007) evaluated several travel time models with measured field data of 50 arterial links in Twin cities. Kajalic et al. (2018) examined several traffic time models of urban streets (e.g. Akcelik model, HCM model, Singapore model, and BPR function) and found the Akcelik model had the best performance in estimating travel time for road sections with a high number of signals.

Accounting for a considerable portion of urban traffic, trucks in heterogeneous traffic flow often significantly contribute to traffic delay due to their different sizes, travel speeds, mechanical properties, and headways from cars. Previous studies indicate that the flow rate and speed decrease with the increase of truck ratio (Li et al. 2016). The standard BPR function does not reflect the effect of traffic flow heterogeneity caused by different vehicle types on traffic congestion. The conversion of trucks into cars by using the passenger car equivalent method only recognizes the size difference but ignores the operational difference between those vehicle types. Truck's impact on the traffic time function has been included in some previous researches (Lu et al. 2016; Muller and Schiller 2015; Yun et al. 2005).

Blockage size is another factor that affects the performance of PBR, which has been preliminarily considered in existing studies. For example, lateral and longitudinal blockage sizes have been incorporated in the empirical equations to calculate the remaining traffic capacity (Adeli and Jiang 2003). Blockage size (e.g. work zone length) has been found to directly influence the travel time required for a vehicle to transverse a road (Cassidy and Han 1993). Given various possible blockage scenarios following different hazards, to incorporate the effect of the blockage size in travel time function can be challenging, but crucial for more rationally evaluating the post-hazard performance of disrupted transportation networks by considering the interaction between roads and other interdependent infrastructures.

Several studies have considered the impact of PBR in the post-hazard urban transportation network analysis, most of which focused on the connectivity analysis of disrupted transportation networks with fully- and partially-closed roads (Argyroudis et al. 2015; Goretti and Sarli 2006; Zanini et al. 2017). Only a few studies took into account the effect of PBR on traffic delay by modeling the post-hazard traffic demand. Tamima and Chouinard (2017) evaluated system vulnerability of transportation networks after earthquakes and considered road closure due to fallen debris from damaged buildings. The reduced capacity of PBR was estimated by assuming there is a linear relationship between the remaining capacity and the percentage of the road width being covered by debris. However, the travel time on PBR in this study was calculated by the standard BPR function including the normal free-flow time and reduced capacity rather than realistic travel time functions for disrupted scenarios of PBR.

Despite the essential role of travel time of PBR for the resiliency analysis of disrupted transportation networks, extensive literature review has not identified any published literature regarding travel time functions of PBR. One big challenge for developing travel time functions of PBR is the unavailability of real traffic data. As discussed earlier, microscopic traffic simulation can become a good alternative. Among those existing microscopic traffic simulation models, CA model is one of the most widely used models, thanks to its high efficiency and flexibility (Hou et al. 2017). Many existing studies investigated disrupted traffic flow on PBR induced by tollbooths, accidents, lane reduction, and work zone with CA models (Fei et al. 2016; Huang and Huang 2002; Jia et al. 2003; Kurata and Nagatani 2003; Meng and Weng 2011; Nassab et al. 2006; Pottmeier et al. 2002; Zhu et al. 2009; Hou, Chen and Han 2019).

In spite of recent effort towards realistic simulation of disrupted traffic, one major challenge for CA-based traffic flow simulation is about unrealistic deceleration behavior. There are generally two types of unrealistic deceleration behavior in existing CA models for disrupted traffic. Firstly, when a vehicle approaches a static obstruction or traffic jam, it may make a sudden stop by sharply reducing its maximum velocity in order to avoid a rear-end crash. In this situation, the required deceleration rate is much higher than the mechanical deceleration capability by most vehicles, making the deceleration rate unrealistic. This is caused by some limitations of most existing models: vehicle's velocity is determined only by the gap between itself and its preceding vehicle, and vehicles tend to brake abruptly at the last second. Secondly, on a disrupted road, when a vehicle enters the merging area before an obstruction, it usually decelerates gradually to a safe speed (e.g. posted reduced speed limit). However, such a deceleration process would be completed regardless within 1 second in existing CA models, which may lead to an unrealistically high deceleration rate. Although unrealistic driving behavior may still lead to reasonable long-term averaged cumulative outcome for normal traffic flow, it may cause erratic local results for disrupted traffic flow which are important for PBR performance. Lan et al. (2009) improved the CA model with piecewise-linear speed variation to avoid the first type of unrealistic deceleration behaviors in the work zone traffic simulation. However, the second type of unrealistic deceleration behavior still existed in their model. Therefore, a general CA-based model for simulation of disrupted traffic flow that can fully consider realistic deceleration driving behavior is still needed.

1.2.5 Vehicle accident simulation in adverse conditions

Under some adverse driving conditions (i.e. strong crosswind, icy or snowy road surface), vehicles often experience increased risks of single-vehicle accidents, such as rollover or sideslip accidents (Baker 1994; Chen and Cai 2004). Past three decades have witnessed considerable amount of research efforts on single-vehicle accidents with several deterministic and probabilistic accident assessment models being developed such as those by Baker (1986, 1987, 1991, 1994), Sampson (2000), Gaspar et al. (2004, 2005) and Batista and Perkovic (2014), among many others. In these studies, a single-unit vehicle was typically modeled with multiple connected mass units, dampers and springs. By considering some typical adverse environments such as icy/snowy/wet road surface conditions, crosswinds and road curvature, Chen and

Chen (2010) developed a new single-vehicle accident simulation model. In the study, more comprehensive dynamic interactions between vehicles, excitations and environments were considered along with some new accident criteria developed based on the characterizations of the transient process of rollover and sideslip accidents. Recently, Wang et al. (2016) proposed a nonlinear safety assessment model for vehicles moving on the ground under a sudden crosswind. Different from linear models, the wind loads and the mass moments vary with the angular displacements of the vehicle in a nonlinear way (Wang et al. 2016).

Based on the deterministic vehicle accident models, a few probabilistic models were also developed to consider uncertainties of critical variables, such as vehicle parameters, vehicle speed, wind velocity, coefficient of friction on roads, and superelevation (Snaebjornsson et al. 2007; Chen and Chen 2011; You et al. 2012; Shin and Lee 2014, 2015; Kim et al. 2016). Compared to road vehicles on roadways, those on long-span bridges under hazardous driving environments are usually more vulnerable to single-vehicle accidents due to the dynamic interactions (Deng et al. 2015; Deng and Cai 2010; Cai and Chen 2004) and more open environments. Several researchers have investigated single-vehicle safety of vehicles on long-span bridges (Chen and Cai 2004; Guo and Xu 2006; Chen et al. 2015; Wang and Xu 2015; Zhou and Chen 2015b; Ma et al. 2015).

1.2.6 Probabilistic modeling of disrupted infrastructures due to fallen trees

Tree failures due to strong winds in both forest and urban areas cause extensive direct and indirect economic and environmental losses. Wind damage to managed forests leads to huge loss of timber yield. For example, storm Martin in 1999 in southwest France caused estimated losses of 26.1 million m^3 of wood, which is about 3.5 years of harvest in that area (Cucchi et al. 2004). In urban areas, the destructions of trees under extreme winds result in considerably more indirect loss and disruptions to human life and infrastructures than the direct economic loss of fallen trees. Fallen trees due to extreme winds may threaten human safety, damage buried water pipes and buildings, cause power outage of overhead powerlines or block transportation routes. All these can seriously jeopardize the resilience of an urban community facing various wind hazards, hamper post-hazard evacuation and rescue operations, and delay critical recovery efforts. For instance, the Great Storm in 1987 caused at least 13 deaths in England, most of whom were killed by fallen trees (Mitchell et al. 1989). After hurricane Isabel in 2003, it took 84 days to remove the tree debris with a total amount of 52,865 m3 from roads in Bertie County, North Carolina (Laefer and Pradhan 2006). In hurricane Katrina and Rita in 2005, uprooting of trees due to high winds was the main cause of the damage to the buried water and wastewater pipes in some cities of Louisiana (Chisolm and Matthews 2012). It is therefore very important to develop an efficient risk assessment tool to predict and further reduce the disruptions to critical infrastructures caused by fallen trees in future wind events.

Over the last decades, some models have been developed to predict the risk of tree failure under strong winds, which can be categorized as two main types: statistical models and mechanistic models. Statistical models can predict the windthrow probability and identify key factors associated with wind damage (Lavoie et al. 2012). However, these models are unable to provide evidence of actual damage mechanism and also hard to be generalized for other locations and environments. Although mechanistic models need some modeling simplifications and supporting empirical relationships, they can provide clear understanding of windthrow mechanism by linking the wind events and tree's performance. Several developed mechanistic models have been widely adopted in the research community for forest trees such as HWIND (Peltola et al. 1999), GALES (Gardiner et al. 2000), and FOREOLE (Ancelin et al. 2004), which can predict the critical wind speeds required to break or overturn trees. These models are commonly employed to estimate wind damage to the forest, serving as forest management decision support tools. Compared to forest trees, urban trees tend to have a broader crown, and more and larger branches, indicating larger applied wind loads and likely higher windthrow risk. However, there have been very few research studies that have focused on failure modeling of urban trees due to strong winds (Ai et al. 2016; Kocatepe et al. 2018).

Fragility is defined as the probability of exceeding a prescribed limit state for a given measure of hazard intensity, and fragility analysis has been widely conducted for the performance assessment of various structures in seismic and wind hazards. However, tree fragility study under strong winds has not received deserving attention. Ciftci et al. (2014) proposed a method to obtain the fragility curves for amenity trees due to wind storms, and dynamic time history analysis of a detailed finite element tree model was carried out to determine the maximum wind-induced bending moment in the tree stem. However, in their study the fragility analysis was conducted for only two specific trees rather than a number of tree classes for each species, making it inappropriate for the risk assessment covering various uncertainties. Kocatepe et al. (2018) identified four common tree species in Tallahassee, Florida based on the convolutional neural network (CNN) method and estimated tree fragility curves with the Monte Carlo simulation. However, the mechanistic model for predicting tree failure induced by winds was rather simplified. Moreover, only stem breakage was considered and another type of major failure type- uprooting was not covered in the tree fragility studies as illustrated above.

There have been many research works related to infrastructure disruption due to the interaction between damaged buildings and the infrastructure itself subjected to natural disasters. Road blockages due to fallen debris from collapsed buildings after earthquakes cause reduced traffic capacity and increased travel delay, which will significantly affect the post-earthquake emergency response and recovery of other infrastructures. The interaction between transportation networks and buildings damaged by earthquakes have been extensively studied (Goretti and Sarli 2006; Argyroudis et al. 2015; Zanini et al. 2017). In contrast, despite catastrophic consequences to human life and infrastructures resulting from tree failure in past wind storms, researches on disruption risk of critical infrastructures caused by tree damage, however, are very limited. Kocatepe et al. (2018) evaluated the accessibility to critical emergency facilities in a disrupted transportation network caused by tree failure during hurricanes with a GIS-based methodology. Laefer and Pradhan (2006) proposed a methodology to identify potentially hazardous trees that may endanger transportation routes by utilizing GIS and airborne laser altimetry data, which has the potential for evacuation routes selection. Poulos and Camp (2010, 2011) developed a decision support system for identifying locations where powerlines can be disrupted by vulnerable trees during storms.

1.3 Current research gaps

1.3.1 Simulation of traffic flow under hazardous conditions

In order to assess the post-hazard performance of a highway system in terms of structural integrity, traffic safety and highway functionality, realistic simulation of traffic flow through a typical highway system under hazardous conditions is apparently critical. Unfortunately, there is no available tool that can provide microscopic traffic flow simulation by incorporating different driving behavior and other unique characteristics associated with hazardous driving environments. Despite some improvements on including driving behavior in traffic flow simulation in recent years, these studies still primarily focus on normal driving conditions. Hamdar (2004) investigated drivers' behavior under extreme conditions with a modified car-following model, in which different individual panic behaviors were defined. However, this study only focused on the homogeneous traffic flow rather than the heterogeneous traffic flow, and the influence of panic behavior on the overall traffic properties was not investigated. There is little study to systematically incorporate unique features essential to hazardous driving conditions in the traffic flow simulation of a general highway and bridge system.

1.3.2 Simulation of disrupted traffic flow

As discussed in Section 1.2.3, existing studies on disrupted transportation systems are relatively limited. These studies include multi-lane traffic flow simulation with a partially closed lane induced by various traffic bottlenecks, e.g., accidents, work zone, and lane reduction. Despite their merits, these studies were about specific scenarios of disrupted infrastructure based on different simulation tools and assumptions. There is no general approach that can be used to study different scenarios of a partially-blocked road or bridge due to typical causes, such as infrastructure damage, debris, vehicle accidents etc.

1.3.3 Travel time function for disrupted urban arterials

Despite reduced traffic capacity, partially blocked roads (PBR) of some critical urban traffic networks often remain open to traffic before, during and after many hazards. To conduct effective traffic planning of road networks involving PBR highly depends on accurate prediction of travel time on PBR, which is very different from those on intact roads. Because there is so far no available travel time function for PBR, the standard BPR function for intact roads has been often adopted by simply applying the reduced capacity for post-hazard transportation demand modeling. However, not only the traffic capacity is reduced for PBR, but also the travel time-volume relationship has significantly changed from its normal condition as a result of the interaction between vehicles and obstructions. Thus, the standard BPR function will likely give inaccurate travel time prediction on PBR, which may lead to erratic results in the post-hazard transportation network analysis. So there is great need to develop travel time functions for PBR that reflect the relationship between travel time and traffic volume realistically.

According to the literature review in Section 1.2.4, studies related to travel time functions mainly focus on normal traffic and very few researches have examined the development of travel time functions on PBR. In the meantime, the impact of trucks on travel time under normal condition has been studied previously, but the effect of blockage size also needs to be incorporated when estimating travel time on PBR. Moreover, existing CA-based traffic simulation models need to be improved to fully consider realistic deceleration driving behavior.

1.3.4 Vehicle accident simulation under adverse driving environments

Despite the progress made by the existing studies as summarized in Section 1.2.5, most of the existing works were conducted based on a single vehicle moving at a constant speed without considering realistic driving scenarios. Depending on the traffic volume, a vehicle on highways accelerates, decelerates, and switches lanes along with other vehicles, and it is more realistic to evaluate the traffic safety of a moving vehicle as a part of traffic flow, rather than a standalone vehicle with a constant speed. Zhou and Chen (2015b) recently carried out a preliminary vehicle safety study of traffic flow on a long-span bridge subjected to crosswinds, without considering complex road surface, geometry and weather conditions. A general traffic safety assessment methodology of traffic flow on a transportation system including both roads and bridges under various adverse driving conditions is still lacking. Moreover, for those very limited existing studies considering road curvatures (e.g. Chen and Chen 2010), wind was usually assumed to be perpendicular to the vehicle driving direction all the time. In fact, the angle between the wind direction and the instantaneous driving direction varies during the curving process and the corresponding vehicle safety performance when subjected to a specific wind event needs to be evaluated based a more realistic way of characterizing the wind loads.

1.3.5 Probabilistic modeling of disrupted infrastructures due to fallen trees

Wind damage of forest trees have been studied extensively over the last decades. Urban trees have a broader crown, and more and larger branches than forest trees, indicating larger applied wind loads and likely higher windthrow risk. However, failure modeling of urban trees due to strong winds have not received enough attention. Moreover, there are very limited studies related to tree fragility, although windthrow fragility curves are very important tools to assess vulnerability of trees subjected to winds and evaluate performance of disrupted infrastructures due to tree damages with probabilistic analysis. Finally, there are very few studies concerning disruptions risk of critical infrastructures caused by tree damage, despite catastrophic consequences to human life and infrastructures resulting from tree failure in past wind storms.

1.4 Objectives

Disruption of transportation systems by multiple hazards will impede social and commercial activities, and hamper the post-disaster emergency response and long-term recovery of the damaged community. Transportation performance are easily impaired in the link level (e.g. road capacity, link travel time, and traffic safety) and network level (e.g. network connectivity, total network travel cost and network flow capacity). As discussed in Section 1.3, previous simulation approaches to assess transportation performance in these levels are not sufficient given their limitations in modeling methodologies. Therefore, this dissertation will focus on developing advanced performance assessment techniques of transportation systems subjected to multiple hazards in two levels: link-level and network-level. It aims to (1) develop an advanced traffic performance assessment framework to evaluate various critical traffic performance aspects (e.g. travel time, traffic capacity, and traffic safety) of key transportation components (e.g. bridges and road segments) subjected to multiple hazards; (2) develop a probabilistic framework to assess the performance of transportation networks subjected to multiple hazards. Specifically, the objectives of the current dissertation are as follows:

The first objective is to develop an advanced traffic flow simulation framework on a typical highway system under hazardous conditions. This framework can help predict rationally the post-hazard performance of a highway system including both structural integrity and traffic functionality.

The second objective is to develop a simulation methodology to study the traffic performance of degraded road links being partially blocked following extreme events. The proposed methodology can predict the traffic performance of degraded transportation systems due to various causes, which can lead to a wide array of future studies such as community resilience modeling, emergency response and evacuation planning, etc.

The third objective is to develop travel time functions for PBR in urban areas based on microscopic traffic simulation. The developed travel time functions will be helpful for accurate travel demand estimate in post-hazard transportation network analysis.

The fourth objective is to develop an integrated model to assess single-vehicle traffic safety performance of stochastic traffic flow under hazardous driving conditions. This study has potential applications to not only regular vehicles, but also advanced traffic management and control algorithms for connected and autonomous vehicles in hazardous driving environments.

The fifth objective is to develop an integrated probabilistic methodology to model the performance of disrupted infrastructures due to fallen urban trees subjected to extreme winds. The proposed model can help people understand the risks of the tree failure and the impacts to some critical infrastructures and the community resilience in a specific wind event.

1.5 Outline of the dissertation

The outline of the dissertation is as follows:

Chapter 1 provides the research background for this dissertation and presents the literature review on five main research topics. Meanwhile, the current research gap for each research topic are identified and the research objectives are described.

In Chapter 2, an advanced traffic flow simulation framework on a typical highway system under hazardous conditions is proposed. As an improved CA microscopic traffic flow simulation methodology, limited deceleration rate, anticipation effect, realistic vehicle properties and different driving behaviors can be considered for replicating realistic traffic flow. Traffic flow on a prototype highway system under normal and hazardous conditions are simulated and examined by the proposed framework. The influences of limited acceleration and anticipation effect are investigated on the characteristics of traffic flow. Finally, the effect of panic driving behavior during a hypothetical hazard process is evaluated and discussed in terms of the traffic load on the bridge, overall traffic flow properties and individual vehicle driving performance.

Chapter 3 studies the traffic performance of degraded road links being partially blocked following extreme events. A CA-based microscopic simulation methodology is proposed for modeling traffic performance of partially-blocked roadway and bridge links due to hazardous events, which can be applied to degraded road/bridge links with various types of obstacles (different sizes, numbers and distributions).

Two typical partially-blocked scenarios are investigated to demonstrate the feasibility of the proposed methodology in studying the traffic performance of disrupted roadway links following extreme events.

In Chapter 4, travel time functions for PBR in urban areas are developed based on microscopic traffic simulation. Firstly, an improved CA model for traffic flow simulation on disrupted urban arterials is proposed based on the two-lane safety driving (SD) model, with which unrealistic deceleration behaviors can be fully avoided and driver's behaviors during traffic signal change intervals can be realistically replicated. Secondly, the proposed model is calibrated and validated at microscopic and macroscopic levels with measured traffic data from an urban road. Finally, traffic data under various scenarios with different traffic volumes, truck ratios and blockage ratios are generated through microscopic simulation experiments. A continuous traffic time function is then developed for disrupted traffic flow and its parameters are estimated with the generated traffic data.

In Chapter 5, an integrated framework is proposed to evaluate the overall safety performance of vehicles in realistic stochastic traffic passing through highway infrastructure systems. The proposed framework evaluates individual vehicle safety performance based on the time-dependent simulation results of stochastic traffic flow, including instantaneous speeds and positions of each vehicle as a part of simulated traffic flow. With the safety information of each individual vehicle, an overall safety performance index of the whole traffic flow on the highway system is further introduced, which serves as a potential traffic safety performance measure and resilience indicator of transportation infrastructure systems under various hazards. The proposed framework is then applied to a bridge-roadway system for demonstration purposes.

Chapter 6 evaluates the performance of disrupted infrastructures due to fallen urban trees subjected to extreme winds in a typical community with an integrated probabilistic methodology. We firstly develop allometric equations for three urban tree species to facilitate the development of the mechanistic model and fragility curves. Secondly, a mechanistic model based on finite element modeling is built with the direct stiffness method by considering wind profile, wind loads and self-weight of trees. Thirdly, fragility curves of three tree species are generated for both stem-breaking and uprooting limit states through Monte Carlo simulation. Finally, the performance of disrupted critical infrastructures in a small community in the city of Fort Collins, such as transportation and overhead powerline infrastructures, due to fallen trees, is evaluated with the proposed probabilistic method.

Chapter 7 concludes the dissertation by highlighting the main findings and suggesting some future research directions.

CHAPTER 2 FRAMEWORK OF MICROSCOPIC TRAFFIC FLOW SIMULATION ON HIGHWAY INFRASTRUCTURE SYSTEM UNDER HAZARDOUS DRIVING CONDITIONS[1]

2.1 Introduction

A typical highway system includes infrastructures, such as roadways and bridges, and moving traffic flow. The resilience of a highway system subjected to various hazards depends on not only post-hazard integrity of infrastructure, but also safe and smooth movements of vehicles through the system during and immediately following hazards. On the one hand, post-hazard traffic by panicking drivers can easily cause local traffic congestion and concentrating loads on bridges, which can become disastrous to those bridges already severely damaged by hazards. On the other hand, the accident risks of vehicles following hazards may considerably increase because of more irrational driving behavior and traffic congestion, threatening the post-hazard functionality of the highway system. To rationally predict the post-hazard performance of a highway system including both structural integrity and traffic functionality, an advanced traffic flow simulation tool of a highway system under hazardous conditions is needed.

This chapter aims to develop an advanced traffic flow simulation framework on a typical highway system under hazardous conditions. Based on the cellular automaton (CA) microscopic traffic flow simulation methodology, the proposed framework can consider limited deceleration rate, anticipation effect, realistic vehicle properties and different driving behaviors. The proposed framework is then applied to a prototype highway system for traffic flow simulation under normal and hazardous conditions. The influences of limited acceleration and anticipation effect are investigated on the characteristics of traffic

[1] This chapter is adapted from a published paper by the author (Hou et al. 2017) with permission from Taylor & Francis.

flow. Assuming a typical hazard occurrence process, the effect of panic driving behavior on the traffic load on the bridge, overall traffic flow properties and individual vehicle driving performance are evaluated and discussed.

2.2 Model formulations

Since Nagel and Schreckenberg (1992) first proposed the CA model (also called NaSch's model), some progress has been made in developing more sophisticated models by mainly focusing on three aspects: update rule, realistic vehicle performance and driving behavior (Barlovic et al. 1998; Benjamin et al. 1996; Esser and Schreckenberg 1997; Knospe et al. 2000). In the proposed model, the lanes are discretized into many identical cells with the length of 0.5 m, each of which is either empty or occupied by a vehicle at a time. Depending on the length of each individual vehicle, different numbers of cells may be occupied by each vehicle. The adoption of a finer discretization than that being used in traditional NaSch's models (e.g. 7.5 m) makes it easier to define more realistic driving and acceleration/deceleration movements of different types of vehicles with sufficient accuracy (e.g., the vehicle length, abrupt acceleration/deceleration).

Let x_i^t and V_i^t be the longitudinal position and velocity of vehicle i at the beginning of time step t. At next time step $t+1$, position x_i^{t+1} and velocity V_i^{t+1} can be updated through the improved double-lane CA rules: the single-lane forwarding rule and lane-changing rule. The forwarding rule can be described as follows:

(1) Acceleration:

$$V_i^{t+1} = min\left(V_i^t + acc_i, V_{i,max}\right) \tag{2.1}$$

(2) Deceleration:

$$V_i^{t+1} = min\left(V_i^{t+1}, V_{i,d}^{t+1}\right) \tag{2.2}$$

(3) Safety:

$$V_i^{t+1} = min\left(V_i^{t+1}, V_{i,safe}^{t+1}\right) \tag{2.3}$$

(4) Randomization with probability pb:

$$V_i^{t+1} = max\left(V_i^{t+1} - dec_i, 0\right), \text{ if } V_i^t - V_i^{t+1} < dec_{max} - dec_i \tag{2.4}$$

(5) Braking:

$$br_i^{t+1} = 1, \text{ if } V_i^t - V_i^{t+1} > 0 \tag{2.5}$$

$$br_i^{t+1} = 0, \text{ if } V_i^t - V_i^{t+1} \leq 0 \tag{2.6}$$

(6) Movement:

$$x_i^{t+1} = x_i^t + V_i^{t+1} \tag{2.7}$$

where $V_{i,max}$ denotes the desired speed of vehicle i, which is typically considered as the road speed limit under normal driving conditions. Only for aggressive drivers under hazardous driving conditions, the desired speed is set higher than the speed limit. acc_i and dec_i denote the normal acceleration and deceleration rates of vehicle i, respectively. dec_{max} is the maximum deceleration rate, which can't be exceeded due to the mechanical constraint of a specific vehicle and the friction of road surface. $V_{i,d}^{t+1}$ denotes the maximum velocity for vehicle i braking with dec_{th} when its headway is d at time step $t + 1$. $V_{i,safe}^{t+1}$ denotes the maximum safe velocity for vehicle i braking with dec_{max} at time step $t + 1$. br_i^t is the state of braking light of vehicle i at time step t. br_i^t = 1 or 0 means braking light of vehicle i is on or off, respectively.

The lane-changing behavior of vehicle i will be triggered with a probability of pch, once all the following conditions are satisfied:

$$gap_i^t \leq V_i^t \tag{2.8}$$

$$gapo_{i,front}^{t} > V_i^t \tag{2.9}$$

$$gapo_{i,back}^{t} > V_{i,max} \tag{2.10}$$

where $gap_i^t = x_{i+1}^t - x_i^t - L_{i+1}$; L_i is the length of vehicle i. gap_i^t is the clear distance between vehicle i and its preceding vehicle $i+1$ on the current lane at time step t; $gapo_{i,front}^t = x_{fi}^t - x_i^t - L_{fi}$ and $gapo_{i,front}^t$ is the clear distance between vehicle i and the nearest vehicle on the target lane ahead of vehicle i at time step t; vehicle fi is the nearest vehicle on the target lane ahead of vehicle i; $gapo_{i,back}^t = x_i^t - x_{bi}^t - L_i$ and $gapo_{i,back}^t$ is the clear distance between vehicle i and the nearest vehicle on the target lane behind vehicle i at time step t; vehicle bi is the nearest vehicle on the target lane behind vehicle i.

2.2.1 Adoption of improved rules for more realistic traffic flow simulation

The following improved rules are applied to the proposed model in order to simulate more realistic traffic flow, especially under hazardous conditions.

1) Limited deceleration and deceleration rates

In traditional NaSch's model, when a sudden brake is applied to avoid a rear-on crash under some emergency situations, a vehicle may make a sudden stop from its maximum velocity, which may lead to some unrealistic deceleration rate (Bham 2002; Chen and Wu 2011) and in turn cause inaccurate simulation results of traffic flow. Different from the deceleration rule in NaSch's model, a deceleration threshold dec_{th} is introduced to avoid an abrupt brake at the last second (Yamg et al. 2007). The stopping distance SD with an initial speed of V_0 can be expressed as:

$$SD = V_0 + \sum_{k=1}^{[V_0/dec_{th}]}(V_0 - dec_{th} \times k) \tag{2.11}$$

where $[x]$ denotes the nearest integer less than or equal to x.

If SD is less than or equal to the headway d of a vehicle, the vehicle can move with a maximum velocity of V_d, a function of headway d. Thus, the vehicle can decelerate gradually before a complete stop within the headway d without applying an abrupt brake. At next time step $t+1$, velocity V_d of vehicle i can be obtained by

$$V^{t+1}{}_{i,d} = max\left\{v \middle| \, v + \sum_{k=1}^{[v/dec_{i,th}]} (v - dec_{i,th} \times k) \leq d\right\} \tag{2.12}$$

where $d = gap_i^t$, if $br_{i+1}^t = 1$; or $d = gap_i^t + V^t{}_{i+1} - \lambda_{ant,i} \times dec_{i+1}$, if $br_{i+1}^t = 0$; $\lambda_{ant,i}$ is a parameter to anticipate the velocity of the preceding car. $dec_{i,th}$ is the deceleration threshold of vehicle i.

Another safety rule is introduced to avoid exceeding the vehicle's deceleration limits (Yang et al. 2007). If vehicle i that brakes with the maximum deceleration rate dec_{max} is safe at time step $t+1$, its stopping distance cannot be larger than its headway plus the minimum stopping distance of the front vehicle $i+1$. By satisfying this safety condition, the maximum safe velocity of vehicle i at time step $t+1$ can be expressed as

$$V^{t+1}{}_{i,safe} = max\left\{v \middle| \, v + \sum_{k=1}^{[v/dec_{max}]} (v - dec_{max} \times k) \leq gap^t{}_i + \sum_{j=1}^{[V^t{}_{i+1}/dec_{max}]} (V^t{}_{i+1} - dec_{max} \times j)\right\} \tag{2.13}$$

AASHTO (2004) recommends a maximum deceleration rate 3.4 m/s^2, which is a typical deceleration rate limit for ordinary drivers. Braking with a deceleration rate higher than 3.4 m/s^2 can be deemed as an abrupt brake. Considering deceleration rate needs to be in multiples of 0.5, the deceleration rate threshold of 3.5 m/s^2 is adopted for normal drivers. In the absence of more specific experimental data, the deceleration thresholds for timid and aggressive drivers are set to be 2.0 m/s^2 and 5.0 m/s^2 in this study, respectively. Different from the deceleration threshold, the maximum achievable deceleration is related to the mechanical constraint of a particular vehicle and the coefficient of friction of the road surface. Fambro et al. (1997) found that the maximum deceleration rate ranges from 0.7 g to 0.9 g (g = 9.8 m/s^2). In this model, the maximum achievable deceleration is set as 8.0 m/s^2 for all the vehicles.

2) Anticipation effect

Anticipation means that the velocity of a vehicle is updated in the following time step based on not only the gap distance from its preceding vehicle, but also the velocity of the preceding vehicle (Li et al. 2001; Xie and Zhao 2013). In the deceleration step of their models, the velocity of vehicle i at time step $t+1$ is obtained by using the following equation:

$$V_i^{t+1} = min\left(V_i^t, gap_{i,effective}^t\right) \tag{2.14}$$

where

$$gap_{i,effective}^t = gap_i^t + V_{i+1,anti}^{t+1} \tag{2.15}$$

$gap_{i,effective}^t$ is the effective gap of vehicle i from its preceding vehicle at time step t, and $V_{i+1,anti}^{t+1}$ denotes the anticipated velocity of the preceding vehicle $i+1$ at time step $t+1$. The effect of anticipation increases the traffic capacity for free flow by reducing the gap distances among vehicles (Larraga et al. 2004). However, it is found that the effect from anticipation becomes weak for dense traffic flow, and cars tend to have smaller velocities than headways (Knospe et al. 2000).

In this model, the anticipation parameter λ_{ant} is used in the deceleration step when calculating the effective headway of the following vehicle, which is equal to the sum of actual headway and anticipated velocity of the preceding vehicle. The values of λ_{ant} for timid, normal and aggressive drivers are set as 2, 1 and 0, respectively. $\lambda_{ant} = 0$ means that aggressive drivers have higher anticipation level and tend to drive with small gap distances between vehicles. Larger anticipation parameters of timid and normal drivers represent lower anticipation levels and more conservative driving behavior.

2.2.2 Incorporation of different vehicle properties

It is common that traffic flow is composed of different types of vehicles with different properties (e.g., dimensions and acceleration/deceleration performance). In this model, three types of vehicle groups are considered (i.e. cars, buses, and trucks) to capture the main traffic classifications on highways.

1) Vehicle dimension

In the traditional NaSch's model, the length of each cell is 7.5 m and each vehicle occupies one cell at a time. Thus vehicle velocity and acceleration/deceleration rates are restricted to multiples of 7.5 m. Finer discretization has been introduced to enable more realistic acceleration and more speed bins (Hafstein et al. 2004; Knospe et al. 2000; Lan and Chang 2005; Larraga and Alvarez-Icaza 2010; Rajeswaran and Rajasekaran 2013). With a much smaller cell length (0.5 m) in the present study, different types of vehicles and a whole range of driving speeds can be modeled to investigate the movements of mixed traffic flow. Following the study by Oketch et al. (2004), the lengths of cars, buses, and trucks in this model are defined as 5 m, 10 m and 19 m, occupying 10 cells, 20 cells and 38 cells, respectively.

2) Normal vehicle acceleration and deceleration rate

Different from deceleration threshold dec_{th}, which is used to avoid an abrupt brake at the last second, normal deceleration rate dec refers to vehicles' deceleration under normal situations. dec has a lower value than dec_{th}. dec is used in the randomization step when the vehicle slows down with the probability of pb and in the deceleratioin step when calculating the headway d. Similarly, normal acceleration rate acc refers to vehicles' acceleration under normal traffic situations. Wang et al. (2007) summarized the acceleration and deceleration data that were obtained empirically and applied them in some car-following models for highway traffic and urban network. According to their findings, normal acceleration and deceleration rates usually range from 1 to 2 m/s^2 and 1 to 3 m/s^2, respectively. In this paper, given the fact that acceleration and deceleration rates should be the multiples of 0.5, the acceleration/deceleration rates in normal driving conditions of cars, buses, and trucks are set as 1.5 m/s^2, 1.0 m/s^2, and 1.0 m/s^2, respectively.

2.2.3 Incorporation of different driving behavior under normal and hazardous conditions

1) Characterization of different driving behaviors

Due to differences on their knowledge, skill, perceptual and cognitive abilities, drivers may perform differently even under the same traffic scenario (Evans 2004). Timid drivers tend to keep large headways with the preceding vehicle, maintain a steady speed and change lane rarely, while aggressive drivers tend to keep short headway with the preceding vehicle and change lanes more frequently to get a higher speed. It is found that aggressive driving is one of the most serious traffic safety threats and a major contributor to traffic accidents (AAA Foundation for Traffic Safety 2009). For congested freeway traffic, both timid and aggressive driving behaviors are found to be the causes of traffic oscillations (Laval and Leclercq 2010).

Timid, normal and aggressive driving behaviors are considered in this study by defining different deceleration thresholds, lane-changing probability values and anticipation parameters in the model. These parameters for different drivers such as deceleration threshold and anticipation parameter often require detailed driving behavior study from specific groups of driver populations.

2) Proportions of different driver groups

Under normal driving conditions, there are usually different proportions of three types of driver groups (i.e. timid, normal and aggressive) for a particular highway. Given the uncertainties associated with the proportions of driver groups at different highways at different time, generic proportions of drivers are nearly impossible to identify. Under hazardous driving conditions, the proportion of aggressive drivers will usually increase because of panic behavior, and the proportions of the other two types of drivers will also change accordingly. Depending on the nature of the hazards and site-specific conditions, these proportions of different driver groups could all vary considerably.

2.3 Demonstrative example

2.3.1 Prototype highway system and CA model parameters

Both roadways and bridges are supporting structures for moving traffic. Compared with bridges, roadways are much stiffer and the interaction between the roadways and vehicles can be ignored when the vehicles move on roadways. When the vehicles in the traffic flow move on the bridge, the vehicle wheels are assumed to have point contact with the bridge deck all the time. As the bridge and vehicles are vibrating when the vehicles are in motion, bridges, especially long-span bridges, experience much more significant impact on structural dynamic response than roadways under moving traffic loads. In the meantime, the vibration of the bridge may in turn affect the dynamic behavior of the vehicles because of the significant interaction effects between bridge and vehicles (Zhou and Chen 2015a). Therefore, vehicles on bridges usually experience stronger dynamic vibration and higher traffic accident risks than on roadways. The proposed traffic flow framework can be used for traffic flow simulation on any general highway system including both bridges and roadways. To demonstrate possible impacts on structural integrity and traffic safety performance on bridges, a typical 4-lane highway system is selected in the demonstrative study with two lanes in each direction and it includes a prototype long-span bridge and a piece of approaching roadway on each side of the bridge (Fig. 2.1). The lengths of the bridge and roadway on each side are 840 m and 1,005 m, respectively, making the total length of 2,850 m for this "roadway–bridge–roadway" system, similar to the one being studied by Chen and Wu (2011).

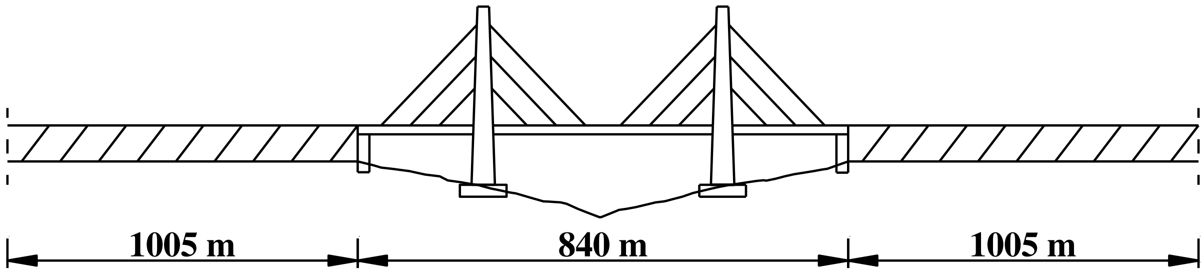

Figure 2.1 Bridge and road system

In this CA model, periodic boundary conditions are used. Each cell represents an actual roadway/bridge segment with the length of 0.5 m and there are a total of 5,700 cells in one lane. The percentage values of different groups of vehicles vary significantly on different roads and at different time. There is no general guideline in terms of vehicle composition of the traffic flow that is widely accepted. Therefore, in the present study, it is assumed that the values following some existing studies (Chen and Wu 2010, 2011) for demonstration purposes only, without representing any specific site or time. For three types of vehicles, i.e. car, bus and truck, their proportions are assumed to be 50%, 25%, and 25%, respectively. The initial location of each vehicle in the lane is randomly generated and the initial velocity of each vehicle is zero. At each time step, the vehicle velocity will be updated according to the CA rules as introduced earlier. The total simulation time period is 17,400 s and the time simulation step is 1 s. To capture the steady traffic flow characteristics, the simulation results of the first 11,400 s are discarded and only those of the last 6,000 s will be used and presented in the following sections.

Existing data related to the driving behavior and driver group classifications are usually location-specific and often require comprehensive experiments to quantify. Currently, the related data are still very rare and no widely accepted generic data are available that can be directly used for the proposed model. In order to demonstrate the proposed framework, some parameters need to be appropriately set based on existing literature and reasonable assumptions. In this study, the lane-changing probability pch of timid drivers, normal driver, and aggressive drivers are assumed to be 0.2, 0.5 and 0.8, respectively. Under normal driving conditions, the proportions of timid, normal and aggressive drivers for each type of vehicles are assumed as 20%, 60%, and 20%, respectively. While under hazardous driving conditions, the proportions of three types of drivers are set to be 20%, 20%, and 60%, respectively.

Drivers in heavy traffic are usually more cautious and responsive to varying driving environments and therefore the randomization probability can be assumed to increase with the increase of traffic occupancy. The relation between randomization probability pb and traffic occupancy ρ is defined as: $pb = 0.5 * \sqrt{\rho}$ (Yamg et al. 2007). Apparently, all the vehicles have different instantaneous driving speeds on the roadway and bridge system and the number of total vehicles remaining on the bridge also varies when the traffic flow moves over the bridge. It is well known that space mean speed is commonly used in traffic engineering to describe the overall traffic speeds. However, the proposed framework is aimed to provide information to evaluate both overall structural loads/performance on the bridge and individual vehicle response/safety risks. Therefore, an average of the instantaneous speeds of all the vehicles remaining on the bridge at any time instant is used to assess the overall traffic condition on the bridge, which can serve as an indication of the potential loads on the bridge. Mean velocity $\bar{V}$ and mean standard deviation $\bar{\sigma}$ of all vehicles on the bridge for a certain simulation time T are used as the main evaluation indicators, which are defined as follows.

$$\bar{V} = \frac{1}{T}\sum_{i=1}^{T}\left(\frac{1}{N}\sum_{j=1}^{N} V_j\right) \tag{2.16}$$

$$\bar{\sigma} = \frac{1}{T}\sum_{i=1}^{T}\left(\sqrt{\frac{1}{N}\sum_{j=1}^{N}\left(V_j - \frac{1}{N}\sum_{k=1}^{N} V_k\right)^2}\right) \tag{2.17}$$

where N denotes the total number of vehicles on the bridge at time step i.

Traffic flows under both normal and hazardous (panic) driving conditions are simulated. As discussed earlier, compared to normal driving conditions, hazardous (panic) driving conditions usually involve a higher proportion of aggressive drivers who behave more aggressively due to possible panicking nature. For example, the acceleration rates of three types of vehicles are higher and drivers tend to brake with a higher deceleration rate. In addition, during hazardous driving conditions, it is assumed that aggressive drivers may exceed the posted speed limits up to 50%. Parameters used in normal and hazardous (panic) traffic conditions are summarized in Tables 2.1 and 2.2, respectively.

Table 2.1 Parameters and benchmark value used in normal traffic

Parameter	Value	Parameter	Value
L_{car}	5 m	dec_{car}	1.5 m/s^2
L_{bus}	10 m	dec_{bus}	1.0 m/s^2
L_{truck}	19 m	dec_{truck}	1.0 m/s^2
V_{max}	20 m/s	$dec_{th,timid}$	2.0 m/s^2
R_{car}	0.5	$dec_{th,normal}$	3.5 m/s^2
R_{bus}	0.25	$dec_{th,aggr}$	5.0 m/s^2
R_{truck}	0.25	dec_{max}	8.0 m/s^2
R_{timid}	0.2	pch_{timid}	0.2
R_{normal}	0.6	pch_{normal}	0.5
R_{aggr}	0.2	pch_{aggr}	0.8
acc_{car}	1.5 m/s^2	$\lambda_{ant,timid}$	2.0
acc_{bus}	1.0 m/s^2	$\lambda_{ant,normal}$	1.0
acc_{truck}	1.0 m/s^2	$\lambda_{ant,aggr}$	0

Table 2.2 Parameters and benchmark value used in panic traffic

Parameter	Value	Parameter	Value
L_{car}	5 m	acc_{truck}	1.5 m/s^2
L_{bus}	10 m	dec_{car}	2.0 m/s^2
L_{truck}	19 m	dec_{bus}	1.5 m/s^2
$V_{max,timid}$	20 m/s	dec_{truck}	1.5 m/s^2
$V_{max,normal}$	20 m/s	$dec_{th,timid}$	2.0 m/s^2
$V_{max,aggr}$	30 m/s	$dec_{th,normal}$	3.5 m/s^2

R_{car}	0.5	$dec_{th,aggr}$	5.0 m/s^2
R_{bus}	0.25	dec_{max}	8.0 m/s^2
R_{truck}	0.25	pch_{timid}	0.2
R_{timid}	0.2	pch_{normal}	0.5
R_{normal}	0.2	pch_{aggr}	0.8
R_{aggr}	0.6	$\lambda_{ant,timid}$	2.0
acc_{car}	2.0 m/s^2	$\lambda_{ant,normal}$	1.0
acc_{bus}	1.5 m/s^2	$\lambda_{ant,aggr}$	0

2.3.2 Influence of limited acceleration and anticipation effect

Two major improvements such as limited deceleration of vehicles and anticipation ability of drivers are incorporated in the proposed model. Although existing studies found that limited deceleration of vehicles and anticipation effects are respectively important to improve the simulation results, the impact and significance of simultaneous inclusion of these two improvements in the proposed traffic flow simulation still need to be evaluated. The evaluation focuses on the impact on the simulation results of overall traffic flow and also individual vehicles by comparing the results from the proposed model with those from another two comparative models. The differences between the two comparative models and the proposed model are: for Model 1, limited deceleration is not considered; for Model 2, the anticipation ability of drivers is not considered.

Mean flow rate and mean standard deviation of the velocities of the proposed model, Model 1 and Model 2 are plotted in Fig. 2.2a and 2.2b, respectively. It is shown in Fig. 2.2a that the mean flow rate from Model 1 is higher than the proposed model, especially in low-occupancy traffic. Such a gap reaches the largest when the occupancy is about 0.3 for busy flow. At this point, the mean flow rate from Model 1 is 81% higher than the proposed model. Apparently, the mean flow rate is overestimated with Model 1 due to the unlimited deceleration of vehicles, especially in low-occupancy traffic, in which vehicles usually have relatively large headways. It is also shown in Fig. 2.2a that the mean flow rate from Model 2 is lower than the proposed model in low-occupancy traffic, but higher in dense traffic. This result corroborates the conclusion from Knospe et al. (2000). The inclusion of anticipation effect of drivers causes the traffic speed to increase in low traffic occupancy, but this is not the case in dense traffic flow.

It can be seen from Fig.2.2b that the mean standard deviation of velocities on the bridge in Model 2 is smaller than the proposed model. This is because without considering anticipation effect, drivers in Model 2 tend to drive more conservatively than the proposed model. It is also shown in Fig. 2.2b that the mean standard deviation of the velocities in Model 1 exhibits much larger fluctuations, which is lower in low-occupancy traffic flow and yet higher in high-occupancy flow than the other two models. For Model 1, the standard deviation of velocities in low-occupancy traffic is nearly zero because vehicles do not decelerate with relative large headways. Vehicles only decelerate at the last second, leading to an unrealistically high deceleration rate in dense traffic.

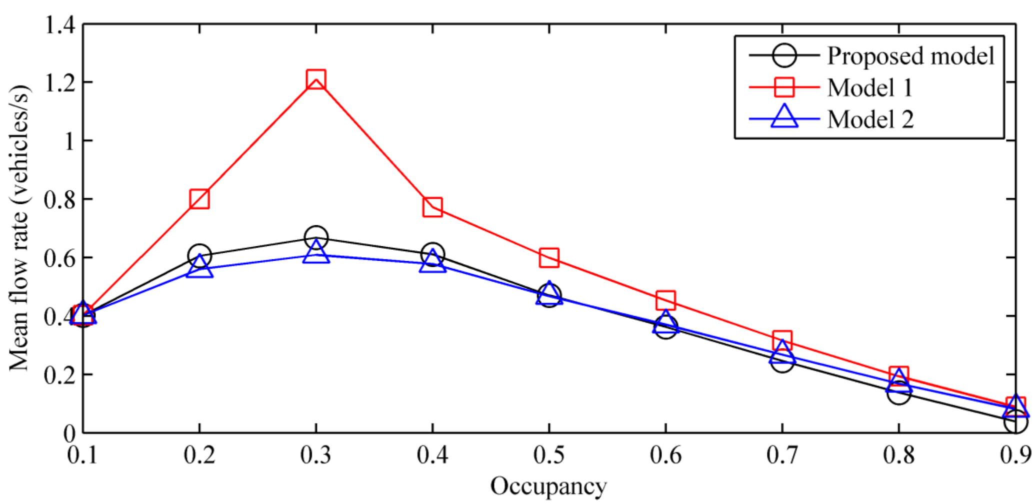

(a) Mean flow rate

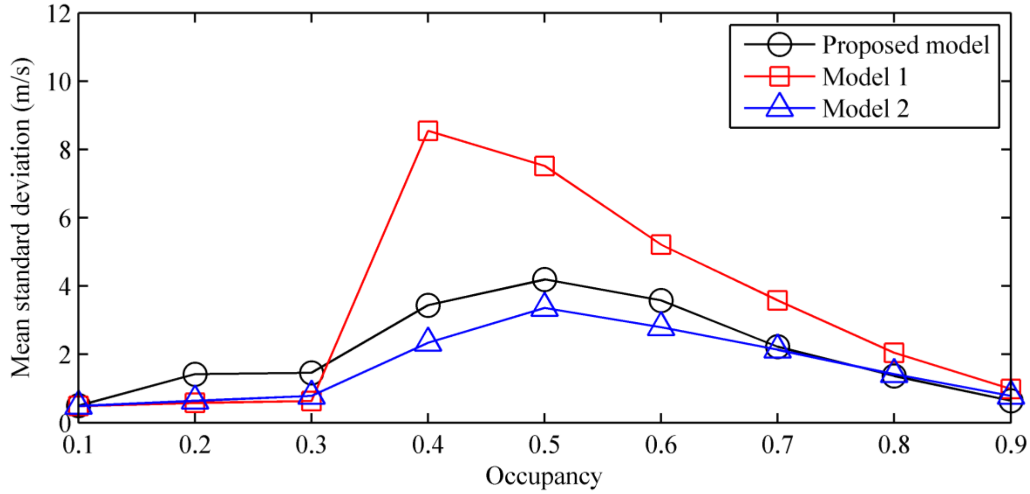

(b) Mean SD of velocity

Figure 2.2 Comparison of overall flow

Velocity time history data of a selected car with a typical driver in three models are plotted in Fig. 2.3. It is found from Fig. 2.3a that in busy flow, the car in Model 1 moves at speeds around the speed limit (20 m/s) and brakes very rarely. The car in the proposed model moves at about 11 m/s, which is much lower than that in Model 1. By introducing the rule of limited deceleration, drivers tend to adjust their speed to avoid uncomfortable braking and possible accident occurrence. Without anticipation of the velocity of the preceding car, the driver of the rear car in Model 2 determines its velocity only by the free space in front of the car and therefore moves slower than in the proposed model.

It is shown in Fig. 2.3b that when the traffic occupancy is 0.4, the car in Model 1 moves with a high velocity before a sudden brake is taken at 36 s at a deceleration rate of 14 m/s^2. Apparently, such a deceleration rate will be unrealistically high. In the proposed model, the car moves more steadily at around 9.5 m/s, and no sudden brake happens. Without considering anticipation effects, the car in Model 2 moves slower than the proposed model, contributing to a lower mean flow rate of the overall traffic. The comparison between the proposed model and two comparative models as summarized above clearly shows that the inclusion of improved rules can considerably affect and lead to more realistic simulation results. Therefore, the incorporation of limited deceleration and anticipation effects in the proposed model is found to be necessary and important.

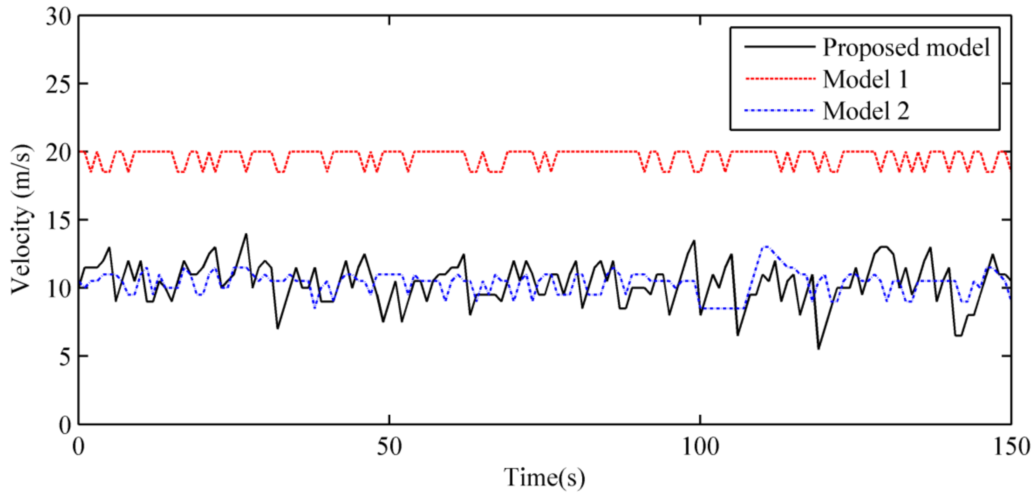

(a) Occupancy = 0.3

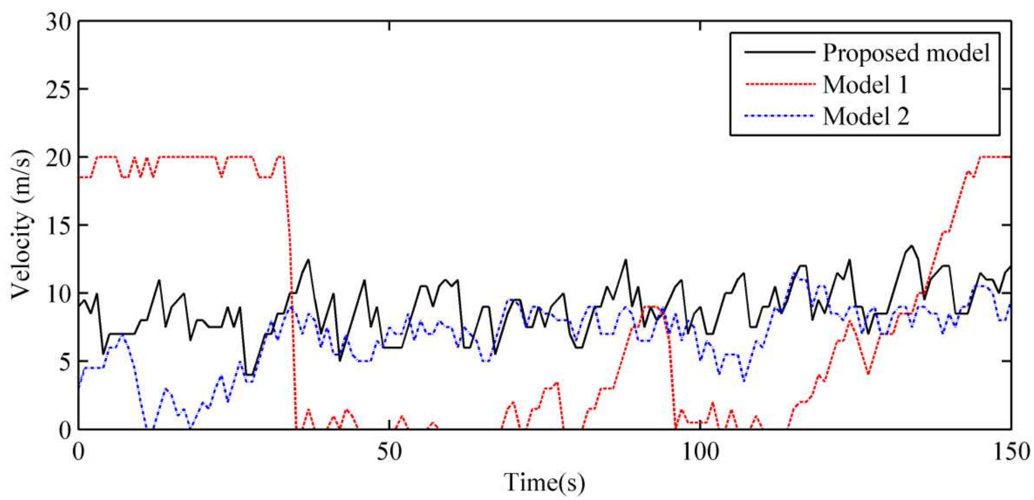

(b) Occupancy = 0.4

Figure 2.3 Comparison of velocity time history of individual vehicle

2.3.3 Influence of panic driving behavior on the overall traffic flow characteristics

Under both normal and panic driving conditions, traffic congestion begins to form in traffic flow with occupancy of 0.4. When traffic occupancy is higher than 0.4, congestion becomes more significant and the flow rate gets lower. However, since vehicles in such traffic flows have very limited space to move, they are much less likely to be influenced by the panic driving behaviors. Therefore, the study only investigates the influence of panic driving behavior on the traffic flows with occupancy below 0.4. Traffic flows with occupancy of 0.1, 0.2, 0.3 and 0.4 are hereafter called free, moderate, busy and congested traffic flow, respectively.

Time histories of instantaneous mean velocities of congested flow for normal and panic traffic conditions are plotted in Fig. 2.4. Different from the overall mean velocity of a traffic flow defined in Eq. (2.16), the instantaneous mean velocity is obtained by averaging the velocities of all vehicles in the traffic flow at each time instant. The mean values of the two curves are very close, but the standard deviation of panic traffic is 61% higher than that of normal traffic. Hazardous (panic) condition is found to significantly increase the velocity fluctuations of vehicles, which are closely related to potential accident risks (Chen et al. 2011).

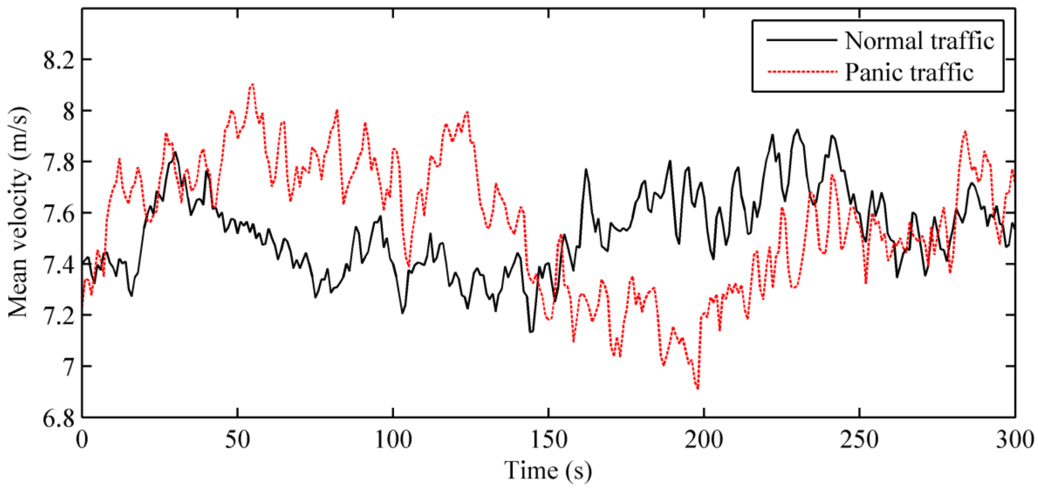

Figure 2.4 Time history of instantaneous mean velocity of congested flow for normal and panic traffic

The mean velocity of the traffic flows under normal and hazardous conditions with respect to occupancy are plotted in Fig. 2.5. The mean velocity decreases as the occupancy of the traffic flow increases under both normal and panic traffic conditions. The mean velocity of normal traffic flow decreases almost linearly with the increase of occupancy. Compared to normal traffic flow, the decreasing rate of mean velocity in panic traffic flow gradually becomes smaller when traffic occupancy increases, as seen by the smaller slope of the curve with a larger occupancy. The largest discrepancy of mean velocity occurs when traffic occupancy is 0.2, in which the mean velocities of normal and panic traffic flow are 14.9 and 15.8 m/s, respectively.

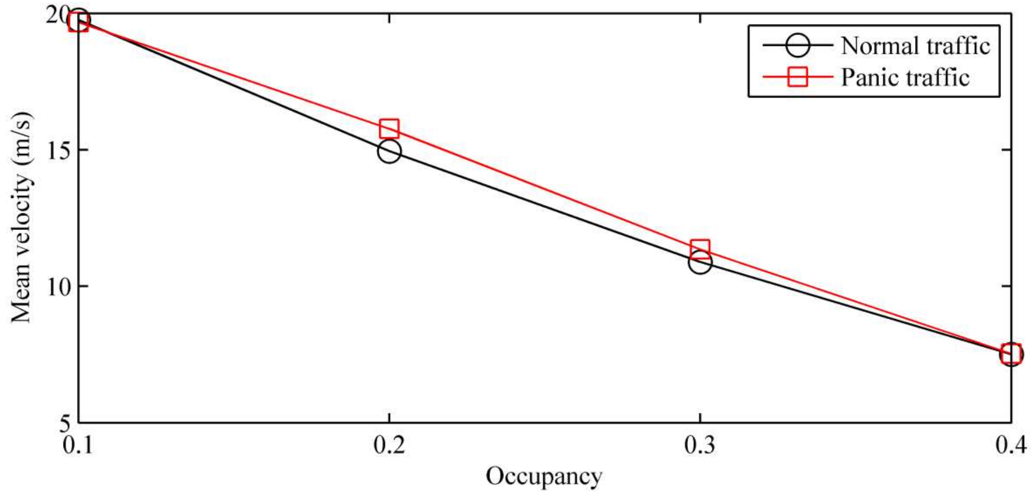

Figure 2.5 Mean velocity of normal and panic traffic

The mean velocities are very close among different types of drivers in either normal or panic traffic flow. However, the mean standard deviations have remarkable difference among different types of drivers. To show the variation of vehicle velocity corresponding to different driver types in both normal and panic traffic flows, the mean standard deviations of the vehicle velocities are obtained for timid, normal, aggressive drivers and all drivers irrespective of the driver type. Figs. 2.6a and 2.6b demonstrate the mean standard deviation values for normal and hazardous (panic) traffic driving conditions, respectively. The velocities of aggressive drivers have larger fluctuations than those of normal and timid drivers in both traffic scenarios as evidenced by larger standard deviations. For both normal and panic traffic scenarios, the largest mean standard deviation of velocities occurs in congested flow for all types of drivers. In free flow, the mean standard deviation values are very similar among different drivers in normal traffic conditions. In contrast, vehicles operated by aggressive drivers in free flow have more fluctuating velocities than other drivers under panic traffic conditions. The mean standard deviation increases significantly when traffic occupancy increases from 0.1 to 0.2 except for the aggressive driver in the panic flow, while the value remains steady when the traffic occupancy is in the range between 0.2 and 0.3. After traffic occupancy increases beyond 0.3, the mean standard deviation increases at similar rates for different types of driver groups. The mean standard deviations for all drivers are very close to the corresponding values for normal drivers under normal traffic conditions. However, under panic driving conditions, the values for all drivers get close to the corresponding value for aggressive drivers in each traffic flow case. By comparing Figs. 2.6a and 2.6b, it is found that the standard deviation of the vehicle velocity is larger in the panic flow than the corresponding value in the normal flow, which is true for each type of drivers, especially for the aggressive driver in the free flow condition. This indicates that aggressive drivers play an important role in the overall traffic flow performance under panic driving conditions.

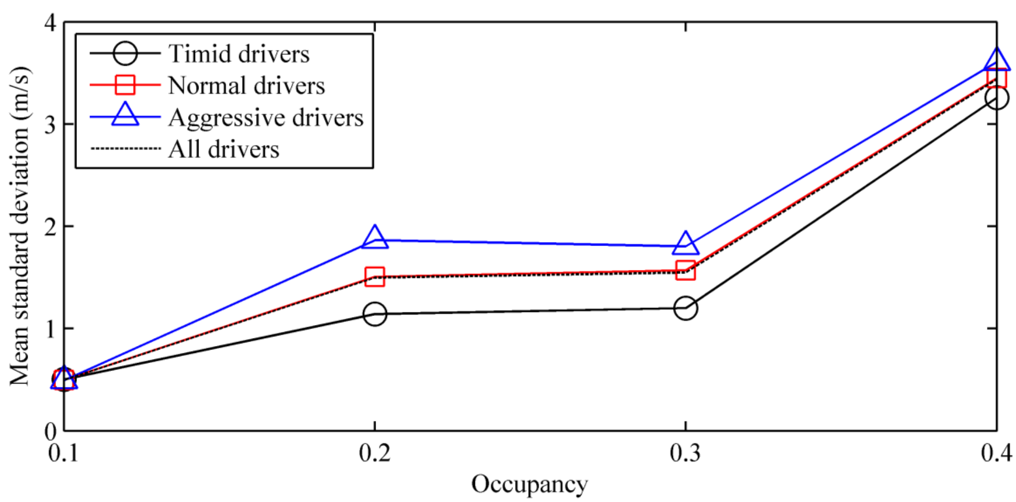

(a) Normal traffic

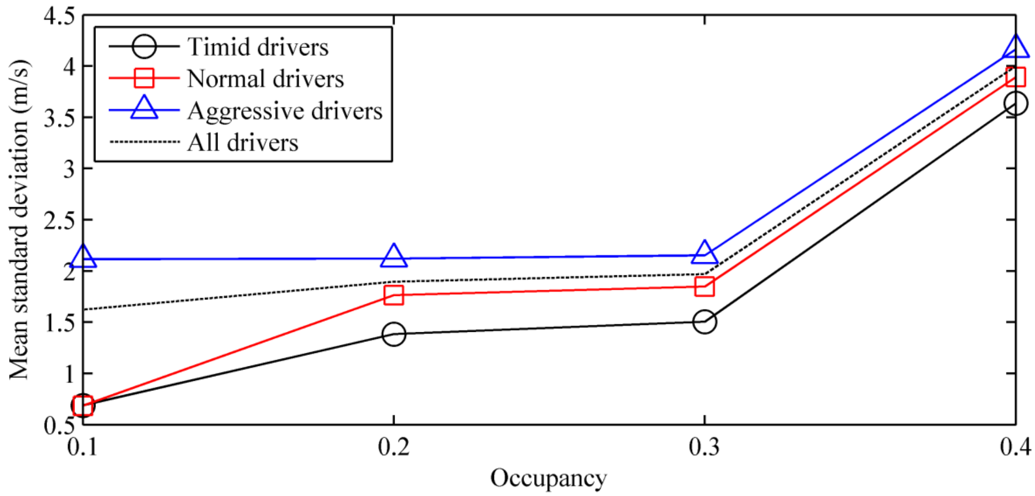

(b) Panic traffic

Figure 2.6 Mean standard deviation of velocity of normal and panic traffic

2.3.4 Application on simulating traffic flow throughout hazard process

In order to investigate the influence of a change in driving behavior on the vehicle performance, a realistic traffic scenario is simulated throughout a whole process of hazard occurrence including before and after a hazard (e.g., earthquake, blast) suddenly occurs. It is assumed that a hazard happens suddenly and has been detected by drivers on the bridge-roadway system at a certain time instant. The reaction time of a driver is assumed to be very short and the transition of driving behavior occurs immediately. Therefore, the traffic flow before that time instant is normal and after the instant it becomes panic traffic flow. Based on the simulated traffic flow results over the hazard occurrence process, the traffic loads acting on the bridge and the performance of individual vehicles are further evaluated in the following.

2.3.4.1 <u>Traffic loads on the bridge</u>

A time-space diagram of congested traffic flow (occupancy = 0.4) on the bridge under normal and hazardous conditions are plotted in Fig. 2.7. In Fig. 2.7, the horizontal axis represents time and the vertical axis represents vehicle position. The black clusters represent traffic congestions formed by the stopped vehicles. It is assumed that a hazard happens, and normal traffic flow turns into panic traffic flow at 300 s. After 300 s, vehicle trajectories become different, as shown in Figs. 2.7a and 2.7b. It is found in Fig. 2.7 that the results of normal and panic traffic flow exhibit different congestion patterns. Congestion clusters in normal traffic are more concentrated than those in panic traffic. Due to larger fluctuation of vehicle velocity, the congestion clusters in panic traffic are more sparsely located. However, panic flow has more congestion clusters and a larger congestion area than those in normal flow.

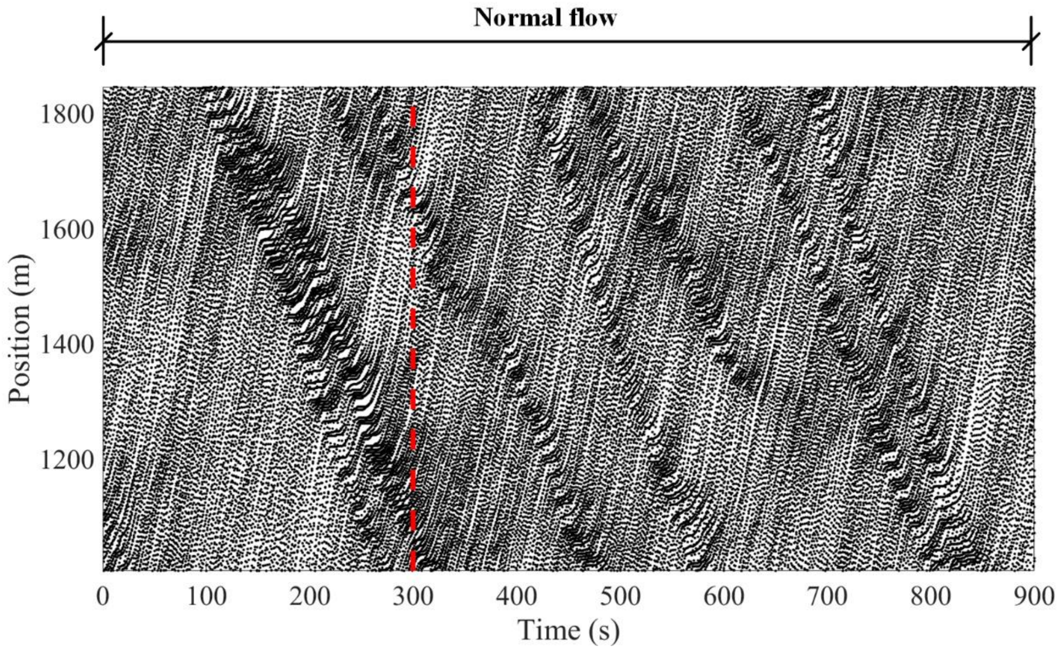

(a) Normal flow (Note: no hazards happen)

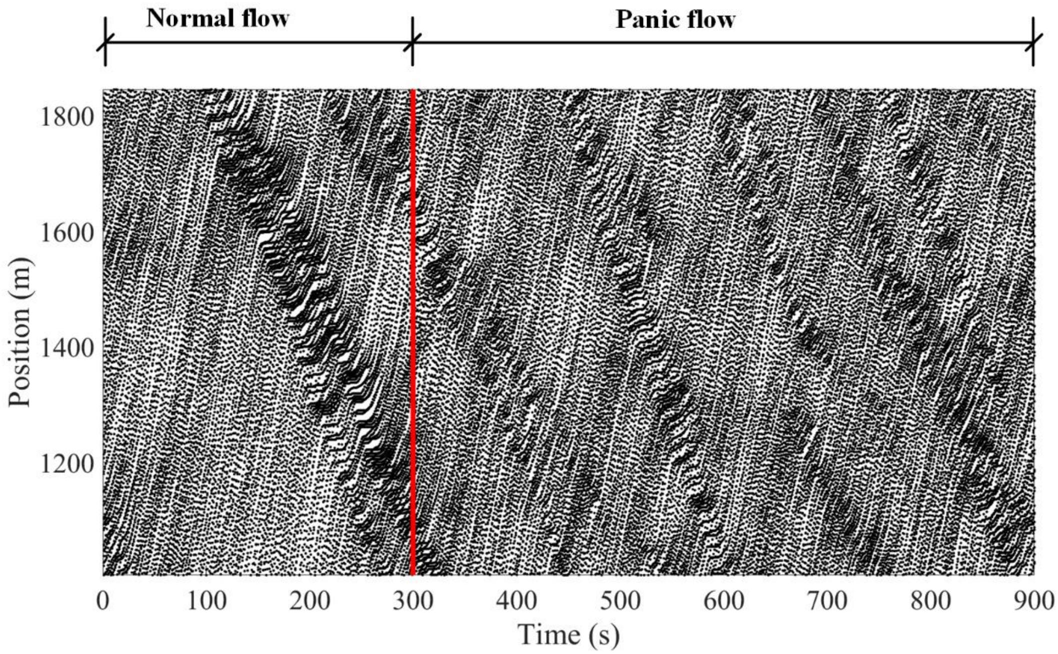

(b) Normal to panic flow (Note: a hazard happens at 300 s)

Figure 2.7 Time-space diagram of congested traffic flow on the bridge

Time history of live loads on the bridge under congested flow is plotted in Fig. 2.8. Local peak values of live load indicate congested traffic. It is found the largest live load on the bridge due to normal traffic is 6,641 kN at about t = 1050 s, while the largest value due to panic traffic is 7,187 kN at about t = 2800 s, which increases by 8.2 %. This indicates that the bridge may experience larger live load in congested flow under panic driving conditions than in normal driving conditions. Because there is no congestion in free, moderate and busy flow, concentrating loads do not form locally on the bridge. Thus, the loading condition of the bridge under panic and normal driving conditions do not exhibit significant differences for traffic flows with low traffic occupancy.

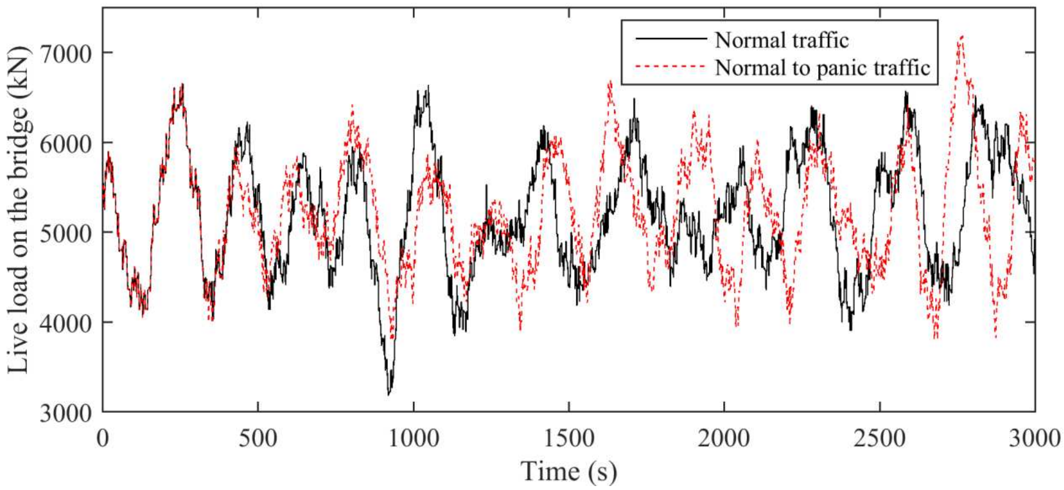

Figure 2.8 Time history of live load due to congested flow on the bridge

2.3.4.2 Time history of individual vehicle velocity

The velocity time histories of a representative truck in free, moderate and busy flow for two types of traffic scenarios are shown in Figs. 2.9a, 2.9b and 2.9c, respectively. One type of traffic scenario is the one including the transition from normal to panic traffic due to the hazard occurrence (labeled as "normal to panic traffic"). For comparison purposes, the results of the other type of traffic scenario, labeled as "normal traffic", which is the normal traffic flow without the occurrence of any hazards, are also plotted in Figs. 2.9a-c. It is found in Fig. 9 that the mean velocity of the truck (about 19 m/s) in free flow is higher than moderate flow and busy flow (about 15 m/s and 11 m/s, respectively) due to more open space for vehicles to maneuver. It is shown in Fig. 9(a) that the maximum velocity of this truck increases from 20 m/s to 25 m/s and the minimum velocity decreases from 18.5 m/s to 14.5 m/s. This is because there are more drivers who change their driving behavior from normal to aggressive behavior after the hazard occurs. Similarly, truck velocity fluctuates more dramatically after the hazard than before in moderate and busy flow. However, the impact due to aggressive driving behavior on the vehicle in moderate and busy flow is less significant than that in free flow.

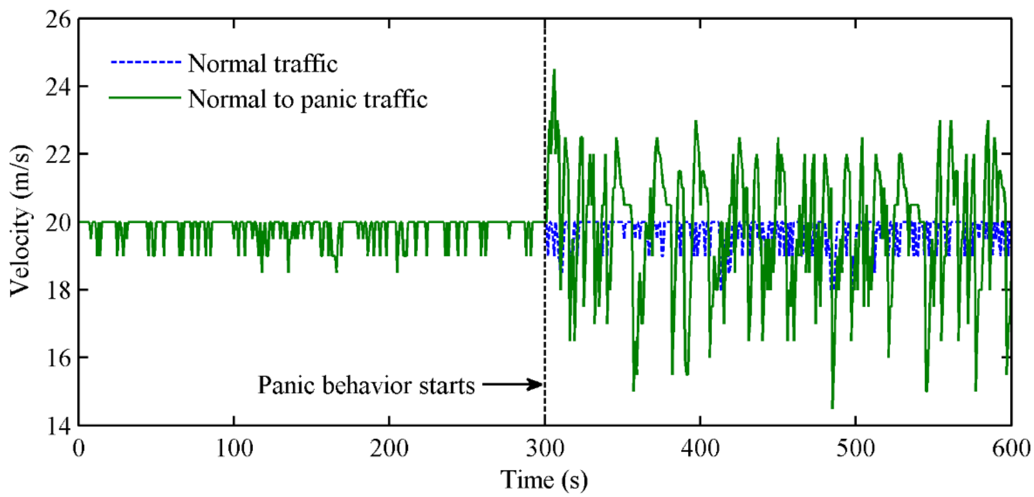

(a) Free flow

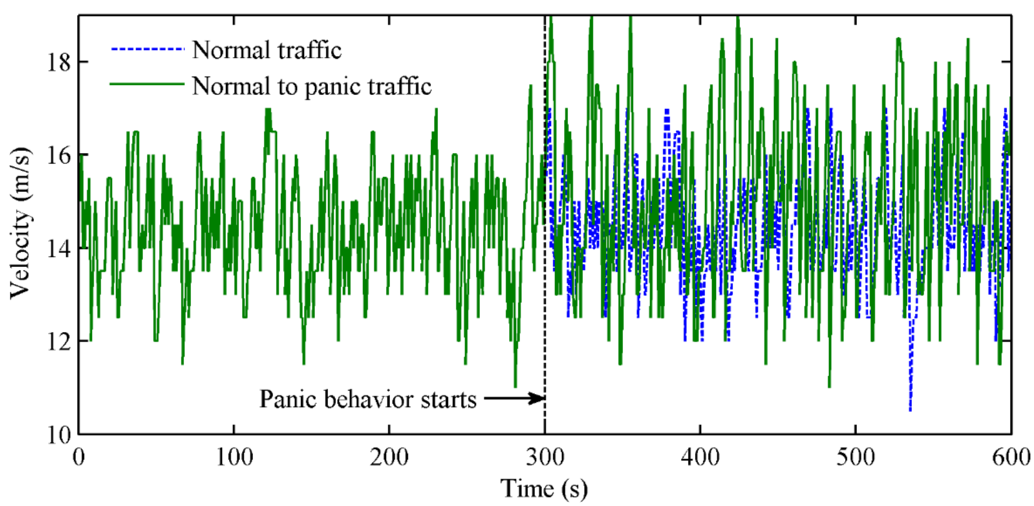

(b) Moderate flow

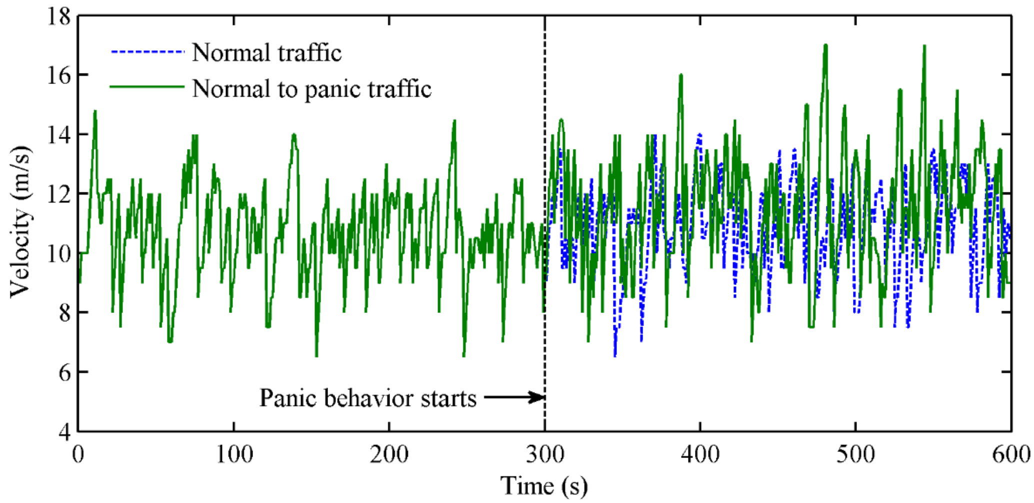

(c) Busy flow

Figure 2.9 Time history of velocity of a truck in traffic flows with different densities

2.3.4.3 Influence of panic driving behavior on vehicle dynamic response

Panic driving behavior may lead to the increase of vehicle driving speed in hazardous conditions, which may further affect the vehicle dynamic response as well as its safety situation. It is known that infrastructure details, vehicle properties, and hazard types can significantly affect vehicle response. In order not to lose generality, no specific hazard is defined in this section and the focus will be on the impacts on vehicle response only due to the changes of traffic condition from normal to panic. To assess the potential impact on vehicle response, some basic information about vehicle-infrastructure interaction needs to be briefly introduced. The vehicles are modeled as a combination of several rigid bodies, wheel axles, springs, and dampers. The heavy truck model has two rigid bodies associated with 19 degrees of freedom (DOFs), including 8 independent vertical, 8 lateral and 3 rotational DOFs. The bus and car model have one rigid body with 12 DOFs, including 5 independent vertical, 5 lateral and 2 rotational DOFs. Each wheel axle is connected to main rigid bodies through one upper spring and damper each at left and right sides in the vertical and lateral directions. Each wheel axle on the ground has contact with the ground through one lower spring and damper on the left and right sides in the vertical and lateral directions. The vehicle dimensions and dynamic parameters can be found in the references (Zhou and Chen 2015a) and are not shown here for the sake of brevity.

Since a long-span bridge is involved and considerable wind usually exists at the deck height of long-span bridges, the steady-state wind speed is assumed to be 20 m/s and the wind direction is assumed to be perpendicular to the vehicle driving direction. The wind speed relative to the vehicle $U_R(t)$ can be obtained in Eq. (2.18a).

$$U_R(t) = \sqrt{(U_m + u(t))^2 + U_{ve}^2(t)} \tag{2.18a}$$

where U_m, u and U_{ve} are steady-state wind speed, turbulent wind speed and vehicle driving speed, respectively; t is the time instant. The yaw angle ψ is the angle between the direction of relative wind speed and the vehicle driving direction in the range from 0 to π, defined in Eq. (2.18b).

$$\psi = \arctan\left[U_m + u(t)/U_{ve}(t)\right] \tag{2.18b}$$

The wind forces acting on the vehicles have six components, which are drag force, side force, lift force, rolling moment, pitching moment and yawing moment. The wind forces can be expressed as the functions of $U_R(t)$, wind coefficient and vehicle dimensions, which can be found in the reference (Zhou and Chen 2015a). Vehicle dynamic analyses are conducted on the vehicles in the free traffic flow under excitations from road surface roughness and wind. Dynamic response time histories are obtained at each independent DOF of the vehicles.

It is assumed that the drivers detect the incident and respond with panic driving behavior starting at 300 s, which is the median time instant of the simulation time period. The same truck as the one with the driving speed history shown in Fig. 2.9a is selected as the representative vehicle for demonstration. The vertical, pitching, rolling and lateral displacements of the 1st rigid body of the vehicle over the time period including the transition from normal to panic traffic (with hazard occurrence) are shown in Fig. 2.10a-d, respectively. The vehicle response time history with normal traffic (without hazard occurrence) is also given in each direction for comparison. It can be seen that the extreme dynamic response of the vehicle has a significant increase in each direction after panic traffic starts. The extreme values of vehicle responses in both "normal traffic" and "normal to panic traffic" are obtained from 300 s to 330 s for comparison. For the "normal traffic", the extreme values of vertical, lateral, rolling and pitching displacements of the 1st rigid body of the truck are 0.0384 m, 0.0533 m, 0.0563 rad and -0.0125 rad, respectively. For the "normal to panic traffic", the extreme values of vertical, lateral, rolling and pitching displacements of the 1st rigid body of the truck are 0.0425 m, 0.0568 m, 0.0604 rad and -0.0128 rad, respectively. The extreme response of the vehicle increases from normal to panic traffic by 10.7 %, 6.6 %, 7.3 % and 0.8 % for vertical, lateral, rolling and pitching directions, respectively.

By comparing Fig. 2.10 with Fig. 2.9a, it is seen that the influence of panic driving behavior on the dynamic response of the vehicle is not as significant as that on the vehicle driving speed. However, the increase of the vehicle extreme dynamic response due to the change of driving behavior is still very remarkable especially in the vertical, lateral and rolling directions, suggesting that the change of normal to panic driving behavior may pose larger safety risks for the vehicles. Due to the limit of the scope, this study is to demonstrate the potential impacts of traffic flow on vehicle response and safety. More detailed investigations need to be made on a specific highway system subjected to a particular hazard in order to quantify the impact on the bridge structure performance and vehicle safety risks.

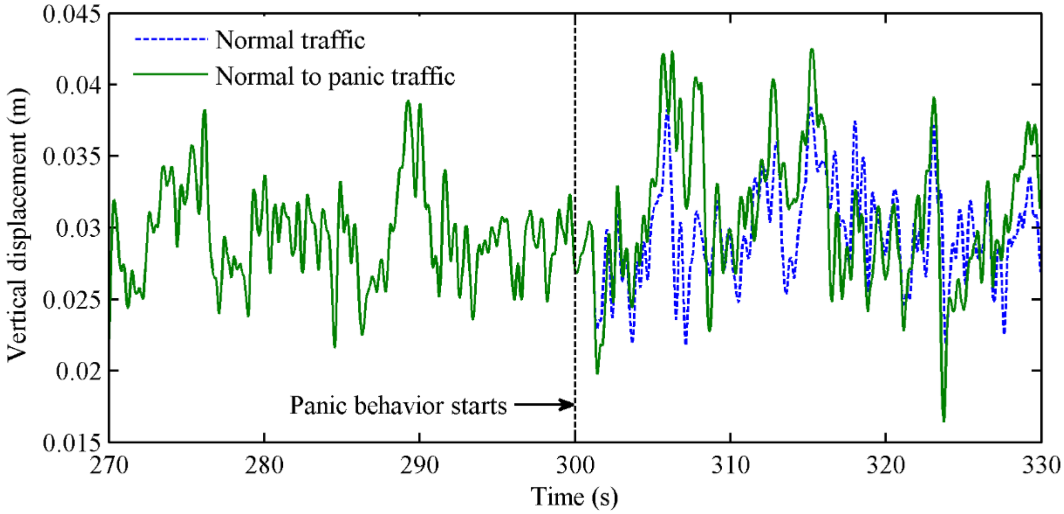

(a) Vertical displacement of the 1st rigid body

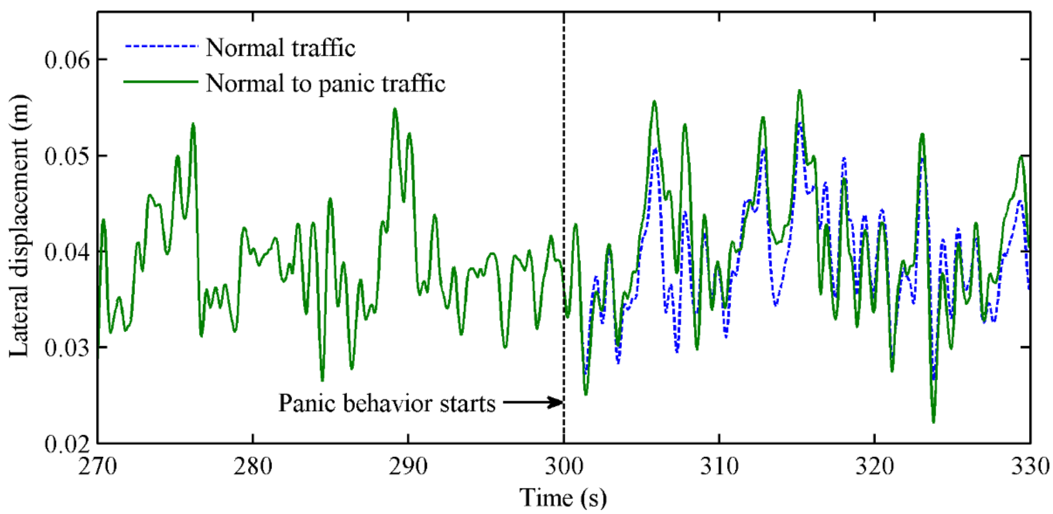

(b) Lateral displacement of the 1st rigid body

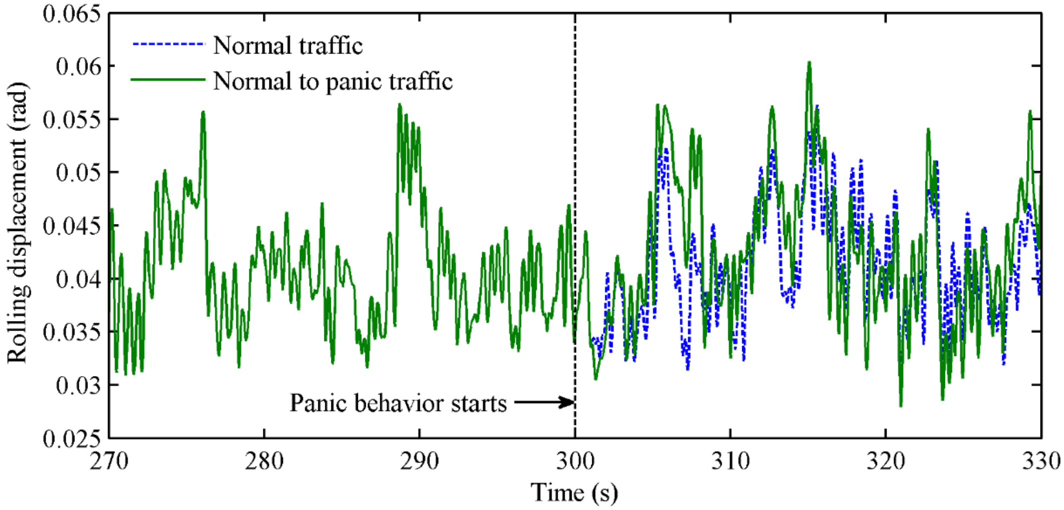

(c) Rolling displacement of the 1st rigid body

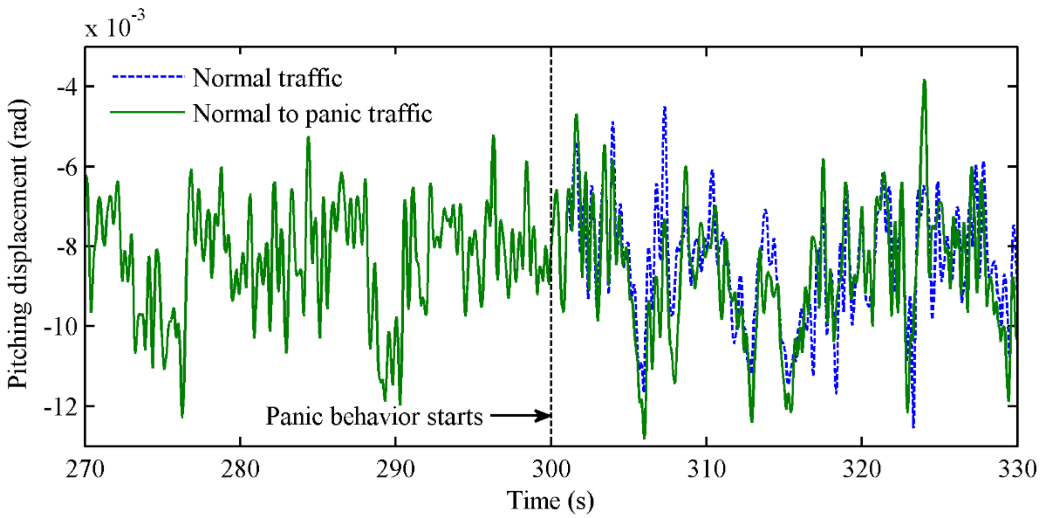

(d) Pitching displacement of the 1st rigid body

Figure 2.10 Time history of vehicle dynamic displacement of the representative truck in free flow

2.4 Conclusions

A new CA-based traffic flow simulation framework for hazardous driving environments is proposed, which considers more reasonable vehicle properties, anticipation effect, and different driving behaviors among drivers. This framework can provide traffic flow simulation under both normal traffic and hazardous (panic) traffic conditions. Both the overall traffic flow properties focusing on potential effects on highway infrastructure (e.g., bridges) and safety performance of individual vehicles in a “roadway–bridge–roadway” system are studied for a demonstration. Based on the demonstrative analysis results, the following conclusions can be made:

(1) Compared to the proposed model, the mean flow rate is overestimated if limited deceleration is not incorporated, while underestimated if anticipation effect is not incorporated. With limited deceleration, individual vehicles in the proposed model generally move slower and avoid unrealistic sudden braking. After anticipation effect is incorporated, an individual vehicle typically moves faster.

(2) Compared to the traffic under normal driving conditions, hazardous driving conditions can increase the mean traffic velocity when the occupancy is low. The standard deviation of the vehicle velocity is larger in the panic flow than the corresponding value in the normal flow, which is true for each type of drivers, especially remarkable for aggressive drivers in the free flow condition. In free flow, the mean standard deviation values are very similar among different drivers in normal traffic conditions. In both normal and panic traffic scenarios, the velocities of aggressive drivers have larger fluctuations than those of normal and timid drivers. The largest mean standard deviation of velocities occurs in congested flow for all types of drivers.

(3) In high-occupancy traffic, congestion will be formed under both normal and hazardous traffic conditions but with different congestion patterns. Compared to normal traffic, the time-space diagrams show that there are more congestion clusters distributed on the bridge under panic driving conditions than those under normal driving conditions, which have a larger size and are more sparsely located. Thus, the bridge may experience increased local concentrations of live loads on the bridge under high-occupancy traffic, which may become critical to a structure that has been partially damaged by the

hazards.

(4) Panic driving behavior is found to lead to larger extreme values and fluctuation of vehicle driving speeds. This is more remarkable in free flow than in moderate and busy flow. Panic driving behavior may significantly influence the extreme dynamic response of vehicles, especially in the vertical, lateral and rolling directions. The change from normal to panic driving behavior with increased speed fluctuations may suggest that some more attention should be paid to possible increased safety risks of the vehicles.

CHAPTER 3 TRAFFIC PERFORMANCE ASSESSMENT METHODOLOGY OF DEGRADED ROADWAY LINKS FOLLOWING HAZARDS[2]

3.1 Introduction

Post-hazard traffic networks are often disrupted due to not only direct impacts on transportation infrastructures, but also indirect impacts originated from interdependent nature with other infrastructure systems and environments. These indirect impacts include road blockage of debris from adjacent buildings, traffic accidents, fallen trees or light poles. For all these scenarios with partially-blocked roads and bridges following extreme events, traffic capacity and travel time are very different from those with intact road infrastructures and therefore become hard to predict. A new simulation methodology of traffic performance of partially-blocked roadway and bridge links due to hazardous events is proposed. This is based on improved microscopic-scale traffic flow simulation techniques that can be applied to degraded road/bridge links with various types of obstacles (different sizes, numbers and distributions). Following the validation with the published results of traffic congestion induced by a work zone, two typical partially-blocked scenarios due to infrastructure damage and accidents are numerically analyzed to demonstrate the feasibility of application to the traffic performance prediction of disrupted roadways due to extreme events. Parametric studies such as the impact of truck proportion, blockage configuration and traffic control measures are also conducted. It is found that the proposed framework can predict the traffic performance of degraded transportation systems due to various causes, which can lead to a wide array of future studies such as community resilience modeling, emergency response and evacuation planning, etc.

[2] This chapter is adapted from a published paper by the author (Hou, Chen and Han 2019) with permission from ASCE.

3.2 Formulations

3.2.1 CA-based traffic flow simulation algorithm on roadway links with partial obstruction

Cellular automaton (CA) model is a popular microscopic-scale traffic flow simulation method, which has been widely applied in many studies in normal traffic conditions (Nagel and Schreckenberg 1992; Fukui and Ishibashi 1996; Chowdhury et al. 1997; Barlovic et al. 1998; Knospe et al. 2000; Kerner et al. 2002; Bham and Benekohal 2004; Larraga et al. 2004; Lan and Chang 2005). A CA-based traffic flow model for hazardous driving conditions was recently developed by the authors (Hou et al. 2017). Compared to previous works, the model has several advantages, including consideration of more realistic acceleration and deceleration, driving behavior under hazardous conditions etc. Similar algorithms are adopted with significant improvements in this study to enable considering highways with any partial obstruction, including different numbers, shapes and distributions of obstacles on a highway.

The lanes of highways are discretized into many identical cells with a length of 0.5 m instead of 7.5 m in the traditional NaSch's model (Nagel and Schreckenberg 1992). With such a finer discretization, realistic properties of different types of vehicles (e.g. vehicle length, acceleration/deceleration) can be defined with sufficient accuracy to capture the realistic traffic features in heterogeneous traffic flow. For example, the acceleration/deceleration rate in the proposed model can be defined as a multiple of 0.5 m/s^2 instead of 7.5 m/s^2 in NaSch's model. To reproduce realistic smooth deceleration behavior, a safety criterion is adopted in the deceleration rule to consider the limited deceleration capability, which was firstly proposed by Lee et al. (2004). By satisfying Eq. (3.1), the velocity of vehicle i at the next time step $t+1$ can be obtained:

$$V_{i,safe}^{t+1} = max\left\{v \middle| \, v + \sum_{k=1}^{[v/M_i]}(v - M_i * k) \leq gap_i^t + \sum_{j=1}^{[V_{i+1}^t/M_{i+1}]}(V_{i+1}^t - M_{i+1} * j)\right\} \quad (3.1)$$

where $V_{i,safe}^{t+1}$ denotes the maximum safe velocity of vehicle i at time step $t+1$; V_{i+1}^t denotes the velocity of the front vehicle $i+1$ at time step t; M_i denotes the maximum deceleration rate of vehicle i; gap_i^t denotes the clear distance between vehicle i and the front vehicle $i+1$ in the current lane at time step t; $[x]$ denotes the nearest integer less than or equal to x.

Based on NaSch's single-lane CA model, the forwarding rules of the proposed model are given as follows:

Step 1, Acceleration.

$$V_i^{t+1} = min\left(V_i^t + a_i, V_{max}\right) \tag{3.2a}$$

Step 2, Deceleration.

$$V_i^{t+1} = min\left(V_i^{t+1}, V_{i,safe}^{t+1}\right) \tag{3.2b}$$

Step 3, Randomization with the probability p_r.

$$V_i^{t+1} = max\left(V_i^{t+1} - d_i, 0\right), \text{if } V_i^t - V_i^{t+1} < M_i - d_i \tag{3.2c}$$

Step 4, Movement.

$$x_i^{t+1} = x_i^t + V_i^{t+1} \tag{3.2d}$$

where x_i^t and V_i^t denote the longitudinal position and velocity of vehicle i at time t, respectively; V_{max} denotes the road speed limit; a_i and d_i are the normal acceleration and deceleration rates of vehicle i, respectively.

In addition to moving forward, vehicles on highways with multiple lanes will switch lanes for better driving conditions. The symmetric lane-changing rules are adopted in this model, which include the incentive criteria and safety criterion. Once the lane-changing rules are satisfied, a vehicle will perform a lane-changing maneuver with a probability of p_{ch}.

The incentive criteria:

$$gap_i^t < min\left(V_i^t + a_i, V_{max}\right) \tag{3.3a}$$

$$gap_{i,f}^t > gap_i^t \tag{3.3b}$$

The safety criterion:

$$gap_{i,b}^t > min\left(V_{i,b}^t, V_{max}\right) \tag{3.4}$$

where $gap_{i,f}^t$ is the clear distance between vehicle i and the nearest vehicle in the target lane ahead of vehicle i at time step t; $gap_{i,b}^t$ is the clear distance between vehicle i and the nearest vehicle in the target lane behind vehicle i at time step t; $V_{i,b}^t$ is the velocity of the nearest vehicle in the target lane behind vehicle i at time step t.

To study partially-blocked scenarios, the algorithms developed for intact roads (i.e. no any blockage) (Hou et al. 2017) are modified by introducing the concept of "dead cell" to represent any obstacle. When there is no obstacle on the road link, all the cells are "live cells" and each "live cell" can be open or occupied by only one vehicle at any time step. For scenarios with partial blockage, depending on the footage of the blocked area, the corresponding cells of the blockage will become "dead cells", which cannot be occupied by any vehicle for the time duration of the blockage. Such "dead cells" can be those covered by debris, fallen trees, light poles, construction equipment or pulled-over vehicles for different durations of simulation time periods. When a vehicle reaches the dead cell, it may switch lanes by following the lane-changing rules. Even for more complex scenarios, such as the lane being gradually narrowed, or the presence of detouring or warning signs, the corresponding cells can also be adjusted accordingly to become "dead". Once the blockage is cleared, the corresponding "dead cells" will become "live cells" again. In this way, the traffic flow simulation of roadways with any type of blockage (obstruction) (e.g. number, size, location) can be easily simulated by taking advantage of existing advances on CA-based algorithms. Furthermore, the adoption of "dead cells" and "live cells" also offers flexibility to simulate the time-progressive traffic flow throughout the occurring and recovery processes of a hazard.

3.2.2 Representative post-hazard scenarios of partially-blocked roadway and bridge links

A typical traffic network is often separated into some nodes, roadway and bridge links based on topological and design features. Following typical extreme wind events, roadway or bridge links may suffer long-term (months to years), short-term (hours to days) and temporary (minutes to hours) disruptions from different causes, such as damaged bridge/pavement, work zone for maintenance/construction, debris, fallen trees/light poles, or accidents (Fig. 3.1). These disruptions, despite different nature, are reflected in the proposed CA-based traffic flow simulation that different number of cells become "dead" for different durations of time. A road or bridge is practically closed to traffic under several situations: 1) sections of a roadway or bridge are fully blocked physically by obstacles; 2) there are still small gaps between obstacles on the road or bridge links. But the gaps are small enough to deter or discourage people from using the road; and (3) the road or bridge is closed by traffic authority or law enforcement. The focus of this study is on the partially-blocked scenarios that are still open to traffic. Table 3.1 summarizes some typical partially-blocked scenarios due to various incidents in real life.

Table 3.1 Different disruption types and their causes

Disruption type	Example causes
Long-term	• Damaged bridges or pavement causing partial closure
	• Work zone for maintenance/construction, etc.
Short-term	• Large debris from damaged buildings due to some hazards
	• Fallen trees and light poles.
Temporary	• Vehicle accidents. Pulled-over vehicles
	• Temporary repair

By adopting appropriate models to simulate structure fragility, debris distribution, and accidents, the specific disrupted infrastructure scenarios can be characterized. Accordingly, roadways/bridges will have a certain number of “dead cells” distributed in corresponding patterns and for certain time periods (e.g. long-term, short-term or temporary), depending on the scenario. The sizes and distributions of these “dead cells” due to obstacles have large variations and uncertainties. Fig. 3.1 gives the illustrative views of CA-based simulation model with partial blockages of three typical types of scenarios.

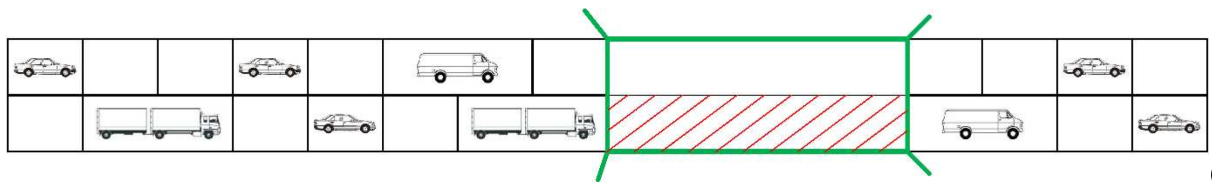

(a)

Long-term disrupted infrastructure (e.g. partially-blocked bridges)

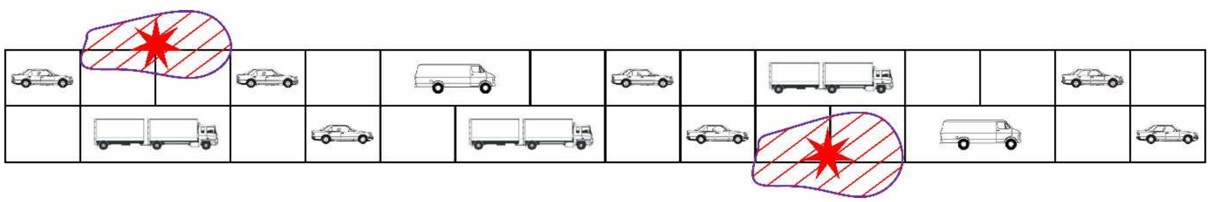

(b) Short-term degraded infrastructure (e.g. by debris)

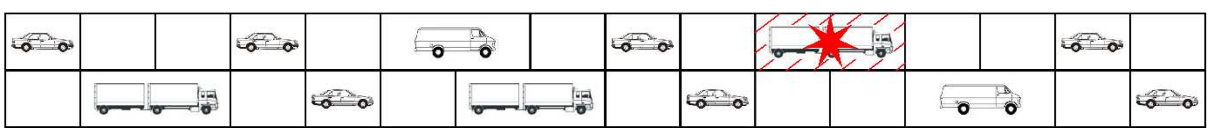

(c) Temporarily degraded infrastructure by accidents and emergency response

Figure 3.1 Typical scenarios of disrupted infrastructure of transportation system

Based on the traffic flow simulation results, traffic performance assessments, including those with some popular transportation functions (e.g. travel time function), can be conducted to support any traffic network-level studies of resilience. In the following sections, after the model validation is conducted, a demonstrative study is made to investigate the feasibility of applying the CA-based traffic flow simulation techniques to conduct traffic flow simulation of disrupted roadway links.

3.2.3 Model validation

Due to the unavailability of post-hazard traffic data, the proposed traffic flow simulation model is validated with the published data of traffic congestion induced by a work zone (Fei et al. 2016). In the reference, the length of the studied two-lane highway system was 3,500 m, and the length of the work zone was 800 m. Two types of vehicles including fast vehicles and slow vehicles were considered in the traffic, which had the maximum velocity of 28 m/s and 17 m/s, respectively. The ratio of the fast vehicles to the slow vehicles was 1/3. The proposed model adopts the same parameters to replicate the same scenario for validation purposes. The flow-density diagram from the simulation result of the proposed framework is compared with that from the reference and presented in Fig. 3.2. It can be seen the simulation result has good agreement with the published data. The small discrepancy is likely due to the difference in model details between two simulation models, e.g. lane changing rules and position updating rules. Therefore, this framework is found to have reasonable prediction accuracy for the selected disrupted scenario and will be used to simulate other disrupted scenarios in the following study.

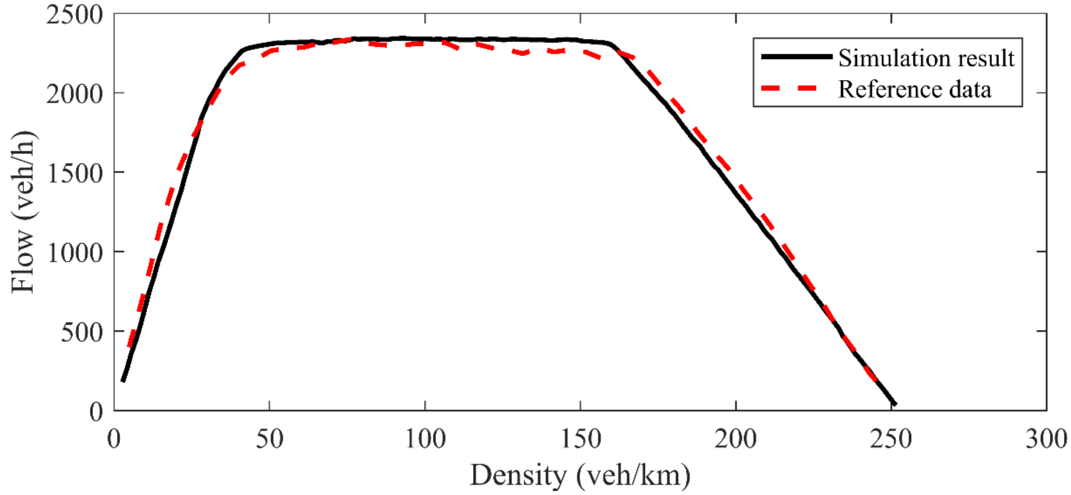

Figure 3.2 Flow-density diagrams from the simulation result and the reference data

3.3 Demonstrative simulation of partially-blocked roadway links following extreme events

3.3.1 Disrupted scenarios and model parameters

A two-lane road link of 2,000 m is selected in the following demonstrative study. There is no traffic light, major entrance and exit on this segment. The speed limit of the road segment is set as V_{max} = 30 m/s (108 km/h). To study heterogeneous traffic flow on highways, three types of vehicle groups are considered (i.e. cars, buses, and trucks). The lengths of cars, buses, and trucks are defined as 5 m, 10 m and 19 m, respectively (Oketch et al. 2004). The normal acceleration/deceleration rate of a car is set to be 1.5 m/s^2, and that of a bus and a truck is set to be 1.0 m/s^2 (Hou et al. 2017). In this paper, only traffic flow on dry pavement is investigated. Following the study by Li et al. (2016), the maximum deceleration rate of all three types of vehicles on dry pavement is 5.0 m/s^2. Properties of different types of vehicles are summarized in Table 3.2. Initial positions of all vehicles on the road are randomly generated and their initial velocities are zero. The randomization probability is set as 0.1 and the lane-changing probability p_{ch} is assumed to be 1 (Zhu et al. 2009). In the numerical simulation, periodic boundary conditions are used. It should be noted that the parameters adopted in this study were selected with assumed values to demonstrate the methodology in this study. Like most microscopic traffic flow simulation tools, all the parameters need to be calibrated with site-specific actual traffic data to give customized results for transportation applications.

The computational formulas for the mean flow, density and mean velocity used in the numerical simulation are given as follows:

$$f = \rho \cdot \bar{v} \tag{3.5}$$

$$\rho = N/L \tag{3.6}$$

$$\bar{v} = \frac{1}{T}\sum_{i=1}^{T}\left(\frac{1}{N}\sum_{j=1}^{N} v_j\right) \tag{3.7}$$

where f is the mean flow, ρ is the density, $\bar{v}$ is the mean velocity, N is the total number of vehicles, L is the road length, T is the simulation time, v_j is the velocity of vehicle j. In each simulation run, the total simulation time period is 20,000 s and the time simulation step is 1 s. To capture the steady traffic flow characteristics, the simulation results of the first 10,000 s are discarded and only those of the last 10,000 s will be used.

Table 3.2 Vehicle properties

Vehicle type	Length (m)	a (m/s^2)	d (m/s^2)	M (m/s^2)
Car	5	1.5	1.5	5.0
Bus	10	1.0	1.0	5.0
Truck	19	1.0	1.0	5.0

The three types of disruptions as shown in Fig. 3.1 include time-dependent information of disruptions. From the simulation perspective, these three types of disruptions can be combined to two types of scenarios: (1) single extended partial blockage and (2) scattered multiple small partial blockages, which are shown in Fig. 3.3. In Scenario A, lane 1 is partially closed due to a damaged bridge/pavement or large debris (Fig.

3.3a). Because the road has periodic boundary conditions, the location of the disruption would have no influence on the traffic simulation results. In Scenario B, both two lanes are partially blocked by two small partial blockages such as caused by multiple wind-induced accidents or small debris (Fig. 3.3b). Existing studies suggested that multiple accidents may occur at the similar time due to a strong crosswind event (Chen and Chen 2010).

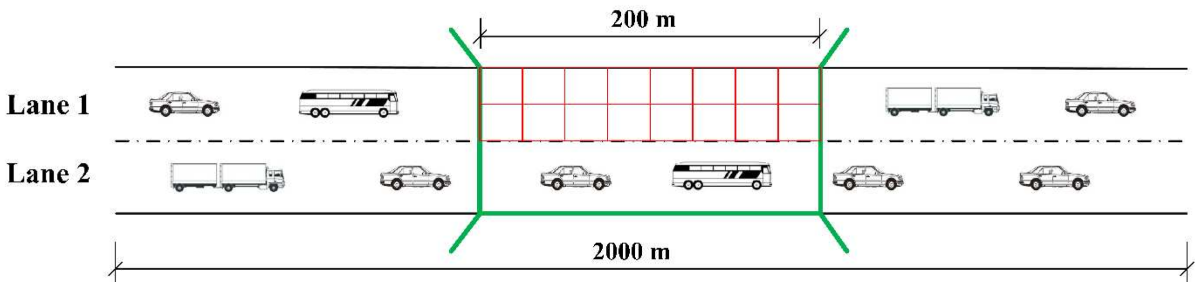

(a) Scenario A: single extended partial blockage (e.g. damaged bridge/pavement or large debris)

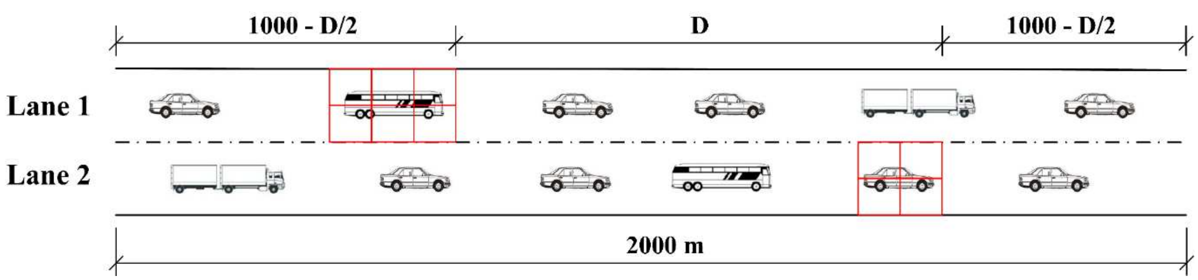

(b) Scenario B: scattered multiple small partial blockages (e.g. accidents & small debris)

Figure 3.3 Schematic illustration of two disrupted scenarios for simulation

3.3.2 Scenario of single extended partial blockage

3.3.2.1 <u>Traffic flow dynamics</u>

For the disrupted scenario induced by a single extended partial blockage as shown in Fig. 3.3a, we will firstly investigate the traffic flow dynamics. The proportions of cars, buses, and trucks in the traffic flow are assumed to be 80%, 10%, and 10%, respectively. The fundamental diagrams and lane-changing frequency are plotted in Fig. 3.4. Zhu et al. (2009) found three regions in the fundamental diagrams of disrupted traffic induced by an accident car, namely, unsaturated traffic, saturated traffic, and oversaturated traffic. Besides those three regions, a new transition region is found between unsaturated traffic and saturated traffic in Fig. 3.4. Four regions are separated by three critical densities, namely, ρ_1 = 17.5 veh/km, ρ_2 = 37.5 veh/km, and ρ_3 = 182.5 veh/km. When $\rho \leq$ 17.5 veh/km, the flow increases with the increase of vehicle density in a linear manner and finally reaches the maximum value at ρ = 17.5 veh/km, which is the traffic capacity. The mean velocity is nearly constant and close to the speed limit, 30 m/s. The lane-changing frequency is zero. This means there is no vehicle moving in lane 1, and all vehicles in lane 2 move with free-flow speed. When 17.5 veh/km < $\rho \leq$ 37.5 veh/km, the lane-changing frequency increases and mean velocity decreases significantly. The flow decreases from the traffic capacity to a stable value finally. In the saturated region (37.5 veh/km < $\rho \leq$ 182.5 veh/km), there is a largely flat plateau in the flow-density diagram, which is a typical phenomenon in disrupted traffic caused by local blockage. The mean flow rate is independent of density and remains very similar, although the mean velocity decreases with the increasing density. In the saturated region (ρ > 182.5 veh/km), the flow decreases with the increase of vehicle density in a linear way. The mean velocity and lane-changing frequency further decrease.

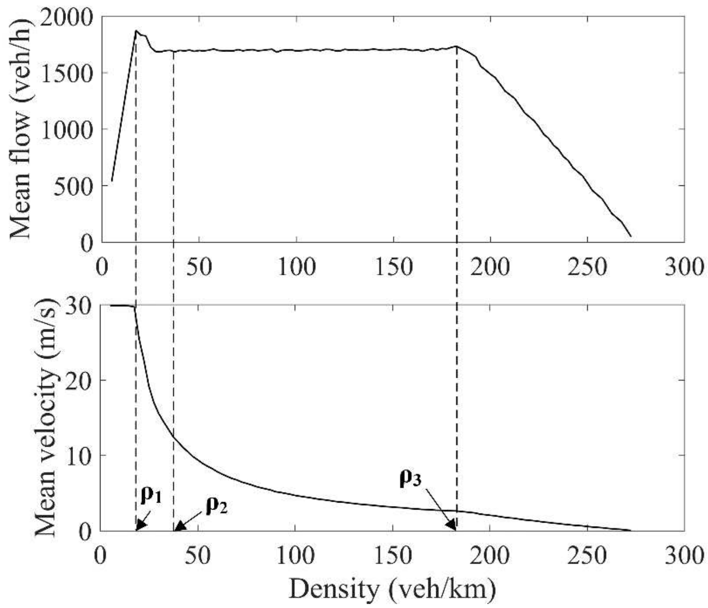

(a) Fundamental diagrams. (upper) flow-density diagram; (lower) velocity-density diagram.

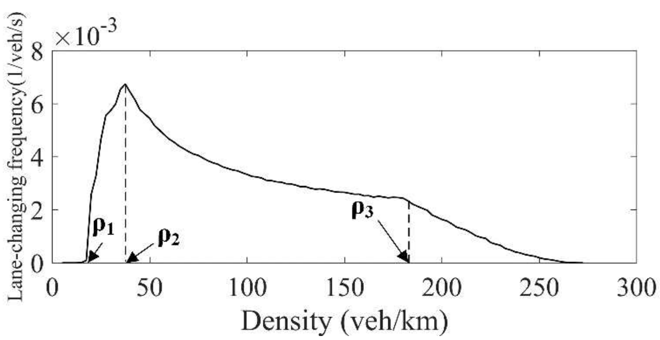

(b) Lane-changing frequency

Figure 3.4 Fundamental diagrams and lane-changing frequency

To gain more insight into the traffic dynamics under disrupted conditions, time-space diagrams at traffic density ρ = 17.5 veh/km and 20 veh/km are plotted in Fig. 3.5. Steep trajectory lines indicate that the velocities are rather low. Lane-changing behaviors are indicated by the disappearance and reappearance of the trajectory lines on the two lanes. The grid pattern region represents the blocked area. From Fig. 3.5a and 3.5c, it can be seen that there is no traffic in lane 1 and traffic flow on lane 2 is a free-flow traffic. This is because vehicles prefer moving in the unblocked lane, which has a much better driving condition in unsaturated traffic. As long as the unblocked lane can accommodate enough vehicles without causing any local jams, there will be no traffic in the blocked lane. When the traffic density increases to a higher value from the first critical traffic density ρ_1, traffic jams appear in both lane 1 and lane 2 (Fig. 3.5b and 3.5d). When vehicles on lane 1 approach the blockage (e.g. the damaged bridge), they slow down and then change to lane 2 for better driving conditions. Because these vehicles usually have low velocities after changing lanes and consequently prevent following vehicles in lane 2 from moving ahead, queues are formed in lane 2. After passing through the blockage, some vehicles in lane 2 change back to lane 1, where the driving conditions are better.

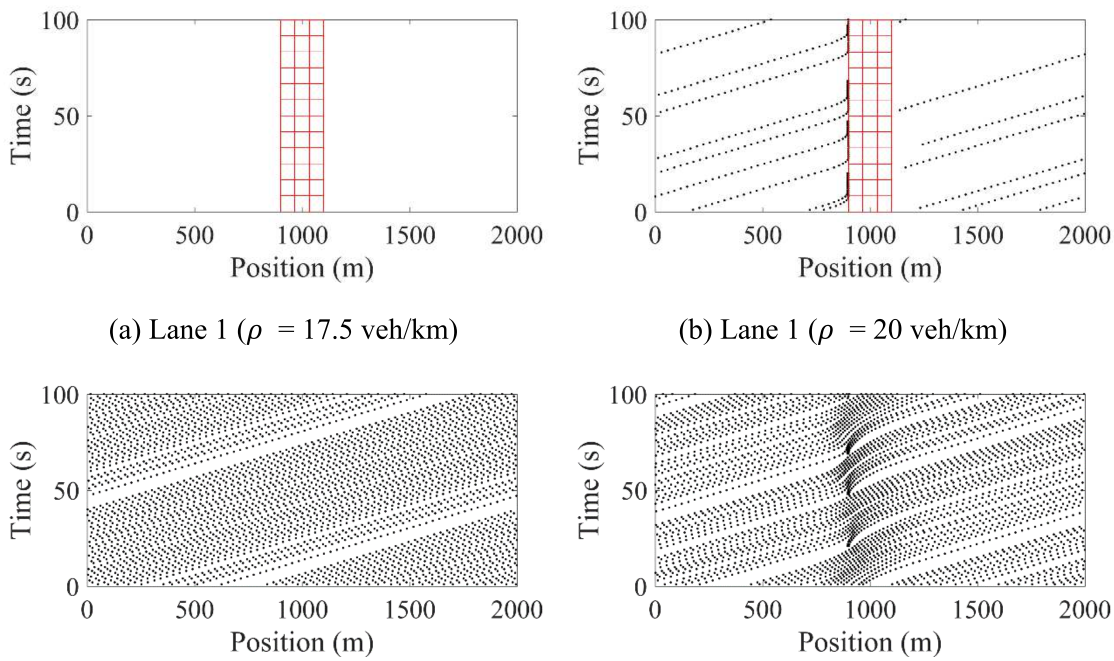

(a) Lane 1 (ρ = 17.5 veh/km) (b) Lane 1 (ρ = 20 veh/km)

(c) Lane 2 (ρ = 17.5 veh/km) (d) Lane 2 (ρ = 20 veh/km)

Figure 3.5 Time-space diagrams

3.3.2.2 Impact of truck proportion

In this subsection, we will investigate the influence of the proportion of trucks R_{truck} on the heterogeneous traffic flow. Here we fix the proportion of buses as 0.1 and change the proportion of trucks and cars. Traffic flow with the truck proportion R_{truck} = 0.1, 0.2, and 0.3 are investigated. Fig. 3.6 gives the fundamental diagrams for different truck proportion. Fig. 3.7 shows the lane-changing frequency of cars and trucks. A similar trend is observed on the flow-density and velocity-density diagrams (Fig. 3.6) for traffic flow with different truck proportions. As the truck proportion changes, there are still four regions on the diagrams and it is found in Fig. 3.6 that truck proportion has a negative effect on the flow and velocity in all traffic regions except the unsaturated region.

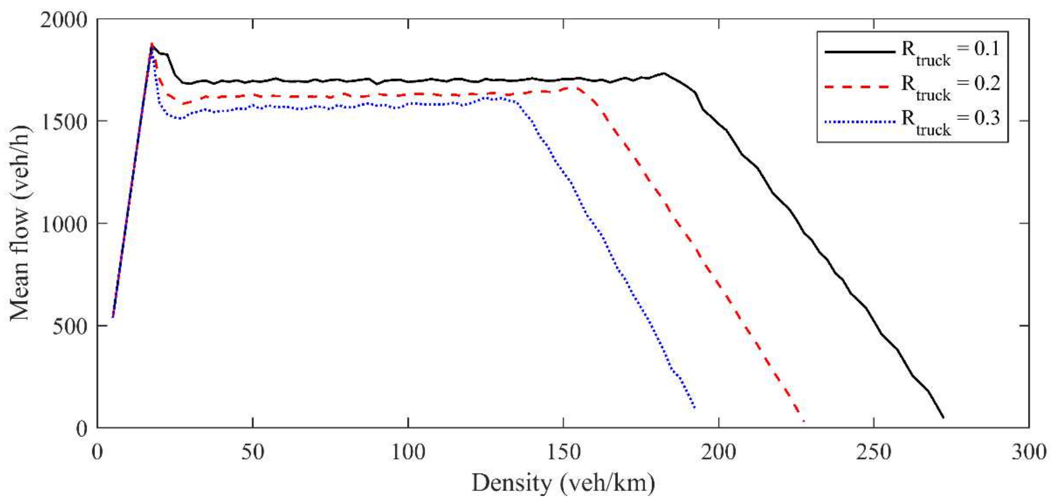

(a) Flow-density diagram

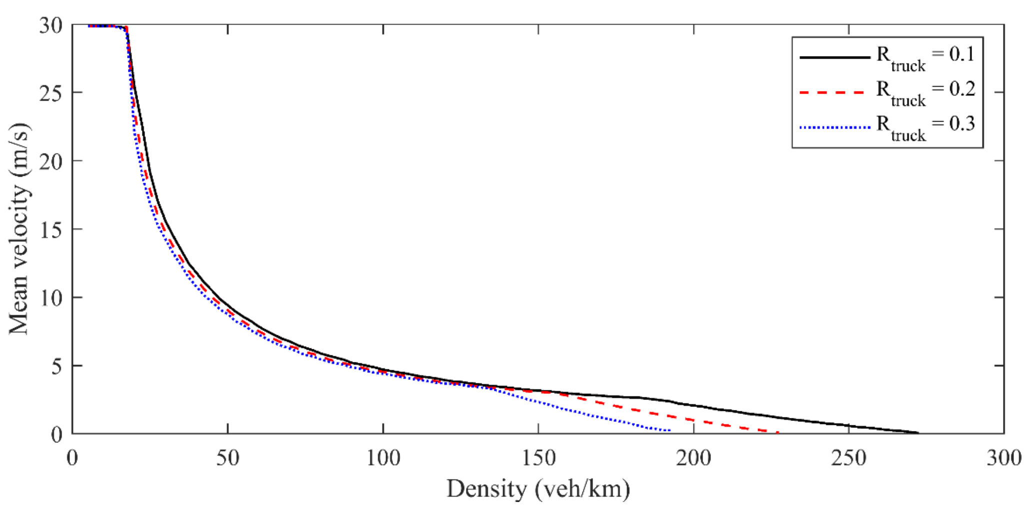

(b) Velocity-density diagram

Figure 3.6 Fundamental diagrams for different truck proportion

It can be seen from Fig. 3.7 that lane-changing frequency of cars is much higher than that of trucks in traffic with different truck proportions. This is because a truck is much longer than a car, making it harder for the truck to find sufficient space on the other lane to make a lane change. As shown in Fig. 3.7a and 3.7b, the increase of the truck proportion leads to the decrease of the critical density ρ_2 and ρ_3. It is also found that the lane-changing frequency of cars and trucks has a same trend: as the truck proportion increases, the lane-changing frequency remains zero in the unsaturated region, increases in the transition and saturated regions, and finally decreases in the oversaturated region. Such results are consistent with the recently published findings by Li et al. (2016). Meanwhile, compared to cars, the influence on the lane-changing frequency of trucks is more significant (Fig. 3.7). It is believed that the change of lane-changing frequency in different regions of traffic flow is caused by the lane-changing maneuvers of trucks. When the traffic density is high enough, trucks will try to obtain higher velocity by switching lane. The large gap caused by lane change of trucks will also prompt lane-changing maneuvers by other vehicles. In this case, more trucks on the road will cause higher lane-changing frequency. However, when the traffic density is very high, trucks seldom switch lane because of small space, which also hinders the lane change of other vehicles. In this situation, more trucks will lead to lower lane-changing frequency.

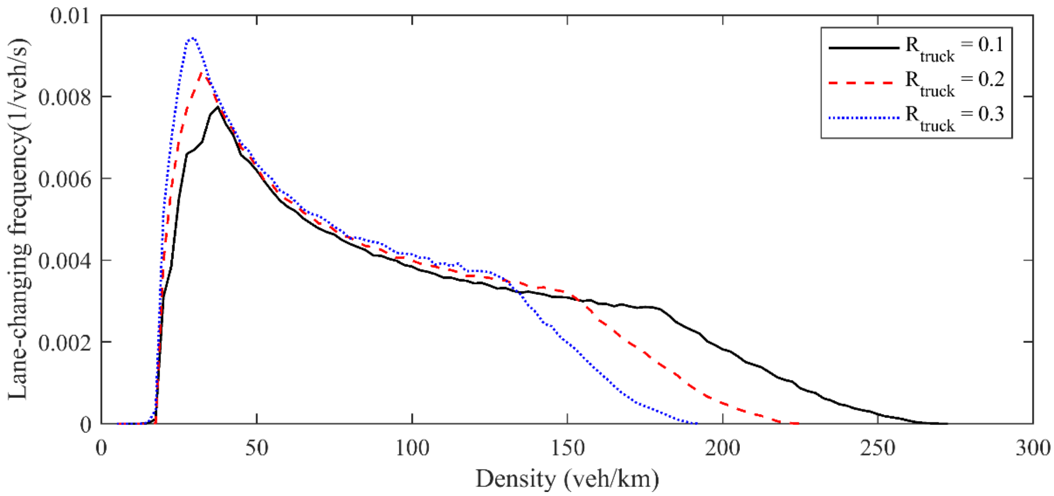

(a) Car

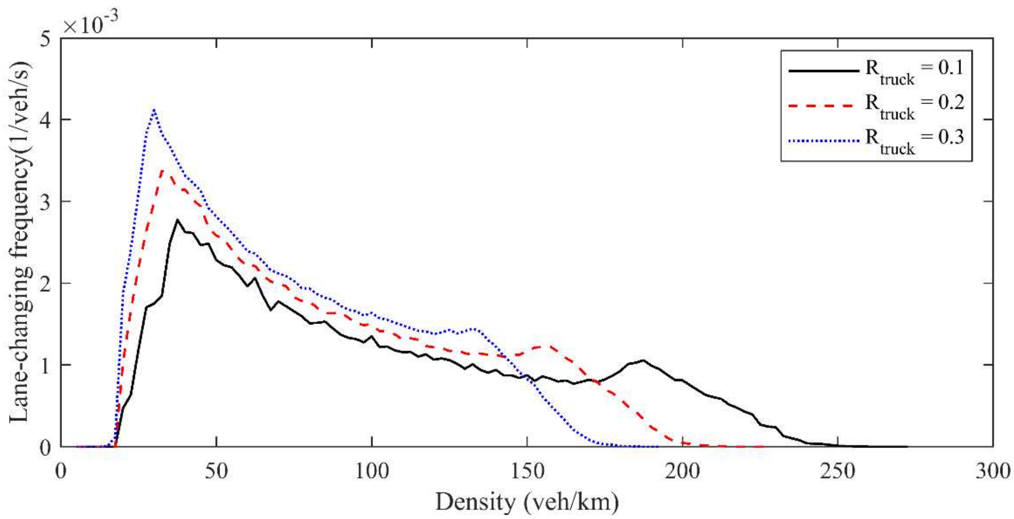

(b) Truck

Figure 3.7 Lane-changing frequency for different truck proportions

3.3.2.3 Impact of traffic control for heavy vehicles

Large vehicles, such as heavy trucks, often experience more frequent crashes in the lane reduction bottlenecks, e.g. work zones, road blockage due to fallen debris. In order to improve traffic safety, some traffic control measures are often implemented at lane reduction bottlenecks for the heavy vehicles, e.g. encouraging them to vacate the closed lane farther upstream; and setting a reduced speed limit for those vehicles. In this subsection, the impact of traffic control measures on the heavy vehicles, namely, trucks and buses, will be investigated. Two traffic control measures are applied to heavy vehicles, i.e., (1) restricting heavy vehicles to lane 2 at the initial state and setting the lane-changing probability of heavy vehicles as 0, namely prohibiting lane change of trucks in the area; (2) setting a reduced speed limit V_{hv}. After the traffic control measures are implemented, the trucks and buses can only move in lane 2 with a reduced speed limit V_{hv}, while the cars can move in both lanes with the normal speed limit V_{max}.

Fig. 3.8 shows the flow-density diagrams with and without traffic control. It is found that the transition region on the flow-density diagram disappears after the traffic control is implemented. In the unsaturated region, the flow rate with traffic control is smaller than the free flow without traffic control. That's to say, the unsaturated traffic becomes congested flow from free flow due to the traffic control. It is also found the flow throughout the whole density region decreases after the traffic control is implemented. Different speed limits of heavy vehicles V_{hv} mainly affect the unsaturated traffic. The higher the V_{hv} is, the lower the flow. Then, we further inspect the standard deviation of velocity of trucks, which is an important indicator of traffic safety performance.

Speed deviations of trucks with and without traffic control measures are plotted in Fig. 3.9. It can be seen that traffic control can greatly reduce the speed deviation of velocity of trucks and improve the overall traffic safety. For example, under traffic control with V_{hv} = 72 km/h, the maximum speed deviation of velocity of trucks is decreased by 39%. Fig. 3.10 presents the time-space diagrams of traffic flow under traffic control with V_{hv} = 72 km/h at density ρ = 15 veh/km. In Fig. 3.10, the black, blue and pink dots indicate cars, buses and trucks, respectively. Due to the traffic control, the trucks and buses only move in lane 2 and their speeds are relatively stable. Overall, traffic control of buses and trucks can improve traffic safety in terms of lower speed variation, although the traffic flow efficiency is reduced.

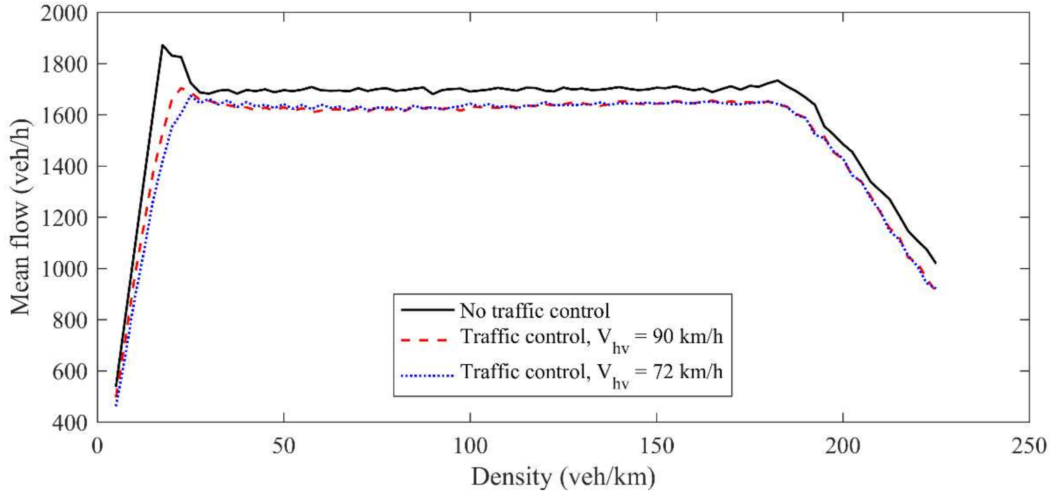

Figure 3.8 Flow-density diagrams with and without traffic control measures

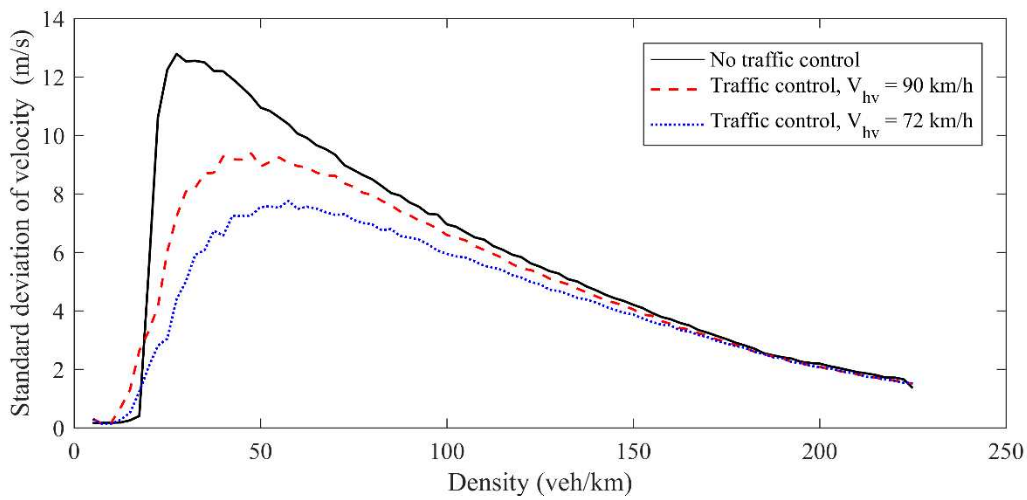

Figure 3.9 Speed deviation of velocity of trucks with and without traffic control measures

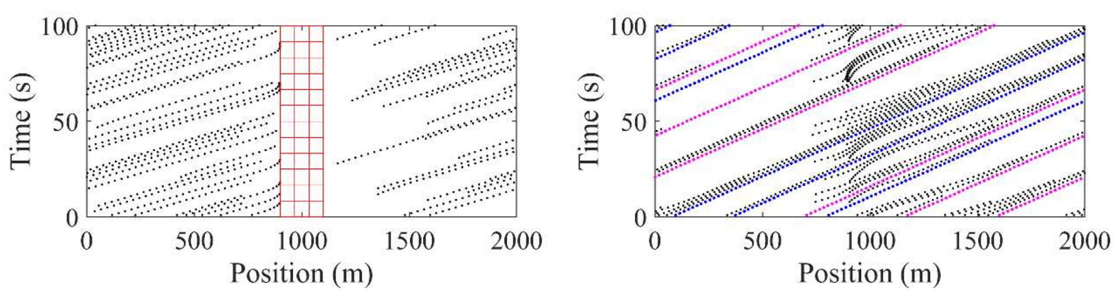

(a) Lane 1

(b) Lane 2

Figure 3.10 Time-space diagrams of traffic flow under traffic control

3.3.3 Scenario of scattered multiple small partial blockages

3.3.3.1 Traffic flow dynamics

In this section, we will investigate the disrupted traffic flow induced by two accidents or two small pieces of debris, as shown in Fig. 3.3b. This represents some scenarios that multiple accidents happen at the similar time, such as due to adverse driving conditions before or after some natural hazards. The proportions of cars, buses, and trucks in the traffic flow are assumed to be 80%, 10%, and 10%, respectively. The distance between two accidents is set as D = 800 m. The fundamental diagrams and lane-changing frequency are plotted in Fig. 3.11. It can be seen that three regions are also observed from the fundamental diagrams, namely, unsaturated traffic, saturated traffic, and oversaturated traffic. Throughout three regions, the mean velocity and lane-changing frequency decrease with the increase of density. In the unsaturated region, the flow increases as the density increases. However, the mean velocity is below the free-flow speed. This indicates that the two-accident traffic becomes congested even when the traffic density is very low. In the saturated region, a plateau is also found on the flow-density curve. It is interesting to find that the plateau is not fully flat, but with a very small negative slope, i.e. the flow rate decreases from 1840 veh/h to 1770 veh/h. It is likely due to the fact that the local increase of density cannot fully compensate for the reduced local velocity in this region. In the oversaturated region, the flow decreases with the increase of vehicle density in a linear manner.

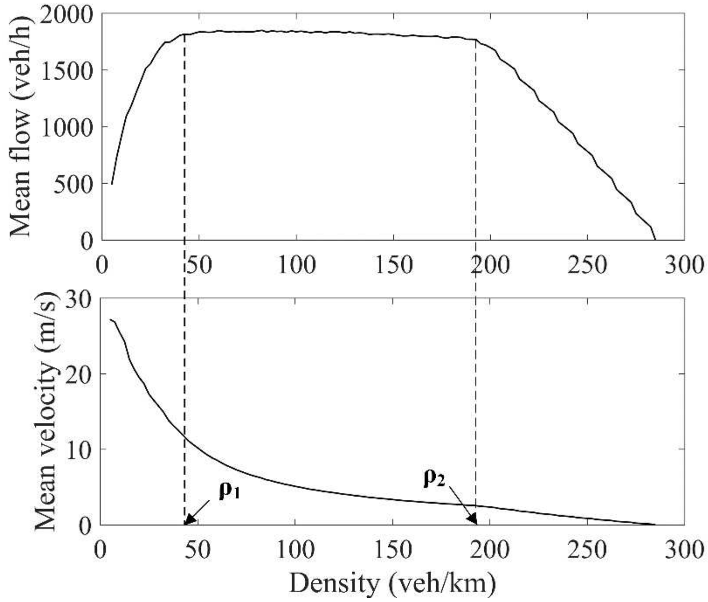

(a) Fundamental diagrams. (upper) flow-density diagram; (lower) velocity-density diagram.

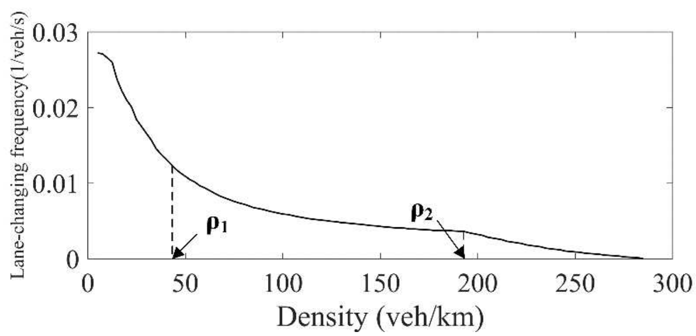

(b) Lane-changing frequency

Figure 3.11 Fundamental diagrams and lane-changing frequency

Time-space diagrams at traffic density ρ = 10 veh/km and 15 veh/km are plotted in Fig. 3.12. The shaded vertical bars indicate the accident locations. It can be seen in Fig. 3.12a and 3.12c that vehicle clusters appear near the accidents in both the blocked lane and through lane even at a relatively low traffic density (ρ = 10 veh/km). There are two congestion regions in each lane. This means that some vehicles need to slow down at least twice in order to finish the trip, and frequent braking makes the traffic flow unstable. When the traffic density increases to ρ = 15 veh/km (Fig. 3.12b and 3.12d, the cluster lengths become longer, and vehicles velocities become lower near the accidents.

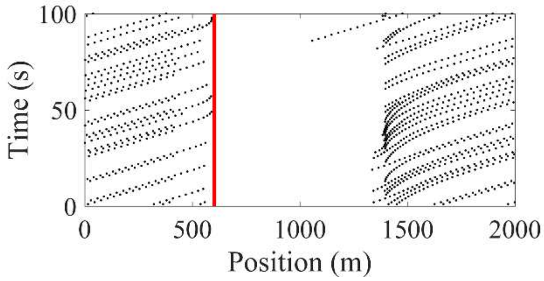

(a) Lane 1 (ρ = 10 veh/km)

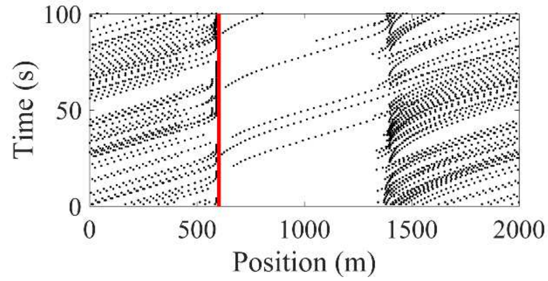

(b) Lane 1 (ρ = 15 veh/km)

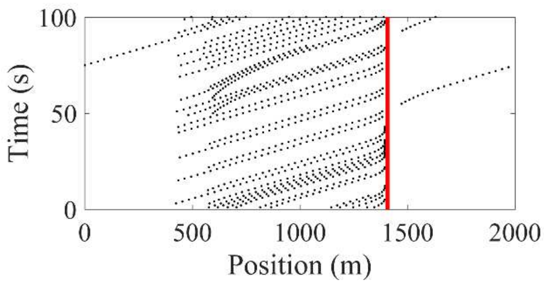

(c) Lane 2 (ρ = 10 veh/km)

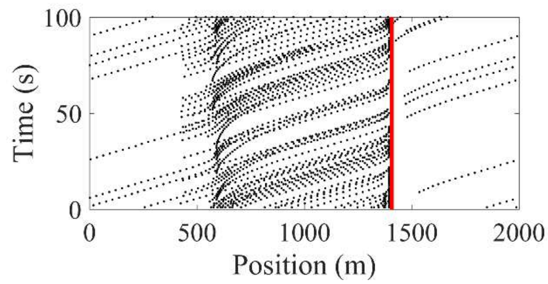

(d) Lane 2 (ρ = 15 veh/km)

Figure 3.12 Time-space diagrams

3.3.3.2 <u>Impact of blockage configuration</u>

Traffic flow characteristics are related to blockage configuration, such as the shape, dimension and distribution of blocked areas (Meng and Weng 2011). In this subsection, we will investigate the influence of the distance between two accidents D on the two-accident traffic. We assume the distance to be D = 100 m, 200 m, 400 m, 600 m and 800 m, respectively. The proportions of cars, buses, and trucks in the traffic are fixed as 80%, 10%, and 10%, respectively. Flow-density diagrams for traffic flow with different values of D are given in Fig. 3.13. It is found that the distance between two accidents mainly affects the flow rate in the saturated region. As the distance D increases, the flow rate increases. However, the flow rate has little change with different D when $D \geq 600$ m.

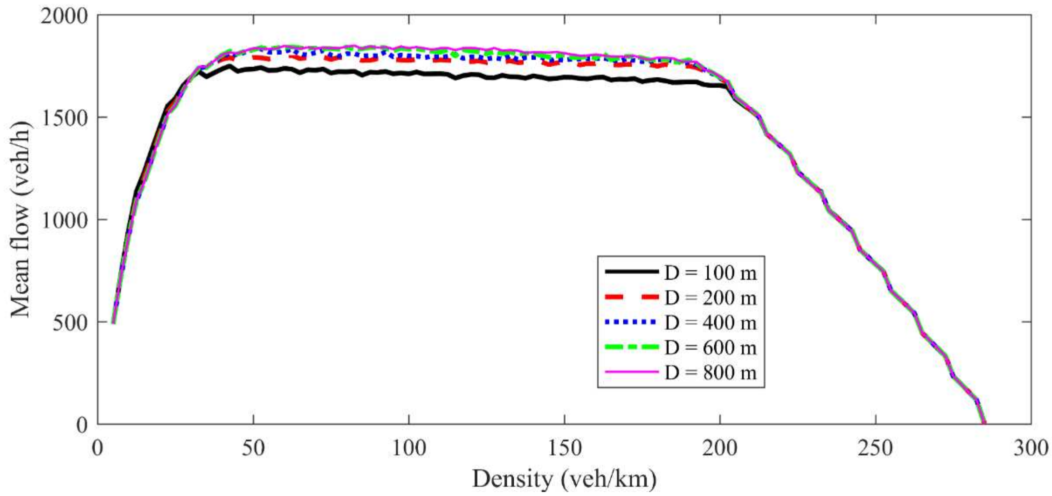

Figure 3.13 Flow-density diagrams for different distances between two accidents

Fig. 3.14 shows the lane-changing frequency for traffic flow with D = 100 m and 600 m. It is found that in the unsaturated region, the lane-changing frequency is higher when D = 100 m; in the saturated region, the lane-changing frequency is higher when D = 600 m; and in the oversaturated region, the lane-changing frequencies of two cases are very close. It can be found that the lane-changing frequency has different trends with the flow in different traffic regions: the influence of the distance between two accidents D on the flow can't be explained by the lane-changing frequency-density relationship in Fig. 3.14. An attempt is made in the following to further investigate the results in Fig. 3.13 by studying the lane-changing frequency at different positions along the road. Fig. 3.15 gives the spatial distribution of lane-changing frequency when D = 100 m and 600 m. Figs. 3.15a and 3.15b correspond to the lane-changing frequency at density ρ = 20 veh/km in the unsaturated region, while Figs. 3.15c and 3.15d correspond to the lane-changing frequency at density ρ = 60 veh/km in the saturated region. It can be seen from Figs. 3.15a and 3.15b that when the density is not very high, lane change mostly occurs near the accidents, e.g. 1000 m in Fig. 3.15a, and 700 m and 1300 m in Fig. 3.15b. Even if the total lane-changing frequencies are different for these two cases, they have very close flow rates because of their similar spatial distribution of lane change. When the density is high enough, lane change occurs in a wider area, as shown in Figs. 3.15c and 3.15d. The difference between these two cases with different D values is that the lane change distributes evenly when D = 600 m, while the lane change distributes unevenly when D = 100 m. The traffic flow efficiency is improved by more evenly distributed lane change, as the D increases. The ideal situation is the normal two-lane traffic without any blockages, which has the best traffic flow efficiency, because the lane change is evenly distributed throughout the whole road.

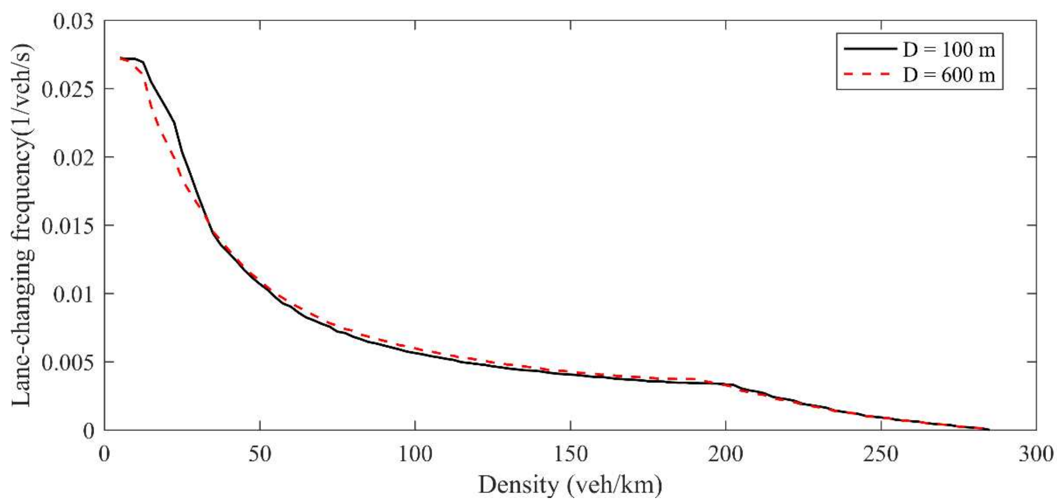

Figure 3.14 Lane-changing frequency for different distances between two accidents

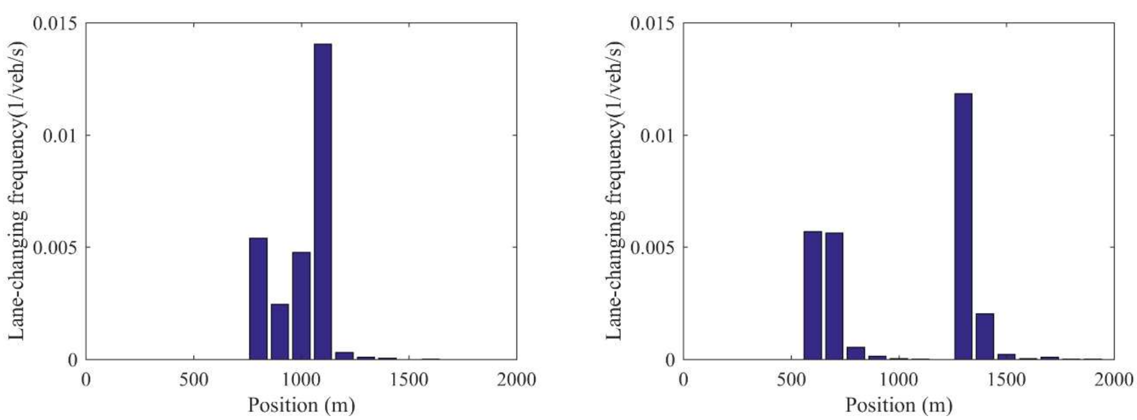

(a) D = 100 m, ρ = 20 veh/km (b) D = 600 m, ρ = 20 veh/km

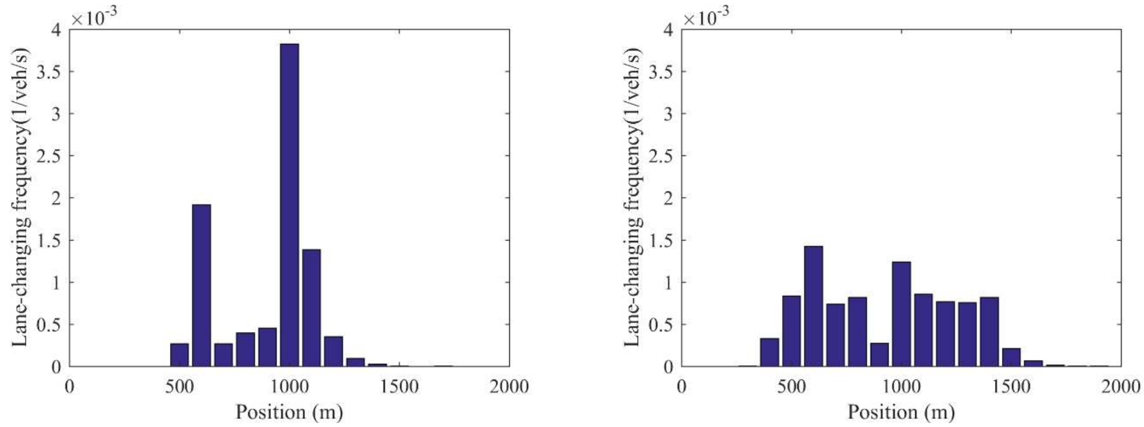

(c) D = 100 m, ρ = 60 veh/km (d) D = 600 m, ρ = 60 veh/km

Figure 3.15 Spatial distribution of lane-changing frequency

3.3.3.3 Impact of traffic control in accident area

Extreme events, such as strong winds, often cause vehicle accidents. Before vehicles involved in accidents are removed from roads, traffic control is often needed to prevent further accidents or injury. Usually, a warning sign is placed at the upstream of the accident scene, showing how far ahead the lane is closed, and often along with reduced speed limits. We will study the impact of traffic control schemes for the two-accident scenario in this subsection. The schematic illustration of the two-accident scenario with traffic control is shown in Fig. 3.16. The area between the warning sign and the first accident is called the restriction zone, and the area between the two accidents is called the accident zone. The lengths of the restriction zone and the accident zone are set to be 200 m and 800 m, respectively. Under the traffic control, vehicles in the restriction zone and accident zone will perform differently with vehicles in other areas. In the restriction zone, vehicles on lane 1 will try hard to switch to lane 2, and vehicles on lane 2 will not change to lane 1. Additionally, all vehicles in the restriction zone and accident zone must comply with the reduced speed limit V_{rs}. Therefore, the lane-changing rules are modified to consider these differences.

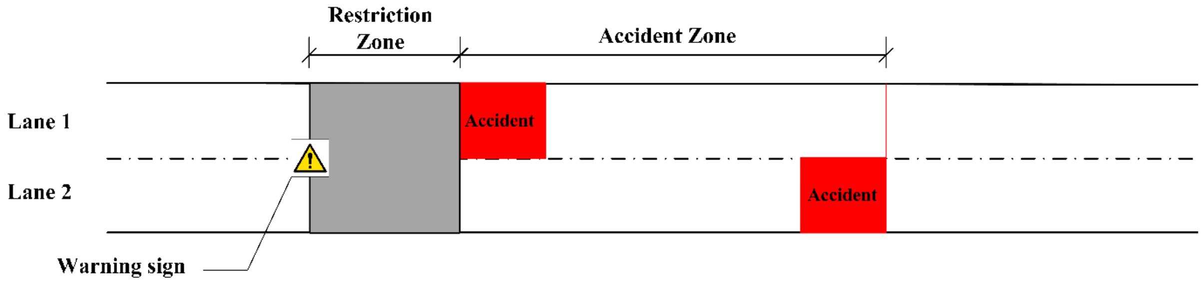

Figure 3.16 Schematic illustration of the two-accident scenario with traffic control

Now we evaluate the effect of different speed limit v_{rs} within the restriction zone and accident zone. Different speed limits v_{rs} = 36 km/h, 54 km/h, 72 km/h and 90 km/h are studied. Fig. 3.17 shows the flow-density diagrams by setting different speed limits in the restriction zone and accident zone. It is found that the flow decreases after the traffic control is enforced, and the speed limit v_{rs} has a negative effect on the flow. As the speed limit increases, the flow increases especially in the unsaturated region. This is consistent with previous research results (Lan et al. 2009). However, when the speed limit is larger than 72 km/h, the speed limit has a very limited effect on the flow. Fig. 3.18 gives the time-space diagrams under traffic control with the speed limit v_{rs} = 36 km/h and 72 km/h at density ρ = 20 veh/km. In Fig. 3.18, the black, blue and pink dots represent cars, buses and trucks, respectively. The black arrow indicates the position of the warning sign. It can be found the vehicle trajectories in the restriction an accident zone are steeper than those in other areas, indicating lower velocity in those areas. Moreover, as the speed limit v_{rs} increases, the cluster length in front of the accidents becomes longer, and more lane changes occur. It is also found that the vehicle clusters are mostly formed by large vehicles (buses and trucks) when the speed limit v_{rs} is relatively high (e.g. 72 km/h), which usually need to wait for longer time than cars before making a successful lane change.

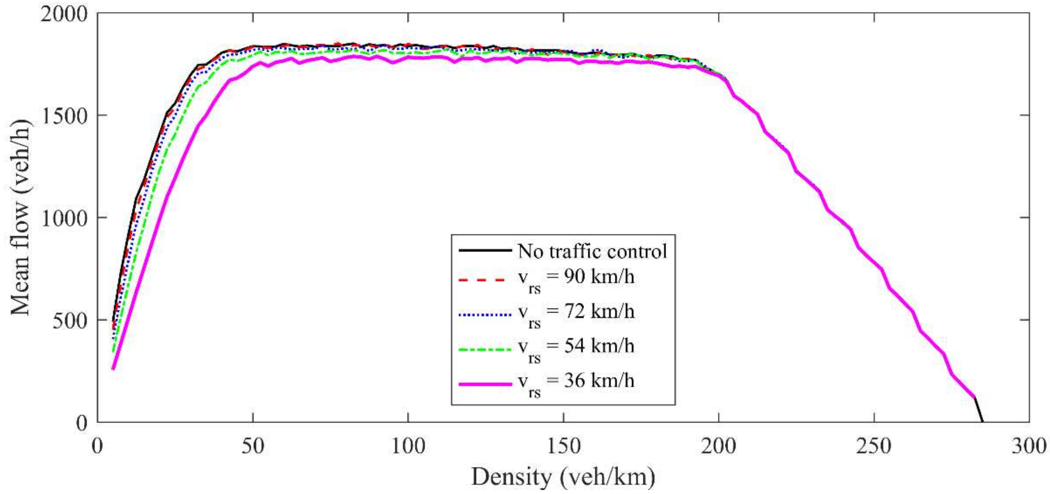

Figure 3.17 Fundamental diagrams with different speed limit

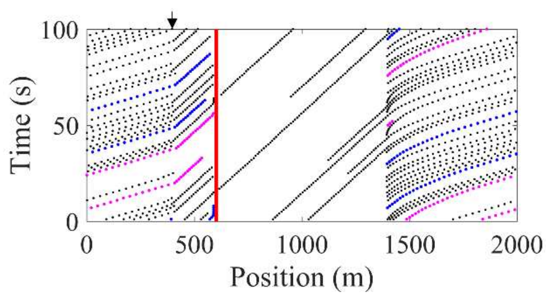

(a) Lane 1 (v_{rs} = 36 km/h)

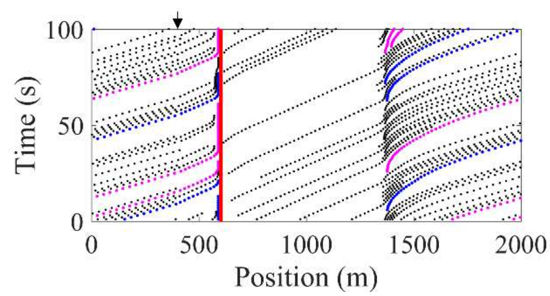

(b) Lane 1 (v_{rs} = 72 km/h)

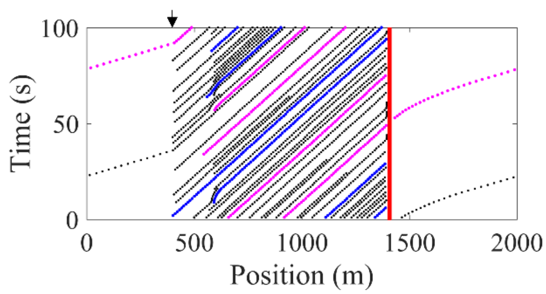

(c) Lane 2 (v_{rs} = 36 km/h)

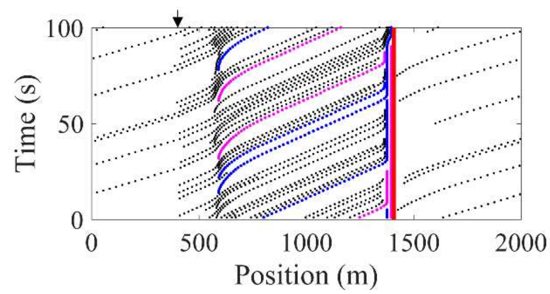

(d) Lane 2 (v_{rs} = 72 km/h)

Figure 3.18 Time-space diagrams

In order to find an appropriate speed limit in the accident scene, the standard deviation of the velocities of all vehicles by setting different speed limits v_{rs} are further investigated with the results displayed in Fig. 3.19. It is found that, in general, the standard deviation of velocities decreases as the speed limit v_{rs}

increases. However, when the speed limit v_{rs} is less than 54 km/h, the standard deviation of velocities increases with the increase of the speed limit at low-density traffic. Based on overall consideration, v_{rs} = 72 km/h is selected as the optimal speed limit, under which the flow is relatively large. Meanwhile, there is also relatively low standard deviation of velocity, which usually suggests lower traffic crash risks, such as rear-ends.

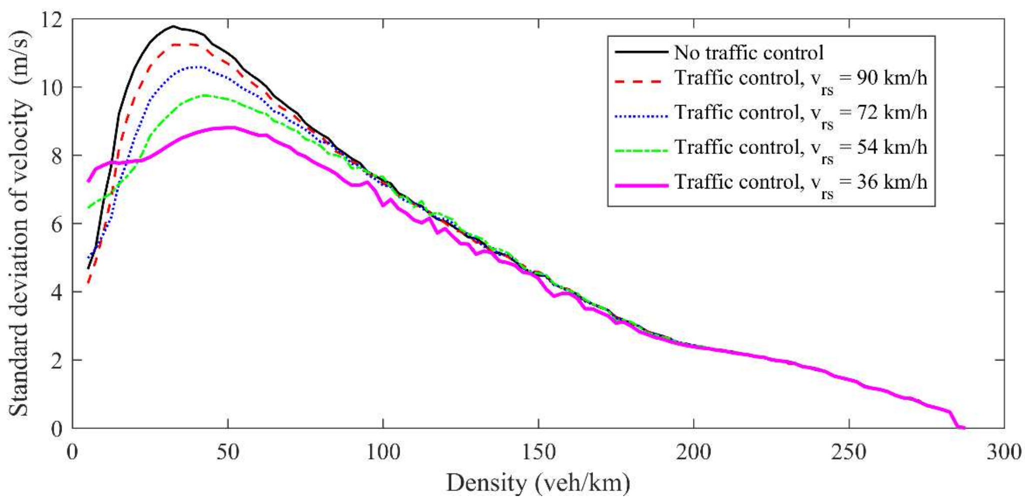

Figure 3.19 Standard deviation of velocity with different speed limit

3.4 Discussions and conclusions

In this study, a new methodology was proposed to study the traffic performance of degraded road links being partially blocked following extreme events. Firstly, by defining the stationary obstacles as “dead cells”, existing CA-based traffic flow simulation algorithms were modified to conduct the traffic flow simulation of roadways with partial traffic blockage scenarios induced by obstacles with any size and distributed pattern. Secondly, in the demonstrative example, two typical partially-blocked scenarios were further analyzed to demonstrate the feasibility of applying the proposed methodology to study the traffic performance of disrupted roadway links following extreme wind events. Although this methodology was proposed for the traffic study of disrupted bridge and roads following extreme wind events, it is noted that the same methodology can also be applied to disrupted scenarios due to other hazards.

In the numerical demonstrative study, the fundamental diagrams, time-space diagrams and lane-changing frequency were developed to investigate the traffic flow characteristics and traffic dynamics under various scenarios. The impact of truck proportion, blockage configuration and traffic control were also studied. The main findings of the numerical study can be summarized as follows:

(1) Four regions are found in the fundamental diagrams of disrupted traffic with single extended partial blockage (scenario A), namely, unsaturated traffic, transition traffic, saturated traffic, and oversaturated traffic.

(2) For scenario A, the truck proportion has a negative effect on the flow and velocity; traffic control of buses and trucks can improve the traffic safety in terms of lower speed variation, although the traffic flow efficiency is reduced.

(3) There are three regions in the fundamental diagrams, namely, unsaturated traffic, saturated traffic, and oversaturated traffic for the scenario with scattered multiple small partial blockages (scenario B).

(4) For scenario B, as the distance between two partial blockages increases, the traffic flow is improved by more evenly distributed lane change; traffic control in the accident area could improve traffic safety but reduce the flow, and an appropriate speed limit in the accident scene is deemed necessary.

CHAPTER 4 DEVELOPMENT OF TRAVEL TIME FUNCTIONS FOR DISRUPTED URBAN ARTERIALS WITH MICROSCOPIC TRAFFIC SIMULATION[3]

4.1 Introduction

Transportation networks are critical for post-disaster evacuation, emergency response and long-time recovery activities. Urban roads are easily disrupted during a disaster due to debris, traffic accidents or damages of other interdependent infrastructures. As a result, urban traffic networks consisting of some partially blocked roads (PBR) are often required to remain open to traffic before, during and after disasters because of their vital roles to hazard preparation, emergency response and recovery of urban communities. To conduct effective traffic planning of road networks involving PBR highly depends on accurate prediction of travel time on PBR, which is very different from those on intact roads. Due to the lack of appropriate models to predict the travel time on PBR, travel time prediction approaches of intact roads have been often applied to PBR, leading to inaccurate travel time estimates. Unrealistic travel time estimates of PBR as well as the whole traffic network further affect traffic planning, emergency response and other decision-makings which are heavily reliant on travel time prediction.

A new approach to develop travel time functions for PBR in urban areas is proposed to close this gap based on microscopic traffic simulation. After the proposed traffic flow simulation model is validated at microscopic and macroscopic levels with measured traffic data from an urban road, traffic simulations under various scenarios with different traffic volumes, truck ratios and blockage ratios are conducted through microscopic simulation experiments. A set of continuous traffic time functions are further developed for

[3] This chapter is submitted to a journal in a paper that is currently under review (Hou, Chen and Bao 2019).

disrupted traffic flow with parameters estimated from the generated traffic data. Comparison with the standard BPR function suggests that the standard BPR function would considerably underestimate the travel time for PBR and the proposed travel time functions can offer more realistic prediction.

4.2 Formulation of microscopic traffic simulation model

4.2.1 A typical PBR scenario

For urban transportation systems in the US, four-lane arterials (i.e. two lanes in each direction) and two-lane arterials (i.e. one lane in each direction) are the most popular arterial types. If one lane of a two-lane arterial is blocked, there will be no any traffic in that direction unless manual traffic intervention is applied, such as alternate one-way traffic for both directions. Such a scenario involves very low traffic capacity and is beyond the scope of the present study. This study will focus on the two-lane traffic in each direction on four-lane arterials. Depending on the specific hazard and surrounding environment, road links can be blocked in many ways. Traffic performance of a PBR is determined by the specific blockage scenario. One of the most common blockage scenarios for two-lane traffic is that one lane is partially closed, and the other lane is open to traffic, which is similar to the two-lane traffic with a work zone, as shown in Fig. 4.1. Although there are other more complicated blockage scenarios, this study will focus on the most typical disruptive scenario in Fig. 4.1. This is because other blockage scenarios either lead to full closure (e.g. multiple blockages near to each other) or can be simplified into the scenario being studied here (e.g. multiple blockages far apart).

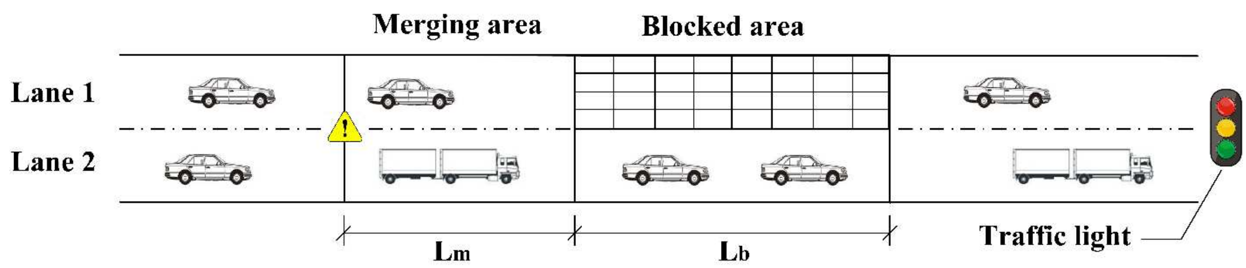

Figure 4.1 Schematic diagram of a road section with a blockage

As shown Fig. 4.1, a blocked area with a length of L_b is included in the road section. A warning sign is usually placed at the upstream of the blockage showing how far ahead the lane is closed, often along with reduced speed limit. The area between the warning sign and the blocked area is called merging area with the length of L_m , where drivers on the blocked lane will try to switch lane to the adjacent lane. In the meantime, vehicles often need to slow down to the reduced speed limit before moving into the blocked area. Any area beyond the blocked and merging areas is called normal area.

In some situations, warning signs may not be immediately available following an incident or a hazard before the traffic management is implemented. In this situation, the length of the merging area and reduced speed limit will depend on individual drivers and traffic conditions. Due to different driving behavior, timid drivers may merge lane far before the blockage, and drive slowly in the blocked area, while aggressive drivers may begin to merge lane very late and drive relatively fast.

As shown in Fig. 4.1, vehicles enter the road section from the left end of the figure and there is a traffic light at the right end with the cycle length of T. The durations of green-light, yellow-light and red-light phases are T_g, T_y and T_r, respectively. If a vehicle reaches the right end of the road section, it will leave when the traffic light is green and stop when the traffic light is red. During a change interval, drivers will stop or proceed through the intersection depending on the distance to the intersection and the driving speed.

4.2.2 CA-based model

In order to fully avoid unrealistic deceleration behavior mentioned in Section 1.2.4, an improved cellular automaton (CA) model is proposed for heterogeneous traffic flow on partially blocked urban roads by extending the two-lane safety driving (SD) model (Li et al. 2016). In this model, the lanes are discretized into many identical cells. Each cell is either empty or occupied by a vehicle at a time. Depending on the length of each individual vehicle, different numbers of cells may be occupied by each vehicle. The vehicle velocity is an integer varying from 0 to v_{max}, which is the maximum velocity of a vehicle. At each time step, the position and velocity of each vehicle are updated through the forwarding rule and lane-changing rule.

Open boundary conditions are used in this model. Vehicles enter the road section from the left end with a flow rate of q, and the time headway h is assumed to follow a displaced exponential distribution, which has a cumulative probability distribution $F(h) = 1 - e^{-\lambda(h-t_m)}$, where t_m is the minimum headway between vehicles and $\lambda = q/(1 - t_m q)$. We assume that the position of the left-most vehicle is x_{last}, and the maximum velocity and length of the new vehicle n are $v_{n,max}$ and l_n, respectively. If $x_{last} > v_{n,max} + l_n$ and vehicle n meets the time headway condition, it will enter the system at the position of $x_n = min(x_{last} - l_n - v_{n,max}, v_{n,max})$ with a velocity of $v_{n,max}$.

4.2.2.1 Forwarding rule

During different traffic light phases, drivers have different driving behavior so the forwarding rules in the CA model are also different. Therefore, we will introduce the forwarding rules with two parts as follows.

4.2.2.1.1 Green-light phase

There are four consecutive steps in the forwarding rules during the green-light phase, which are performed in parallel for all vehicles.

S1: Safe distance. Obtain three safe distances for vehicle n, including safe acceleration distance d_{acc_n}, safe keep velocity distance d_{keep_n} and safe deceleration distance d_{dec_n}.

For the normal vehicle-vehicle cases, where vehicle $n+1$ is followed by vehicle n, d_{acc_n}, d_{keep_n} and d_{dec_n} are obtained with the following equations:

$$d_{acc_n} = max\left(0, \sum_{i=0}^{(v_n(t)+a)_{div\,M_n}} [(v_n(t)+a) - iM_n] - \sum_{i=0}^{(v_{n+1}(t)-M_{n+1})_{div\,M_{n+1}}} [(v_{n+1}(t) - M_{n+1}) - iM_{n+1}]\right) \tag{4.1}$$

$$d_{keep_n} = max\left(0, \sum_{i=0}^{v_n(t)_{div\,M_n}} [v_n(t) - iM_n] - \sum_{i=0}^{(v_{n+1}(t)-M_{n+1})_{div\,M_{n+1}}} [(v_{n+1}(t) - M_{n+1}) - iM_{n+1}]\right) \tag{4.2}$$

$$d_{dec_n} = max\left(0, \sum_{i=0}^{(v_n(t)-d)_{div\,M_n}} [(v_n(t)-d) - iM_n] - \sum_{i=0}^{(v_{n+1}(t)-M_{n+1})_{div\,M_{n+1}}} [(v_{n+1}(t) - M_{n+1}) - iM_{n+1}]\right) \tag{4.3}$$

For special car-truck cases, when both the velocity $v_n(t)$ and limited deceleration capability M_n of vehicle n (car) are higher than $v_{n+1}(t)$ and M_{n+1} of the leading vehicle $n+1$ (truck), d_{acc_n}, d_{keep_n} and d_{dec_n} are calculated with the following equations:

For d_{acc_n}, we set $\Delta v = v_{n+1}(t) - M_{n+1} - (v_n(t)+a)$, $\Delta M = M_{n+1} - M_n$, $\tau_1 = \Delta v_{div\,\Delta M}$, $\tau_2 = (v_n(t)+a)_{div\,M_n}$.

$$d_{acc_n} = min\left\{\sum_{i=0}^{\tau_1\ or\ \tau_2} \left[\left((v_n(t)+a) - iM_n\right) - \left((v_{n+1}(t) - M_{n+1}) - iM_{n+1}\right)\right]\right\} \tag{4.4}$$

For d_{keep_n}, we set $\Delta v = v_{n+1}(t) - M_{n+1} - v_n(t)$, $\Delta M = M_{n+1} - M_n$, $\tau_1 = \Delta v_{div\,\Delta M}$, $\tau_2 = v_n(t)_{div\,M_n}$.

$$d_{keep_n} = min\left\{\sum_{i=0}^{\tau_1\ or\ \tau_2} \left[(v_n(t) - iM_n) - \left((v_{n+1}(t) - M_{n+1}) - iM_{n+1}\right)\right]\right\} \tag{4.5}$$

For d_{dec_n}, we set $\Delta v = v_{n+1}(t) - M_{n+1} - (v_n(t)-d)$, $\Delta M = M_{n+1} - M_n$, $\tau_1 = \Delta v_{div\,\Delta M}$, $\tau_2 =$

$(v_n(t) - d)_{div\, M_n}$.

$$d_{dec_n} = min\left\{ \sum_{i=0}^{\tau_1\, or\, \tau_2} \left[\left((v_n(t) - d) - iM_n\right) - \left((v_{n+1}(t) - M_{n+1}) - iM_{n+1}\right)\right] \right\} \tag{4.6}$$

For vehicle-obstacle cases, where vehicle n is the nearest vehicle behind an obstacle, d_{acc_n}, d_{keep_n} and d_{dec_n} are calculated with the following equations:

$$d_{acc_n} = max\left(0, \sum_{i=0}^{(v_n(t)+a)_{div\, M_n}} [(v_n(t) + a) - iM_n]\right) \tag{4.7}$$

$$d_{keep_n} = max\left(0, \sum_{i=0}^{v_n(t)_{div\, M_n}} [v_n(t) - iM_n]\right) \tag{4.8}$$

$$d_{dec_n} = max\left(0, \sum_{i=0}^{(v_n(t)-d)_{div\, M_n}} [(v_n(t) - d) - iM_n]\right) \tag{4.9}$$

S2: Slow to accelerate. Determine the stochastic noise parameter R_a based on the vehicle's velocity $v_n(t)$.

$$R_a = min(R_d, R_0 + v_n(t) \cdot (R_d - R_0)/v_s) \tag{4.10}$$

S3: Update the velocities of all vehicles simultaneously by comparing the vehicle's space gap $d_n(t)$ with the calculated three safe distances. When vehicles approach the merging area, they need to decelerate to the reduced speed limit v_r gradually in a short time period and obey the speed limit until moving out of the blocked area. At the same time, in the merging area, vehicles in the blocked lane (lane 1) will try to change to the unblocked lane (lane 2) as soon as possible. Therefore, the forwarding rules in the merging and blocked areas are different from those in the normal area.

S3a: Acceleration.

In the normal area, where the maximum velocity is v_{max}, if $d_n(t) \geq d_{acc_n}$, or in the merging and blocked areas, where the maximum velocity is v_r, if $d_n(t) \geq d_{acc_n}$ and $v_n(t) \leq v_r$

$$v_n(t+1) = \begin{cases} min(v_n(t) + a, v_{max} \; or \; v_r), if \; randf() \leq (R_a) \\ v_n(t), otherwise \end{cases} \tag{4.11}$$

S3b: Random slowing down.

In the normal area, if $d_{acc_n} > d_n(t) \geq d_{keep_n}$, or in the merging and blocked areas, if $d_{acc_n} > d_n(t) \geq d_{keep_n}$ and $v_n(t) \leq v_{wz}$

$$v_n(t+1) = \begin{cases} max(v_n(t) - d, 0), if \; randf() \leq (R_s) \\ v_n(t), otherwise \end{cases} \tag{4.12}$$

S3c: Braking.

In the normal area, if $d_{keep_n} > d_n(t) \geq d_{dec_n}$,

$$v_n(t+1) \rightarrow max(v_n(t) - d, 0) \tag{4.13}$$

In the merging and blocked areas,

$$v_n(t+1) = \begin{cases} max(v_n(t) - d, 0), if \; v_n(t) \leq v_r \; and \; d_{keep_n} > d_n(t) \geq d_{dec_n} \\ max(v_n(t) - d, 0), if \; v_n(t) > v_r \; and \; d_n(t) \geq d_{dec_n} \\ v_n(t), otherwise \end{cases} \tag{4.14}$$

S3d: Emergency braking. If $v_n(t) > 0$ and $d_n(t) < d_{dec_n}$,

$$v_n(t+1) \rightarrow max(v_n(t) - M_n, 0) \tag{4.15}$$

S4: Vehicle movement.

$$x_n(t+1) \rightarrow x_n(t) + v_n(t+1) \tag{4.16}$$

where $x_n(t)$ and $v_n(t)$ denote the longitudinal position and velocity of vehicle n at time step t, respectively; $d_n(t)$ denotes the space gap of vehicle n, which is the clear distance between vehicle n and its preceding vehicle $n+1$ on the current lane, $d_n(t) = x_{n+1} - x_n - l_n$; if vehicle n is the first vehicle on its lane, a large value will be assigned to $d_n(t)$; l_n denotes the length of vehicle n; a and d denote the normal acceleration and deceleration rate, respectively; $X_{div\,Y}$ denotes the integer division, and it is defined as $X_{div\,Y} = [X/Y]$, where "/" denotes normal division and $[z]$ is the floor function; v_s is a constant velocity slightly above 0; R_0 and R_d are given constants that control the velocity fluctuations of vehicles, $0 < R_0 < R_d \leq 1$; $R_a = R_0$ when the $v_n(t) = 0$, and $R_a = R_d$ when $v_n(t) \geq v_s$; R_s is the slowing down probability.

4.2.2.1.2 Yellow- and red-light phases

Once the yellow light is on, drivers must decide to stop or to cross the intersection. Therefore, at the onset of yellow light, the status of a vehicle needs to be determined based on the vehicle's distance to the intersection and the driving speed. There are three possible statuses for each vehicle, namely "cross status", "stop status" and "follow status". A vehicle with a cross status will cross the intersection during the yellow-light phase. With a stop status, the vehicle will stop in front of the intersection during the yellow and red-light phases. There is only one vehicle with a stop status on each lane. All the vehicles behind any vehicle in "stop status" are in "follow status", which will move by following their preceding vehicles. A vehicle's status will be determined by three algorithms in the proposed CA model. The first algorithm is used to reflect the uncertainty of a driver's decision with a distance-dependent stopping probability function. A logistic function adopted by Hsu and Chiou (2018) is used to compute the probability of stop decision of a vehicle at the onset of yellow light, as expressed in Eq. (4.17). The logistic function describes the relationship between the stopping probability of a vehicle and its distance to the intersection. Generally, as the distance to the intersection decreases, the stopping probability increases.

$$P_s = \frac{1}{1+e^{-\alpha(d_{sig}-\beta)}} \tag{4.17}$$

where P_s is the stopping probability of a vehicle; d_{sig} is the distance to the intersection; α and β are two shape parameters.

The second algorithm is that if a vehicle cannot stop in front of the intersection during the yellow-light phase by decelerating from its current speed with the maximum deceleration rate, it will have a "cross status". If not, the vehicle may have a "stop status". The stopping distance during the yellow-light phase can be expressed with Eqs. (4.18) and (4.19).

$$t_d = v_n(t)_{div\ M_n} \tag{4.18}$$

$$S_d = \begin{cases} \sum_{i=1}^{t_d} [v_n(t) - iM_n], if\ t_d \leq t_y \\ \sum_{i=1}^{t_y} [v_n(t) - iM_n], if\ t_d > t_y \end{cases} \tag{4.19}$$

The third algorithm is that if a vehicle driver decides to proceed through the intersection but cannot reach the intersection by accelerating with the normal deceleration rate, the vehicle will have a "stop status" when it reaches the intersection. The driving distance during the yellow-light phase can be calculated with Eqs. (4.20) and (4.21).

$$t_c = \left(v_{max} - v_n(t)\right)_{div\ a} \tag{4.20}$$

$$S_c = \begin{cases} \sum_{i=1}^{t_c} [v_n(t) - ia] + \left(t_y - t_c\right)v_{max}, if\ t_c \leq t_y \\ \sum_{i=1}^{t_y} [v_n(t) - ia], if\ t_c > t_y \end{cases} \tag{4.21}$$

We set the identifier of "stop status", "cross status" and "follow status" as $st = 2, 1, and\ 0$, respectively. The "stop status" and "cross status" will be firstly determined by the logic algorithm displayed in Fig. 4.2 by considering all three above-mentioned conditions. The algorithm will be checked for all vehicles from the first to the last one on each lane. As long as vehicles with "stop status" and "cross status" are identified, the statuses of the rest vehicles will be assigned accordingly.

```
if S_d ⩽ d_sig
    if rand() ⩾ P_s
        st(i) = 2
    else
        if S_c ⩽ d_sig
            st(i) = 2
        else
            st(i) = 1
        end
    end
else
    st(i) = 1
end
```

Figure 4.2 Logic algorithm for vehicle status determination

After vehicle statuses are all identified, vehicles with different statuses will move by following different forwarding rules. Forwarding rules used in the green-light phase will still apply to vehicles with a "cross status" and "follow status". However, those forwarding rules will need some revisions before applying to vehicles with "stop status". Firstly, three safe distances in step S1, including safe acceleration distance d_{acc_n}, safe keep velocity distance d_{keep_n} and safe deceleration distance d_{dec_n}, will be calculated with Eqs. (4.7) to (4.9), respectively. Secondly, in step S3, space gap $d_n(t)$ will be substituted with $d_{sig}(t)$.

4.2.2.2 Lane-changing rule

The symmetric lane-changing rules are adopted in this model with the incentive and safety criteria. Once the lane-changing rules are satisfied, a vehicle will perform lane-changing maneuver with a probability of R_c. Vehicles in different areas have different lane-changing behavior: vehicles in the blocked area cannot change lane; moreover, vehicles in the merging area will try to switch from lane 1 to lane 2, but are not allowed to switch lane from lane 2 to lane 1. Therefore, different lane-changing rules will be applied depending on which area any vehicle is currently at.

4.2.2.2.1 Normal area

The incentive criterion:

$$d_n < d_{acc_n} \text{ and } d_{n,other} \geq d_{acc_{n,other}} \tag{4.22}$$

The safety criterion:

$$d_{n,back} > d_{dec_{back,n}} \tag{4.23}$$

where $d_{n,other}$ denotes the gap between vehicle n and the nearest vehicle in front of it in the adjacent lane, i.e. the front vehicle; $d_{n,back}$ denotes the gap between vehicle n and the nearest vehicle behind it in the adjacent lane, i.e. the back vehicle; $d_{acc_{n,other}}$ denotes the safe acceleration distance of vehicle n if it switches to the adjacent lane; $d_{dec_{back,n}}$ denotes the safe deceleration distance of the back vehicle if vehicle n is switched to the adjacent lane.

4.2.2.2.2 Merging area

Because vehicles in the merging area will try hard to switch from lane 1 to lane 2, the incentive criterion of lane change for them becomes less strict than that of vehicles in the normal area. Therefore, the incentive criterion is modified as follows.

$$d_{n,other} \geq d_{dec_{n,other}} \tag{4.24}$$

where $d_{dec_{n,other}}$ denotes the safe deceleration distance of vehicle n if it switches to the adjacent lane. The safety criterion of lane change is same as that in the normal area. Besides, vehicles in lane 2 will not change lane in the advance warning area, and therefore the lane-changing probability is set as R_c = 0.

4.3 Model calibration and validation

4.3.1 Data collection

The data used in this study was collected from Drake Road between Shields Street and Taft Hill Road, a two-lane arterial road in the City of Fort Collins, Colorado. There are two reasons why this road was chosen. Firstly, there was a work zone area on one of the two lanes on this road, which can be treated as a typical PBR scenario. Secondly, there was a data collection system Bluetoad installed on both ends of the road. The total length of the road is 1,610 m with the speed limit of 18 m/s (40 mph). The work zone was located from 644 to 1,079 m, with a length of 435 m. There was a warning sign located at 300 m upstream of the work zone and there was no posted work zone speed limit. The durations of green-, yellow- and red-light phases were 25 s, 5 s, and 60 s, respectively. The data used in this study was collected between December 9th and December 23th of 2018 when the work zone was under construction. Two types of traffic data were collected: microscopic and macroscopic data. Macroscopic data include travel time, speed, and vehicle volume, which are accessible from the data collection system BlueTOAD installed on both ends of the road section. The system measures travel time and delay of travelers by detecting Bluetooth MAC addresses of passing devices (e.g. mobile phones, ear phones and in-vehicle hand free audio systems) and comparing the time of these addresses from one known location to another. Macroscopic data were collected for 15 days and the datasets were aggregated over 15-minute time intervals. According to the field observation, the truck ratio is about 5%.

For the microscopic data collection, the video-photographic method is the most widely used technique. However, the method is not suitable in this study because many cameras are needed to cover long road sections and the accuracy is not guaranteed with fewer cameras. Therefore, a smartphone-based GPS method is used to collect the microscopic data of moving vehicles in this study. The instantaneous vehicle speed and trajectory were measured through a mobile app called GPS Speedometer installed on the drivers' smartphone and the mobile app has an accuracy of 98%. Vehicles moved in tandem along the road in order to consider the interaction between vehicles. The limitation of this method is that data collection is restricted by the available resources, such as drivers, vehicles and smartphones. In this study, during each round of data collection, two experienced test drivers were asked to drive through the whole road section from the beginning to the end, and the trajectory and speed data were collected with the mobile app. A total of 12 rounds of data collection were conducted.

4.3.2 Model calibration

The proposed model is then calibrated with the collected data macroscopically and microscopically. Because microscopic data of trucks are not available, microscopic calibration is conducted for cars only. Parameters of trucks, such as vehicle length l, acceleration rate a, vehicle deceleration rate d, and deceleration capability M provided in Li et al. (2016) are used, as shown in Table 4.1. Moreover, it is observed that maximum velocities for cars and trucks outside the work zone area are about 18 m/s (40 mph) and 15.5 m/s (35 mph), respectively. The observed maximum velocity in the work zone area for both vehicle types is about 13.5 m/s (30 mph). Preliminary tests show that some model parameters have more significant influence on the vehicle trajectory and speed than the rest, while others have greater influence on the macroscopic dynamics of traffic flow. Therefore, calibrations are performed in two steps. Firstly, trajectory and speed data are used to calibrate parameters of cars including the vehicle acceleration rate a, vehicle deceleration rate d, and deceleration capability M. Secondly, aggregated average travel speed data are used to calibrate model parameters including the randomization probability R_s, the stopping probability-related parameter α and β, and the stochastic noise-related parameter v_s. Genetic Algorithm is used in the macroscopic and microscopic calibration, and the calibrated parameter values for the proposed model are found and displayed in Table 4.1.

Table 4.1 Calibrated parameters for the proposed model

Parameters	Car	Truck
Vehicle length l (m)	6	12
Acceleration a (m/s^2)	1	0.5
Deceleration d (m/s^2)	1.5	1
Deceleration capability M (m/s^2)	4	3
Maximum velocity v_{max} (m/s)	18	15.5
Work zone speed limit v_r (m/s)	13.5	
Stochastic noise related parameter v_s (m/s)	5.5	
Randomization probability R_s	0.36	
Stopping probability related parameter α	0.17	
Stopping probability related parameter β (m)	55.5	

4.3.3 Model validation

The validation of the proposed model is conducted at microscopic and macroscopic levels. In microscopic validation, we compared the trajectory and speed of individual vehicles generated from the proposed model with the measured field data. In macroscopic validation, the simulated average travel speeds were compared with the measured field data.

4.3.3.1 <u>Microscopic validation</u>

The simulated trajectories by the proposed model are compared with the measured microscopic filed data. In order to generate the same initial headway, observed vehicle arrival distribution and entry speed are used to generate vehicles in the simulation. Fig. 4.3 shows the comparison of the observed and simulated longitudinal trajectories and speeds for two cars. It can be seen from the figure that both cars decelerate from the maximum velocity before entering the work zone, accelerate after leaving the work zone, and finally stop in front of the red traffic light. There is good agreement between the simulated trajectory and speed and the field data for both cars. However, relatively large speed deviations are found in the work zone area (Fig. 4.3b), especially for car 2, due to the stochastic characteristic of traffic dynamics. This indicates that microscopic traffic dynamic is not only affected by the vehicle performance, but also the driving behaviors of different drivers, especially in abnormal driving environments such as disrupted roadways. Moreover, some obvious trajectory deviations are found for car 2 when it approached the traffic light (Fig. 4.3a), which was mainly resulted from the speed deviations in the work zone area.

Error tests are used to quantitatively evaluate the performance of the proposed model. The overall error between the simulation results and field data are quantified by the root mean square percent error (RMSE) and mean percent error (MPE). The equation of RMSE and MPE can be expressed as follows.

$$RMSE = \sqrt{\frac{1}{N}\sum_{k=1}^{N}\left(\frac{\hat{z}_k - z_k}{z_k}\right)^2} \tag{4.25}$$

$$MPE = \frac{1}{N}\sum_{k=1}^{N}\left(\frac{|\hat{z}_k - z_k|}{z_k}\right) \tag{4.26}$$

where $\hat{z}_k$ is the simulated value from the proposed model, z_k is the corresponding observed value from the field data, and N is the number of observations. Error tests are performed for the trajectories and speeds of each vehicle at each second. According to the error tests result, the RMSE and MPE of the vehicle trajectories are less than 7% and 4%, respectively. The RMSE and MPE of vehicle speeds are less than 7% and 6%, respectively. The deviations between the simulation and field data are relatively small and deemed acceptable. Therefore, we can conclude that the proposed model can capture the traffic dynamics of disrupted flow at the microscopic level with reasonable accuracy.

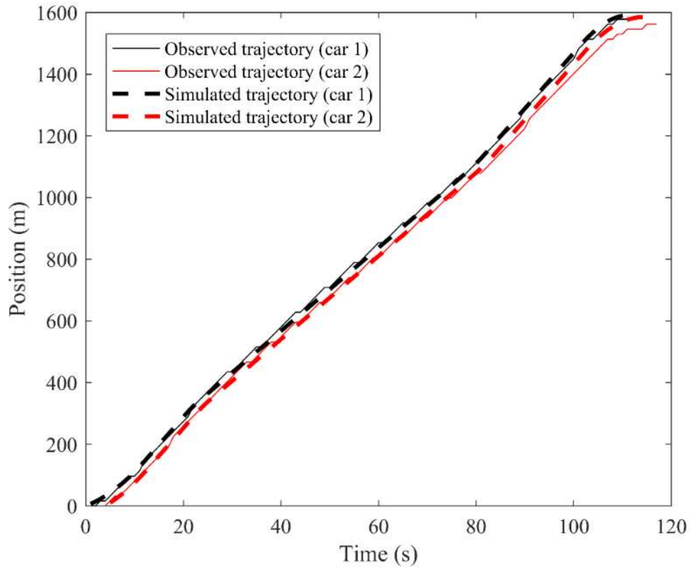

(a) Position

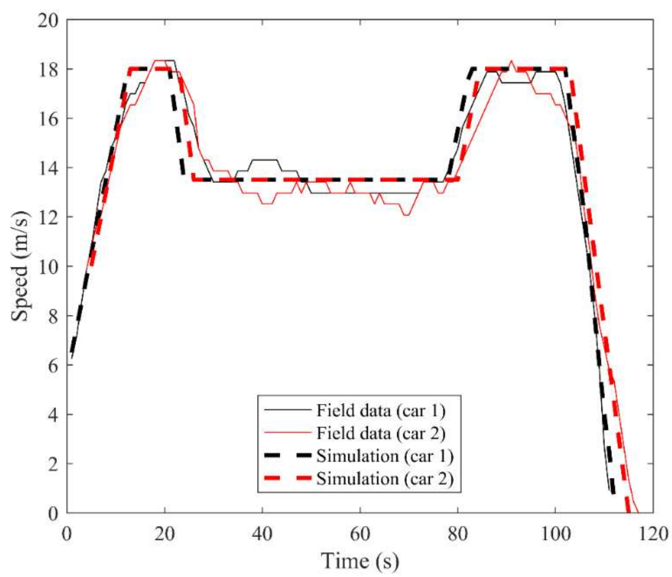

(b) Speed

Figure 4.3 Comparison between observation and CA simulation

4.3.3.2 Macroscopic validation

The model is then validated with average travel speed data from the rest 5 days of the 15 days. Firstly, the speed-volume relationship from the simulation results was compared with the field data. Fig. 4.4 shows the comparison of speed-volume relationships from both field data and simulation. It can be seen from the figure that the simulated speed-volume relationship has a good agreement with the observed field data, although there is pretty large discrepancy against the field data under low-volume traffic conditions. Secondly, we compared the simulated time series of speed with field data in order to evaluate how well the proposed model performs in the time domain. Fig. 4.5 shows the comparison of time series of speed from field data and simulation. It can be seen that the simulated speeds match well with the field data for most time periods except for the late night and early morning when the traffic volume is very low, and the travel time becomes significantly random. RMSE and MPE are still used for the overall error of the aggregated speed between simulation results and field data, which are found to be 12% and 9%, respectively. These errors are within the acceptable limit as stated by Meng and Weng (2011) for the CA-based model in terms of travel speed. These results show that the proposed model can realistically reproduce the disrupted traffic flow at the macroscopic level.

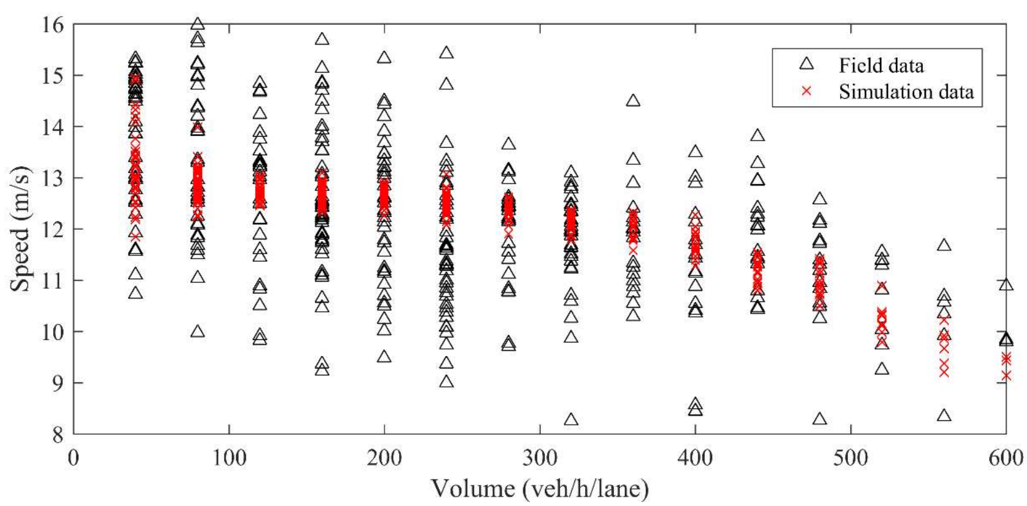

Figure 4.4 Comparison of speed-volume relationship from field data and simulation

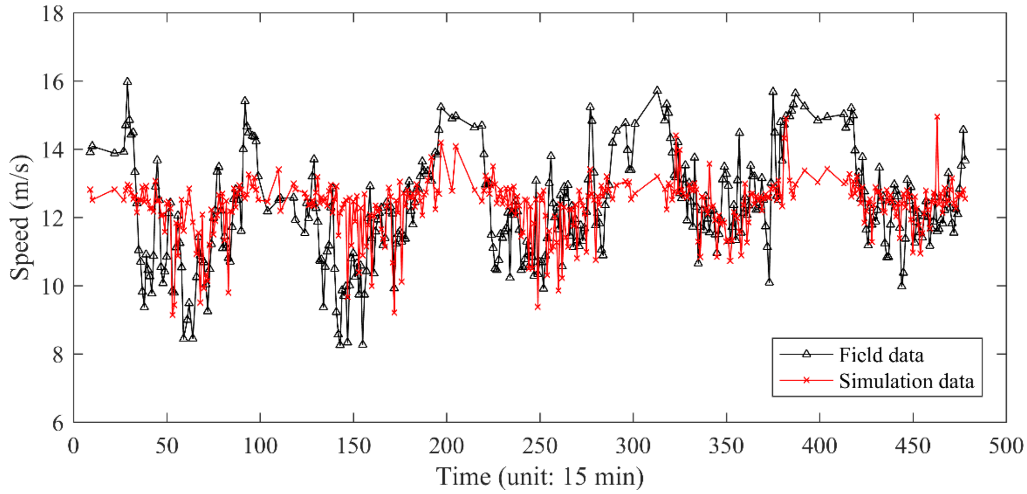

Figure 4.5 Comparison of time series of speed from field data and simulation

4.4 Development of travel time functions for PBR

4.4.1 Simulation experiments

Traffic volume, truck ratio and blockage ratio are identified as the three key factors that affect travel time in past studies. Blockage ratio is defined in this study as the ratio between the length of the blockage and the total length of the road. In order to evaluate quantitatively the influence of traffic volume, truck ratio and blockage ratio on travel time, microscopic simulation experiments are conducted with the validated model on the same disrupted road in the last section. A total of 525 combination scenarios for 15 traffic volumes (50 to 750 veh/h/lane with a 50 veh/h/lane increment), 7 truck ratios (0% to 30% with a 5% increment) and 5 blockage ratios (10% to 50% with a 10% increment) are simulated.

Fig. 4.6 shows the simulated travel time-volume data with different truck ratios when the blockage ratio R_b equals 30%. Fig. 4.7 shows the simulated travel time-volume data with different blockage ratios when the truck ratio R_t equals 20%. Several general observations can be made from the simulation results in Figs. 4.6 and 4.7. Firstly, the travel time increases as the traffic volume increases. Secondly, it is found in Fig. 4.6 that the travel time increases as the truck ratio increases and the impact of the truck ratio becomes more significant when the traffic volume is higher. Thirdly, it can be found in Fig. 4.7 that the travel time increases with the increase of the blockage ratio. However, as the traffic volume increases, the influence of the blockage ratio becomes slightly less significant.

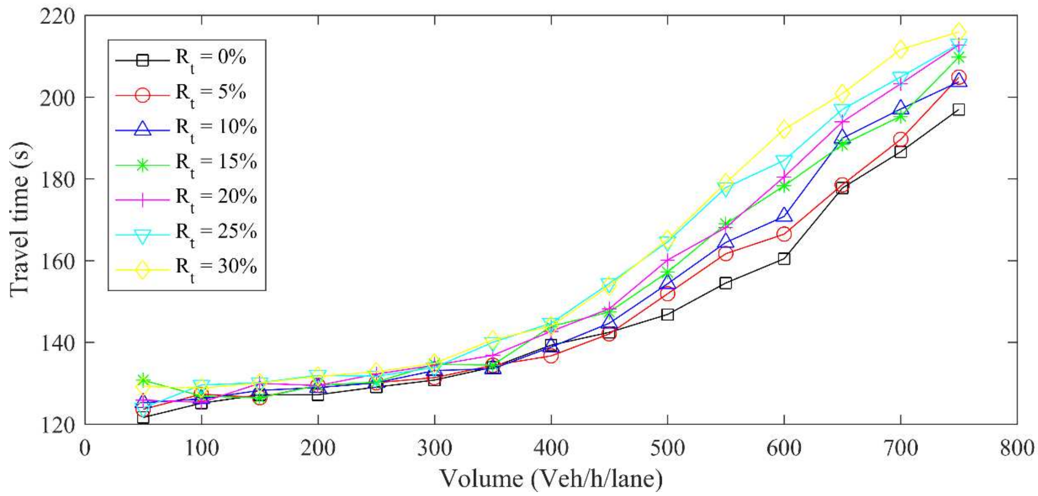

Figure 4.6 Simulated travel time-volume data with different truck ratios

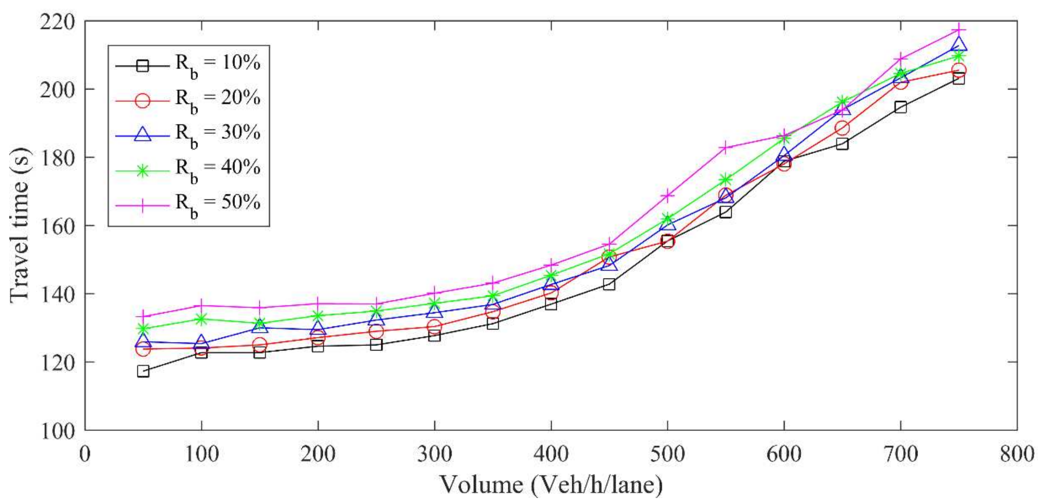

Figure 4.7 Simulated travel time-volume data with different blockage ratios

4.4.2 Regression analysis of travel time functions

In order to consider the effect of trucks on the travel time-volume relationship, Yun et al. (2005)

proposed a revised BPR function, which has the following form.

$$t = t_0\left[1 + \alpha(1 + R_t)^{\beta}(f/C)^{\gamma}\right] \tag{4.27}$$

where t is the travel time; t_0 is the free-flow time; f is the traffic flow volume; C is the road capacity; α, β and γ are coefficients. The term $(1 + R_t)^{\beta}$ in Eq. (4.27) is used to reflect the impact of the truck ratio on the travel time in a reasonable way. Firstly, the value of this term becomes 1 when the truck ratio $R_t = 0$. This ensures that Eq. (4.27) is consistent with the BPR function. Secondly, the value of $(1 + R_t)^{\beta}$ increases as the truck ratio R_t increases when $\beta > 0$.

As discussed earlier, the blockage ratio R_b has following effects on travel time: a significant increase in the free-flow time as R_b increases, and a smaller influence when the traffic volume is higher. Therefore, two modifications of Eq. (4.27) need to be made to consider the effect of the blockage ratio. Firstly, a new term $f(R_b)$, which is a function of the blockage ratio R_b, is introduced to replace the constant free-flow time t_0. This ensures that different blockage ratios correspond to different free-flow time. Several possible function forms (e.g. linear, quadratic, exponential functions) are tested, and it is found that a simple linear function can provide a very good fit of the observed data. Secondly, a power function in the form of $(1 + R_b)^{\beta}$ is introduced to consider the decreasing effect of the blockage ratio with the increase of traffic volume. When $\beta < 0$, the value of $(1 + R_b)^{\beta}$ decreases as the blockage ratio R_b increases. The other reason that we choose the power function is that it has a consistent form as the term about the truck ratio R_t, which allows for easy calibration. Finally, the modified travel time function has the following form:

$$t = (\alpha_1 + \alpha_2 R_b)[1 + \alpha_3(1 + R_b)^{\alpha_4}(1 + R_t)^{\alpha_5}(f/C)^{\alpha_6}] \tag{4.28}$$

where α_1, α_2, α_3, α_4, α_5, and α_6 are parameters.

A nonlinear regression analysis is performed to estimate the parameters of the travel time function shown in Eq. (4.28) with the simulated 525 data sets. The road capacity used in the analysis is determined based on the speed-volume relationship from the field data, which is around 600 vehicle/h/lane. The calibrated travel time functions are shown as follows.

$$t = (115.8 + 30.4R_b)[1 + 0.357(1 + R_b)^{-0.304}(1 + R_t)^{1.36}(f/C)^{2.387}] \quad (4.29)$$

To measure how well the regression model describes the simulated data, a number of goodness-of-fit statistics are evaluated. The high value of R^2 (0.99) and low value of SEE (3.11) clearly indicates that the calibrated travel time functions can capture the relationship between the travel time and the traffic volume, truck ratio and blockage ratio very well. The high value of F (41815) also indicates overall significance of the regression model.

The calibrated travel time functions are further validated by predicting travel time of random traffic scenarios and comparing them against the actual values. A randomly selected scenario (R_b = 0.33 and R_t = 0.18) that was not included in the previous simulation is used in the validation analysis. The validation results are shown in Fig. 4.8, from which it can be seen that all new simulation data of the selected scenario falls in the 95% prediction intervals of the regression travel time. Similar validation results are also obtained for other random scenarios and this indicates that the calibrated travel time functions are able to predict new observations with acceptable accuracy.

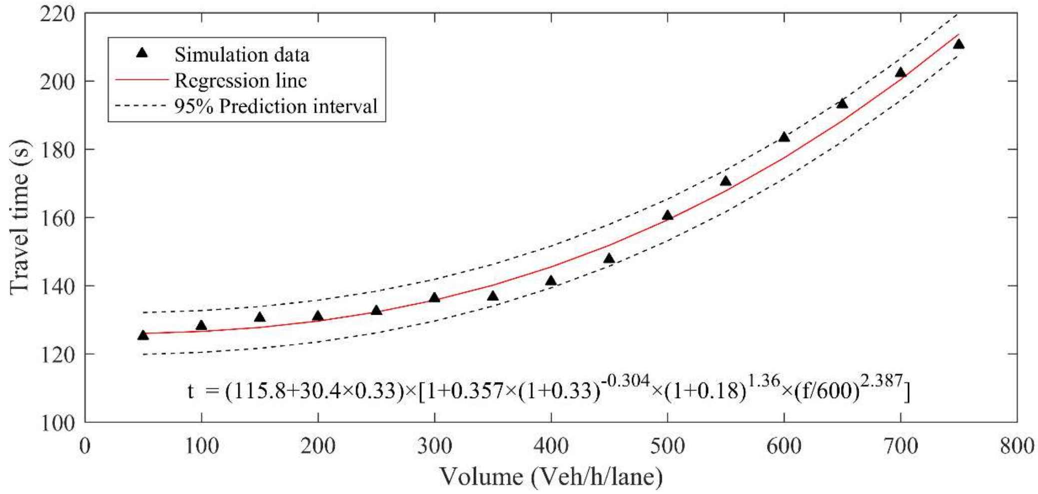

Figure 4.8 Validation results for a random selected scenario

4.4.3 Discussion on the application of travel time function for PBR

Accurate estimation of travel time on PBR is very important for the performance assessment of post-hazard transportation networks. However, the standard BPR function was usually used in the past for travel time prediction on PBR in the post-hazard transportation demand modeling, due to unavailability of travel time functions derived specifically for PBR. In this section, we will compare the developed travel time functions with the standard BPR function to identify the difference between them. The comparison of the calibrated travel time functions of different traffic scenarios and the standard BPR function for PBR is shown in Fig. 4.9. There are 6 different combination scenarios in Fig. 4.9, including 3 blockage ratios and 2 truck ratios. In line with previous practice, the free-flow time under normal condition (t_0 = 109 s) and the reduced traffic capacity (C = 600 Veh/h/lane) are substituted into the standard BPR function, $t = t_0(1 + 0.15(f/C)^4)$, to get the travel time function.

Several limitations of the standard BPR function can be identified from Fig. 4.9. Firstly, since there is only one curve for the standard BPR function, it cannot consider the difference between different traffic scenarios with different vehicle compositions and blockage sizes. Secondly, the curve of the standard BPR is considerably different from that of the calibrated functions. Although the values from both functions increase over volume-to-capacity ratio, the increment is much smaller under undersaturated condition for the standard BPR function, because the interaction between vehicles and the obstruction was not considered. Thirdly, the standard BPR function underestimates travel time under both undersaturated and oversaturated conditions as compared to the calibrated functions. For example, for the scenario where the blockage ratio R_b = 10% and truck ratio R_t = 10%, the estimated travel time by the standard BPR function is 25% lower when the volume-to-capacity ratio is 1.0. Underestimation of travel time with the standard BPR function will lead to biased travel demand estimates. Apparently, the calibrated travel time functions can give more realistic travel time prediction over the standard BPR function, which in turn leads to realistic travel demand estimate in post-hazard transportation network analysis.

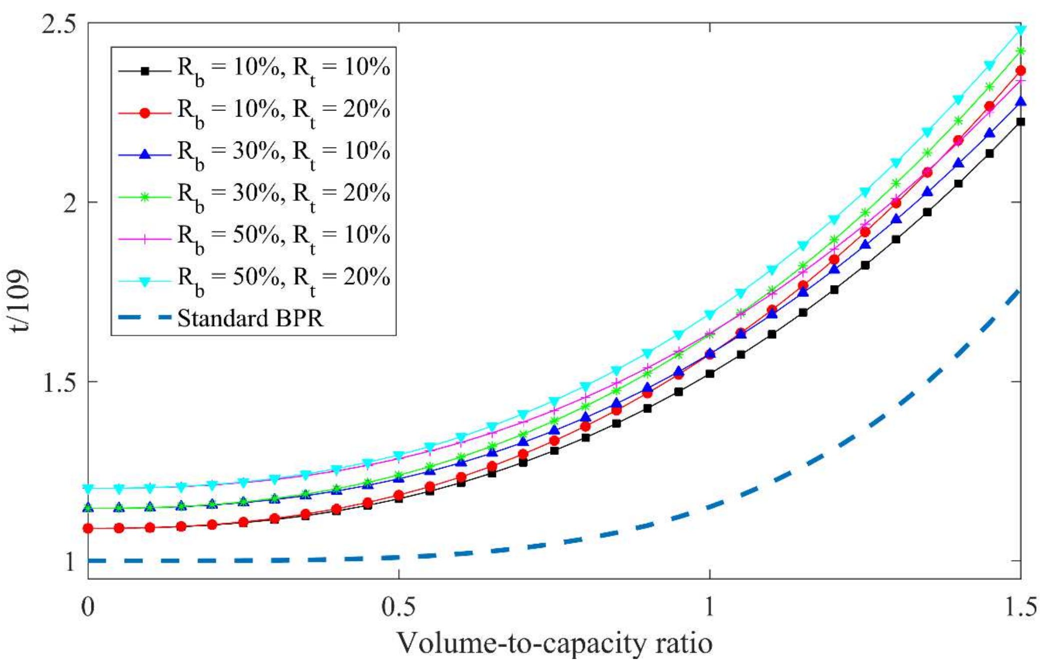

Figure 4.9 Comparison of calibrated travel time functions and standard BPR function

4.5 Conclusions

By overcoming the limitations of previous studies, this study proposed a methodology for developing travel time functions of PBR in urban areas based on microscopic traffic simulation. Firstly, an improved CA model was proposed for heterogeneous traffic flow on partially blocked arterial roads by extending the two-lane SD model. With the proposed model, two types of unrealistic deceleration behaviors in most existing CA models can be avoided. Meanwhile, driver's behaviors during traffic signal change intervals were realistically replicated by determining the vehicle status based on the vehicle's distance to the intersection, driving speed and stopping probability. Secondly, the proposed model was calibrated and validated with the collected field traffic data in both macroscopic and microscopic scales. The validation results show that the proposed model can simulate the disrupted traffic flow with acceptable accuracy. Finally, the traffic data under various scenarios with different traffic volumes, truck ratios and blockage ratio were generated through microscopic simulation experiments. The experiment results demonstrate that both blockage ratio and truck ratio have significant influence on the travel time. A continuous traffic time function was proposed for the disrupted traffic flow to capture the effect of the blockage ratio and truck ratio on the travel time. Its parameters were then estimated through a nonlinear regression analysis with the generated traffic data. Comparison results show that the developed travel time functions can provide more flexible and accurate predictions of travel time for PBR than the standard BPR function.

CHAPTER 5 FRAMEWORK OF SIMULATION-BASED VEHICLE SAFETY PERFORMANCE ASSESSMENT OF HIGHWAY SYSTEM UNDER HAZARDOUS DRIVING CONDITIONS[4]

5.1 Introduction

Vehicles are extremely vulnerable to single-vehicle accidents under some hazardous driving conditions (i.e. strong wind, icy or snowy road surface). An integrated framework is proposed to assess single-vehicle traffic safety performance of stochastic traffic flow under hazardous driving conditions. Different from most existing studies focusing on a single vehicle moving at a constant speed, for the first time, the proposed work evaluates individual vehicle safety performance based on the time-dependent simulation results of stochastic traffic flow, including instantaneous speeds and positions of each vehicle as a part of simulated traffic flow. Simultaneously, complex geometric and other environmental conditions of the highway system are also considered realistically, not only during the safety assessment process, but also in quantifying the wind loads applied on the vehicles. Finally, with the safety information of each individual vehicle, an overall safety performance index of the whole traffic flow on the highway system is further introduced, which serves as a potential traffic safety performance measure and resilience indicator of transportation infrastructure systems under various hazardous conditions. This study has potential applications to not only regular vehicles, but also advanced traffic management and control algorithms for connected and autonomous vehicles in hazardous driving environments.

5.2 Methodology Formulation

[4] This chapter is adapted from a published paper by the author (Hou, Chen and Chen 2019) with permission from Elsevier.

As illustrated in Fig. 5.1, the proposed vehicle safety assessment framework consists of three main parts: first, stochastic traffic flow is simulated with an improved CA-based traffic flow simulation model; second, rollover or sideslip accidents of each individual vehicle in the simulated traffic flow under hazardous driving conditions are assessed with the single-vehicle accident (SVA) simulation model; finally, the overall traffic safety performance of the traffic flow is assessed in terms of accident vulnerability for a specific hazardous scenario. The sketch of the first two parts in the proposed framework is shown in Fig. 5.2. The theoretical basis of these three parts is introduced in Section 5.2.1 to 5.2.3. In Section 5.2.1, an improved traffic flow simulation model is introduced. Section 5.2.2 presents a single-vehicle accident simulation model and describes in detail the external loads acting on vehicles. The vehicle safety assessment method of traffic flow is introduced in Section 5.2.3.

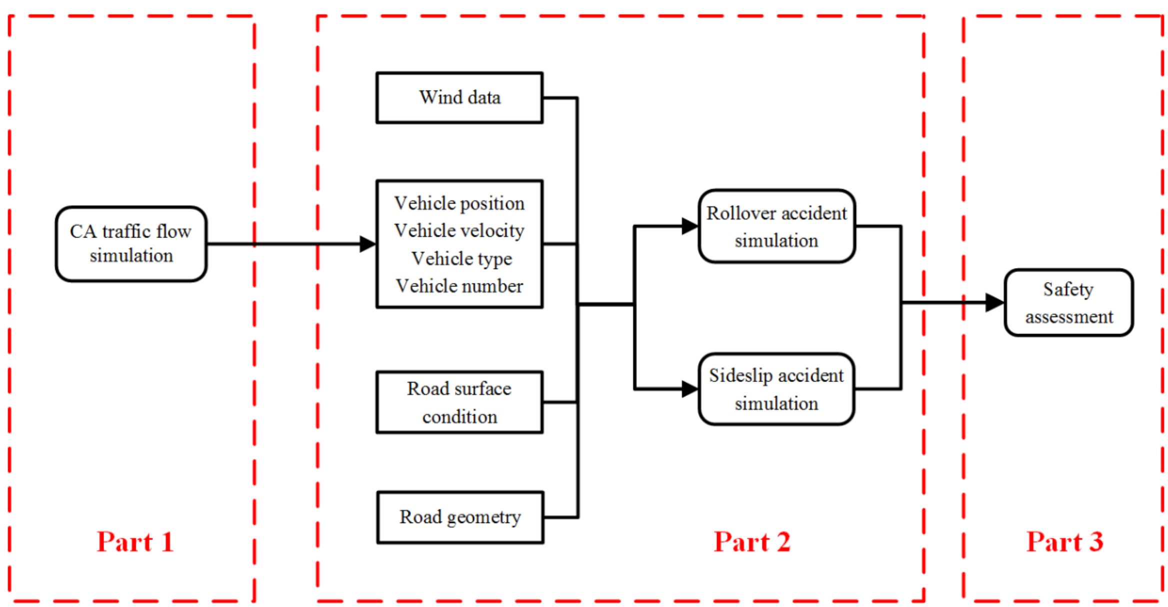

Figure 5.1 Flowchart of the traffic safety assessment framework

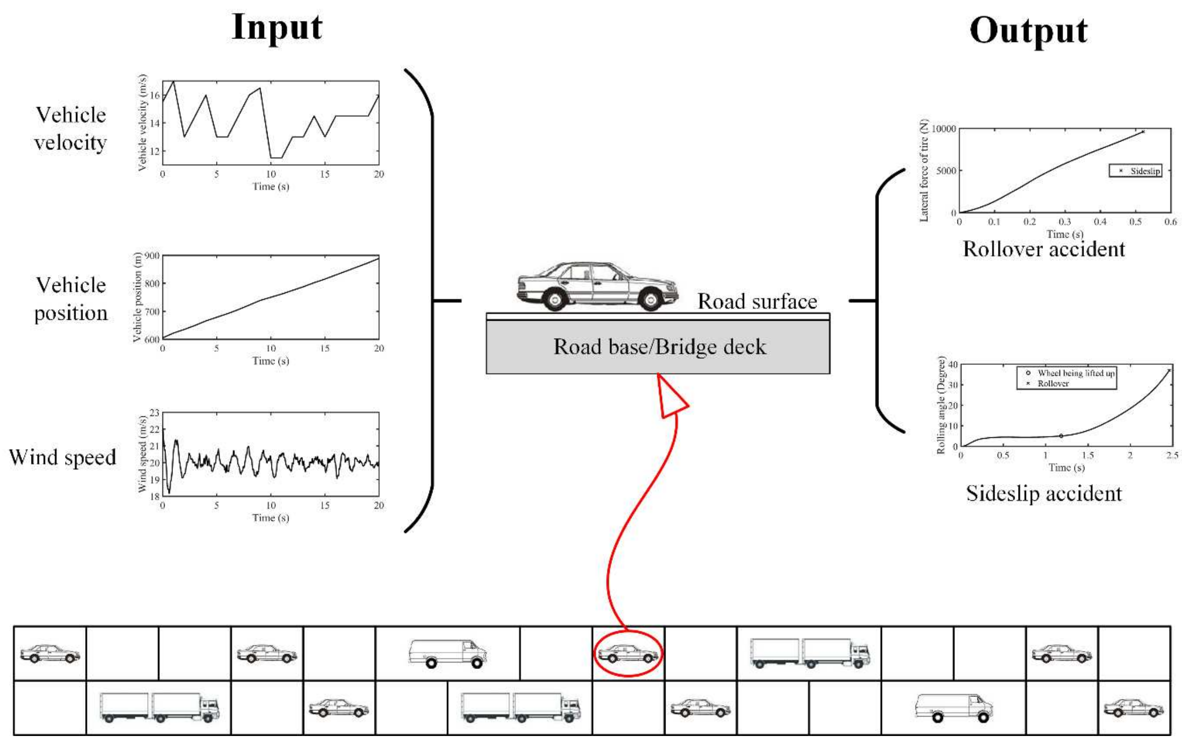

Figure 5.2 Sketch of the traffic safety assessment framework

5.2.1 Traffic flow simulation with improved CA model

As a stochastic microscopic traffic flow simulation model, the cellular automaton (CA) model is able to simulate the traffic flow realistically in a microscopic scale. In this study, an improved CA model for hazardous driving conditions is applied to provide the time-variant information (i.e. vehicle position, vehicle velocity, and vehicle type) of individual vehicles of the traffic flow in a highway system (Hou et al. 2017). At each time step, the velocity and position of each vehicle are updated through the single-lane forwarding rule (i.e. acceleration, deceleration, random brake, and movement) and the lane-changing rule. Based on the basic CA model, limited deceleration capabilities and realistic vehicle properties are incorporated into the proposed model in order to simulate more realistic traffic flow under hazardous conditions. A refined cell length (0.5 m) is used to represent multiple types of vehicles (i.e. car, van, and truck) with different dimensions in the mixed traffic flow. More details about the improved model can be found in Refs (Hou et al. 2017; Chen and Wu 2011).

5.2.2 Single-vehicle accident (SVA) simulation model for individual vehicles

The simulation-based SVA model proposed by Chen and Chen (2010, 2011) is employed to simulate the accidents of vehicles in the traffic flow under hazardous driving conditions. In order to provide some essential background information, the simulation model is briefly introduced below (Chen and Chen 2010).

5.2.2.1 Vehicle dynamics model

A vehicle is modelled with three rigid bodies, one representing the sprung mass and the other two for the unsprung masses of the front and rear axles. The sprung mass rotates about the roll axis, in the manner representing the kinematic properties of the front and rear suspensions. The unsprung masses can also rotate to consider the effect of the vertical compliance of the tires. Five differential equations of motion are built to describe the balance of the lateral force and the yaw moment of the entire vehicle, and the roll motion of the sprung and unsprung masses. The detailed equations of motion and related parameters can be found in the study by Chen and Chen (2010). Dynamic equations will be solved by the Runge-Kutta method in time domain with a time step of 0.001 s.

5.2.2.2 External loads acting on vehicles

5.2.2.2.1 Wind loads

Sudden crosswind gust is common in nature, especially in complex terrains where wind is significantly influenced by changes of surrounding environments. These include but are not limited to moving vehicles passing between open road segments and road segments with mountains, trees or bushes, passing bridge towers or other roadside structure that may temporarily shield the wind acting on the vehicles. In existing studies regarding single-vehicle safety, sudden crosswind has been identified as a critical scenario for moving vehicles (Baker 1986; Guo and Xu 2006; Wang and Xu 2015).

The wind forces and moments acting on a moving vehicle are determined by the quasi-static assumption (Baker 1987, 1994; Coleman and Baker 1994), which are defined in Eqs. (5.1) – (5.6).

$$F_x = \frac{1}{2}\rho C_{Fx} U_{re}^2 A \tag{5.1}$$

$$F_y = \frac{1}{2}\rho C_{Fy} U_{re}^2 A \tag{5.2}$$

$$F_z = \frac{1}{2}\rho C_{Fz} U_{re}^2 A \tag{5.3}$$

$$M_x = \frac{1}{2}\rho C_{Mx} U_{re}^2 A h_{re} \tag{5.4}$$

$$M_y = \frac{1}{2}\rho C_{My} U_{re}^2 A h_{re} \tag{5.5}$$

$$M_z = \frac{1}{2}\rho C_{Mz} U_{re}^2 A h_{re} \tag{5.6}$$

where F_x, F_y, and F_z denote the drag force, lift force, and side force, respectively; M_x, M_y, and M_z denote the rolling moment, yawing moment, and pitching moment, respectively; C_{Fx}, C_{Fy}, C_{Fz}, C_{Mx}, C_{My}, and C_{Mz} are the coefficients of drag force, lift force, side force, rolling moment, yawing moment, and the pitching moment, respectively; ρ is the density of air; A is the reference area; h_{re} is the reference arm; U_{re} is the wind velocity relative to the vehicle (Fig. 5.3), which is defined in Eq. (5.7).

$$U_{re} = \sqrt{[U + u(t)]^2 + V^2(t) - 2V(t)[U + u(t)]cos\varphi} \tag{5.7}$$

where U is the mean wind velocity; $u(t)$ is the turbulent component of wind velocity in the alongwind direction; $V(t)$ is the driving speed of the vehicle; φ is the wind direction.

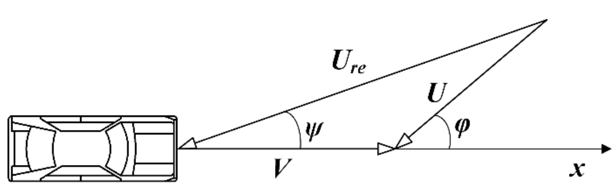

Figure 5.3 Demonstration of the relative wind velocity

It is assumed that wind is perpendicular to the vehicle driving direction all the time on straight road segments, whereas the angle between wind and the vehicle driving direction will change with the instantaneous position of the vehicle on curved roads (Fig. 5.4).

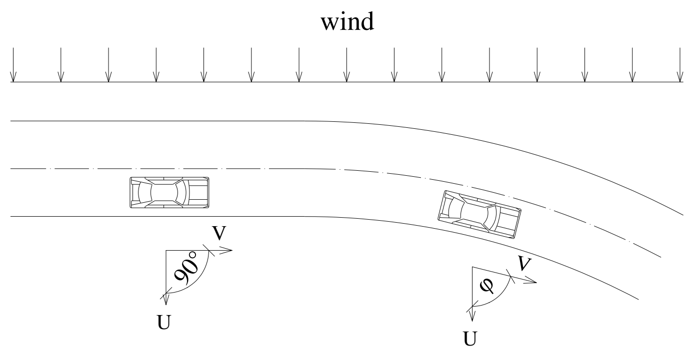

Figure 5.4 Sketch of a moving vehicle under crosswind condition

5.2.2.2.2 Tire forces

The lateral tire forces of the front and rear wheels acting at the wheel contact points with the ground are approximated to be proportional to their respective tire side slip angles, which are defined in Eqs. (5.8) and (5.9) (Gaspar et al. 2004; 2005).

$$F_{y,f} = \mu c_f \alpha_f \tag{5.8}$$

$$F_{y,r} = \mu c_r \alpha_r \tag{5.9}$$

where $F_{y,f}$ and $F_{y,r}$ denote the lateral tire forces of the front and rear tires, respectively; μ denotes the friction coefficient of the road surface; c_f and c_r are the tire cornering stiffness of the front and rear tires; α_f and α_r are the tire side slip angles of the front and rear tires, respectively.

The tire sideslip angle of the front and rear tires can be expressed by Eqs. (5.10) and (5.11) (Gaspar et al. 2004; 2005).

$$\alpha_f = -\beta + \delta - a_f \dot{\psi} V \tag{5.10}$$

$$\alpha_r = -\beta - a_r \dot{\psi} V \tag{5.11}$$

where β is the sideslip angle; δ is the steer angle; $\dot{\psi}$ is the yaw rate; V is the driving speed; a_f and a_r are the longitudinal distances from the center of sprung mass to the front and the rear axles, respectively.

5.2.2.2.3 Force due to superelevation

Superelevation is designed to offset some of the centripetal force developed as a vehicle moves on a curved roadway. In this model, lateral force and roll moment on the vehicle due to superelevation are included in the dynamic equations to replicate the realistic situation when the vehicle is driven along a curved road. The recommended value of superelevation corresponding to the curvature radius in the Green book (AASHTO 2004) is adopted in this study.

5.2.2.3 <u>Accident assessment criteria for individual vehicles</u>

Based on the SVA model, the whole process of rollover/sideslip accidents can be simulated following the corresponding safety criteria (Chen and Chen 2010). A rollover accident is defined in two steps: first, the wheel lift-up phenomenon is identified by satisfying either Eq. (5.12) or Eq. (5.13); subsequently, after the wheel is lifted up, the vehicle will roll over ultimately when Eq. (5.14) is satisfied.

$$W_{trans} > mg/2 - F_{w,z}/2 \tag{5.12}$$

$$\phi^i - \phi^i_{t,f} \geq \phi^{cri} \quad or \quad \phi^i - \phi^i_{t,r} \geq \phi^{cri} \tag{5.13}$$

$$\phi > arc\ sin\left(d/2\sqrt{d^2/4 + h_{cm}^2}\right) + \theta \tag{5.14}$$

where W_{trans} is the weight-transfer ratio between the left and right wheels; m is the total mass of the vehicle; g is the acceleration of gravity; $F_{w,z}$ is the vertical wind force; ϕ is the absolute roll angle of sprung mass; ϕ^{cri} is the maximum allowable relative roll-over angle due to the mechanical restraints; $\phi^i_{t,f}$ or $\phi^i_{t,r}$ is the absolute roll angle of front or rear unsprung mass; d is the wheel width of the vehicle;

h_{cm} is the height of the mass center of the vehicle, measured upward from the ground; θ is the road superelevation.

A sideslip accident is defined as the situation when the lateral forces of front tires or rear tires exceed the corresponding sideslip critical friction forces (Chen and Chen 2010). Therefore, the criterion of a sideslip accident is shown as follows.

$$F_{y,f} > F_{la,f}^{max} = \mu F_{z,f} \tag{5.15}$$

or

$$F_{y,r} > F_{la,r}^{max} = \mu F_{z,r} \tag{5.16}$$

where $F_{la,f}^{max}$ and $F_{la,r}^{max}$ are the sideslip critical friction forces of the front and rear wheels, respectively; $F_{z,f}$ and $F_{z,r}$ are the vertical reaction forces on the front and rear axles, respectively.

It is assumed the vehicles in the traffic flow may encounter a sudden crosswind gust, which could be one of the most dangerous scenarios in terms of single-vehicle accidents (Baker 1987; Guo and Xu 2006). In addition, depending on the specific hazard and weather conditions, other adverse driving conditions may also be present simultaneously, such as adverse road surface conditions or complex terrains. For example, vehicles moving on a curved road with an icy surface may also experience a sudden crosswind gust. Typically, a vehicle under these hazardous conditions may rollover or sideslip over a certain time period, which will be assessed against the "critical sustained time" (CST) (Chen and Chen 2010). CST is the minimum time period required to sustain the specific combination of the adverse environments and driving conditions to enable an accident to occur. In this study, an accident is defined as the situation when the CST of a vehicle is less than 0.66 s, which is the median reaction time as recommended in the Green book (AASHTO 2004). In other words, if the occurrence of a vehicle accident (either sideslip or rollover) is within 0.66 s after it enters the road with an adverse environment, an accident is deemed to occur. If the CST is greater than 0.66 s, the vehicle is deemed remaining safe, assuming the driver has sufficient time to take appropriate actions to prevent the occurrence of an accident. In this study, secondary accidents of a vehicle caused by the accident occurrence of an adjacent vehicle is not considered due to very low probability (e.g. a rollover vehicle hit an adjacent vehicle). The accident simulation is performed for each vehicle in the traffic flow independently and simultaneously before the overall safety risk of the traffic flow is assessed in the following.

5.2.3 Vehicle safety assessment of traffic flow

With the time-variant information of any individual vehicle from the traffic flow simulation, accident simulation of that vehicle is peformed with the SVA model as discussed above. The hazardous conditions being investigated in this study include: sudden crosswind gust, various road surface conditions (i.e. dry, snowy, and icy), and complicated topographical conditions (i.e. bridges, straight/curved roadways). In the proposed framework, the accident condition of each vehicle in the simulated traffic flow will be checked at every minute to assess the overall vehicle safety performance. Vulnerable vehicle ratio at every minute is defined as the ratio of the number of vehicles that experience rollover or sideslip accidents to the total number of vehicles in the traffic flow. Since the simulated traffic flow is essentially stochastic the traffic safety performance of the traffic flow needs to be assessed statistically. The same experiments are repeated over time continuously by evaluating the passing vehicles through the same observation window. Based on the basic statistical analyses of the results from the repeated experiments, vehicle accident vulnerability of the traffic flow is characterized by an index, which is the median value of the vulnerable vehicle ratios throughout the entire simulation time, which can be expressed in Eq. (5.17).

$$V_u = M\{R_1, R_2, \cdots, R_T\} \tag{5.17}$$

where V_u is the vehicle accident vulnerability index of the traffic flow; $R_i = n_i/N_i$, R_i is the ratio of the vulnerable vehicles at the i^{th} minute, n_i is the number of vehicles that experience rollover or sideslip accidents at the i^{th} minute, N_i is the total number of vehicles in the traffic at the i^{th} minute; T is the total number of repeated experiments; M refers to median.

5.3 Demonstrative study

5.3.1 Prototype highway system and traffic flow simulation

The prototype highway system (Fig. 5.5) in the present study consists of a long-span bridge, a straight roadway on the left side, and a curved roadway with a radius of 400 m on the right side. The lengths of the bridge and roadway on each side are 836.7 m and 300 m, respectively, making the total length 1,436.7 m for this "roadway–bridge–roadway" system.

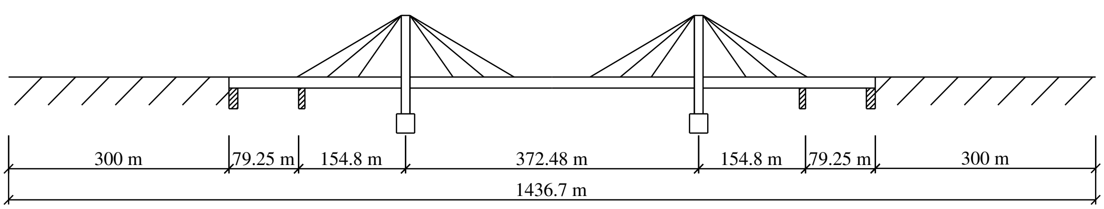

(a) Elevation view

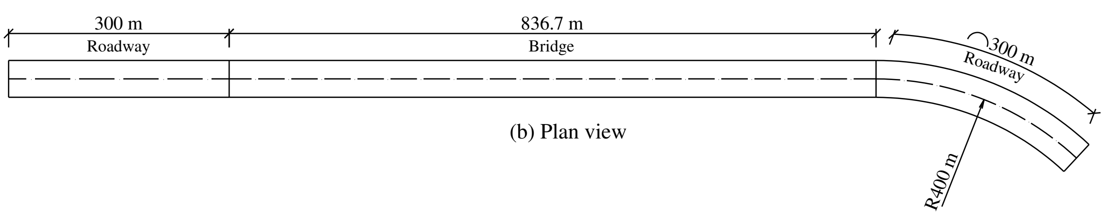

(b) Plan view

Figure 5.5 Prototype highway system

In the CA model, the highway system is discretized as many identical cells with a length of 0.5 m for each. Therefore, there are a total of 2,880 cells in one lane, including 1,680 cells for the bridge and 600 cells for each of the two approaching roadways. The vehicle driving speed limit is assumed to be 30 m/s

(108 km/h). The three types of vehicle groups that are considered to capture the main traffic classifications on highways are cars, vans, and trucks. Their proportions in the traffic flow are typically obtained from site-specific traffic data collection and are assumed to be 50%, 25%, and 25% for demonstrative purposes, respectively. The lengths of cars, vans, and trucks in this model are defined as 5 m, 7.5 m, and 12 m, occupying 10 cells, 15 cells, and 24 cells, respectively. According to Wang et al. (2007), normal acceleration and deceleration rates usually range from 1 to 2 m/s^2 and 1 to 3 m/s^2, respectively. In this paper, the acceleration/deceleration rates of cars, vans and trucks are set as 2 m/s^2, 1.5 m/s^2, and 1 m/s^2, respectively. The limited deceleration capability of 5 m/s^2 have been used in (Li 2016; Larraga and Alvarez-Icaza 2010), which is considered an acceptable value for an emergency braking maneuver. Therefore, the maximum braking capacity of all three types of vehicles is set as 5 m/s^2. Detailed parameters in dynamics models of three types of vehicles are listed in Table 5.1. Traffic flows with occupancy of 0.07, 0.18, and 0.25, correspond to level B (9 veh/km/lane), D (20 veh/km/lane), and F (34 veh/km/lane) defined in the Highway Capacity Manual (2000).

Following the method used by Chen and Wu (2011), those three traffic scenarios are called free, moderate, and busy traffic flow, respectively, which are considered in this study for comparison purpose. The probability of randomization deceleration is assumed to be $0.5 * \sqrt{\rho}$, in which ρ is the traffic occupancy (Yamg et al. 2007). The lane-changing probability is set as 0.5 and the total simulation time duration is 18,000 s and the time step of the simulation is 1 s. To capture the steady traffic flow characteristics, the simulation results of the first 14,400 s are discarded and only those of the last 3,600 s will be used and presented in the following sections. Time-space diagrams of free, moderate and busy flow are shown in Fig. 5.6. Vehicles move with the maximum speed (speed limit) in the free flow (Fig. 5.6a), while vehicles experience slow-down or braking due to the existence of traffic jam in the moderate and busy flow (Figs. 5.6b and 5.6c). The mean driving speed of free, moderate and busy flow are 29.7 m/s, 25.0 m/s and 12.6 m/s, respectively. Because the time step of accident simulation is 0.001 s, the time interval of vehicle speed will be transformed to 0.001 s by linear interpolation before accident simulation is conducted.

Table 5.1 Parameters in dynamics models of three types of vehicles

Parameters	Value			Unit
	Car	Van	Truck	
Sprung mass	1515	6244	10443	kg
Front unsprung mass	111	353	545	kg
Rear unsprung mass	108	500	2088	kg
Distances between front axle and sprung mass	1.19	2.56	4.51	m
Distances between rear axle and sprung mass	-1.71	-1.54	-1.59	m
Height of the center of sprung mass	0.47	1.15	0.653	m
Height of center of mass for whole vehicle	0.67	1.5	1.212	m
Height of lateral wind load	0.9	1.3	1.663	m
Height of rolling center	0.25	0.83	0.737	m
Wheel width	1.6	1.86	1.829	m
Active roll torque	0	0	0	kN-m
Tire cornering stiffness of front tires	70	146	181	kN/rad
Tire cornering stiffness of rear tires	130	196	648	kN/rad
Roll stiffness of front suspension	102	380	156	kN-m/rad
Roll stiffness of rear suspension	45	684	1590	kN-m/rad
Roll damping rate of front suspension	100	100	100	kN/rad
Roll damping rate of rear suspension	239	239	239	kN/rad
Roll stiffness of front tires	1000	1648	2060	kN-m/rad
Roll stiffness of rear tires	1500	2336	1776	kN-m/rad
Height of center of front/rear unsprung mass	0.35	0.53	0.508	m
Roll moment of inertia of sprung mass	689	8470	7466	kg-m^2
Yaw-roll product of inertia of sprung mass	31	1680	3590	kg-m^2
Yaw moment of inertia of sprung mass	3374	13967	52517	kg-m^2
Reference area	2.5	7	10	m^2
Vehicle length	5	7.5	12	m

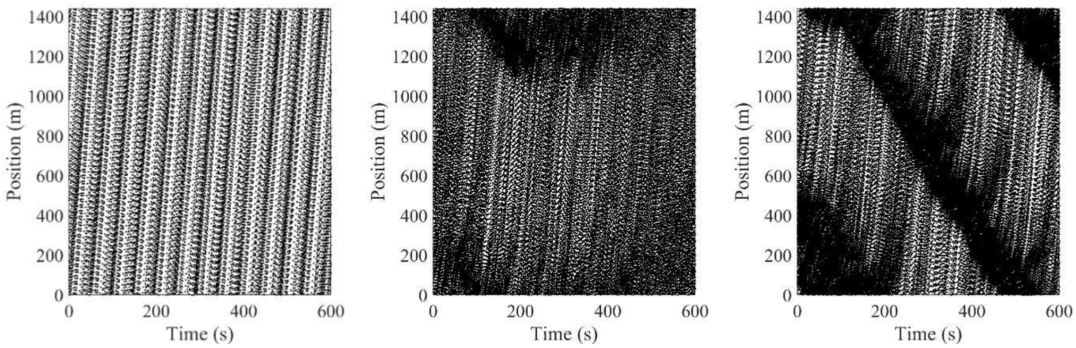

(a) Free flow (b) Moderate flow (c) busy flow

Figure 5.6 Time-space diagrams

5.3.2 Demonstration of accident safety assessment method

A case study is conducted to demonstrate how the accident safety assessment method illustrated in Section 5.2.3 can be used to obtain the accident vulnerability. In the case study, the moderate traffic flow (occupancy = 0.18) through the highway system under an icy surface condition is investigated. The safety performance of vehicles in the traffic flow under sudden crosswinds is evaluated at every minute. The traffic flow simulation time is 60 minutes, so there will be a total of 60 vulnerable vehicle ratios for each crosswind case. The box plots of vulnerable vehicle ratios with varying wind velocities are shown in Fig. 5.7. For each box plot, the range between the first quartile and the third quartile is less than 0.05, and the range between the upper whisker (the upper adjacent value) and lower whisker (the lower adjacent value) is less than 0.15. Despite some extreme outliers, most of the data falls into a relatively narrow range. Therefore, it is reasonable to select the median of vulnerable vehicle ratios to represent the accident vulnerability of a traffic flow for a specific hazardous scenario in this study.

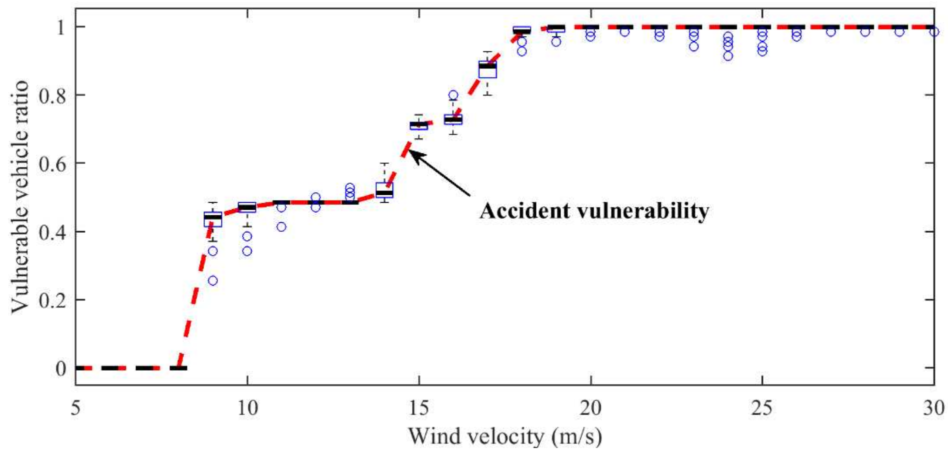

Figure 5.7 Vulnerable vehicle ratios with varying wind velocity

5.3.3 Influence of different road surface conditions

Accident vulnerabilities of vehicles in the moderate traffic flow (occupancy = 0.18) through the highway system under different road surface conditions are given in Fig. 5.8. The accident vulnerability is found to be very sensitive to the road surface conditions. Among the three different road surface conditions, the icy road surface poses the greatest threat to vehicle accidents, whereas the dry road surface does the least. Despite the significant difference, accident vulnerability of vehicles exhibits a similar trend for all three road surface conditions: it starts from 0 when the wind velocity is relatively low, and then increases as the wind velocity increases, and finally reaches 1.0 when the wind velocity is high enough. Rollover and sideslip accident vulnerability under different road surface conditions, characterized by the respective vulnerability indexes, are shown in Fig. 5.9 and Fig. 5.10, respectively.

As can be seen in Fig. 5.9, rollover accident vulnerability under the three road surface conditions are very close, indicating that road surface conditions have limited influence on rollover accidents. By comparing Fig. 5.8 and Fig. 5.9, it can be found that the two curves related to the dry road surface condition are almost identical, which suggests that only rollover accidents occur under the dry surface condition.

Meanwhile, it is found in Fig. 5.10 that the sideslip accident vulnerability is always zero under the dry road surface condition. As shown in Fig. 5.10, as the wind velocity increases, sideslip accident vulnerability of vehicles on both icy and snowy roads increases first and then decreases to 0. Therefore, it is found that, on ice- or snow-covered roads, sideslip accidents are dominant when the wind velocity is relatively low, whereas rollover accidents are dominant when the wind velocity is high. Moreover, compared to the snowy surface condition, the icy surface condition poses much greater threats on vehicles in terms of sideslip accidents.

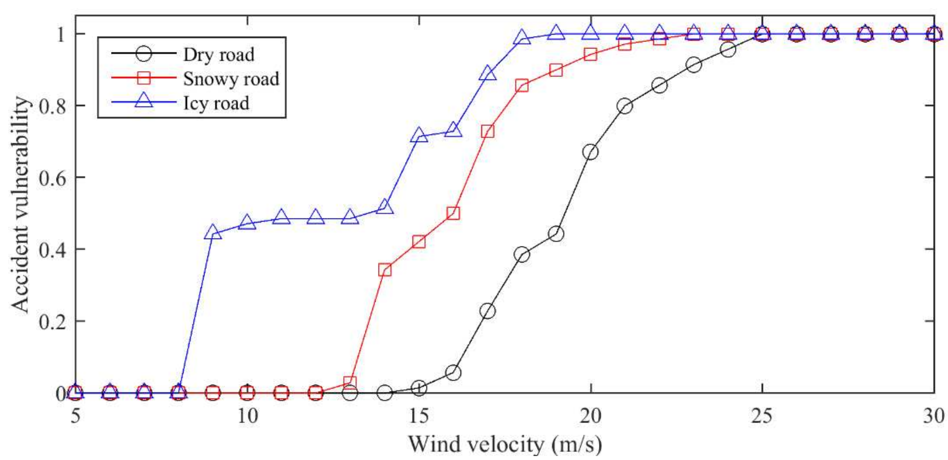

Figure 5.8 Accident vulnerability index of vehicles under different road surface conditions

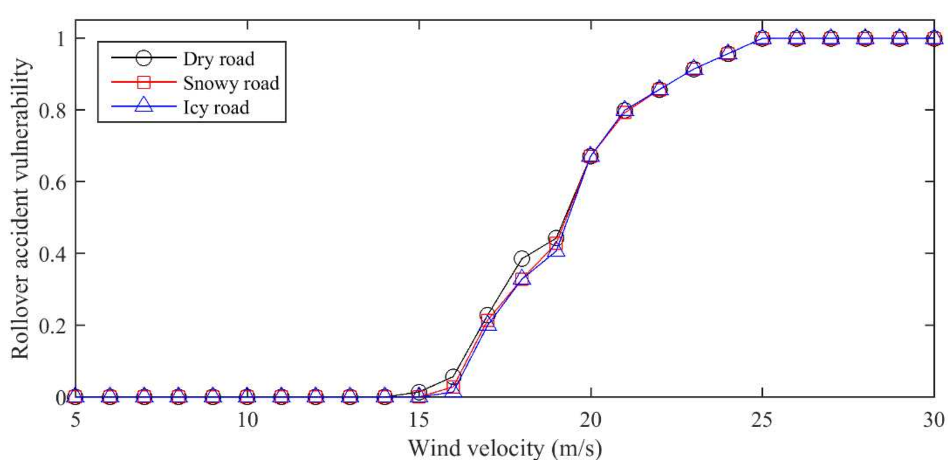

Figure 5.9 Rollover accident vulnerability index of vehicles under different road surface conditions

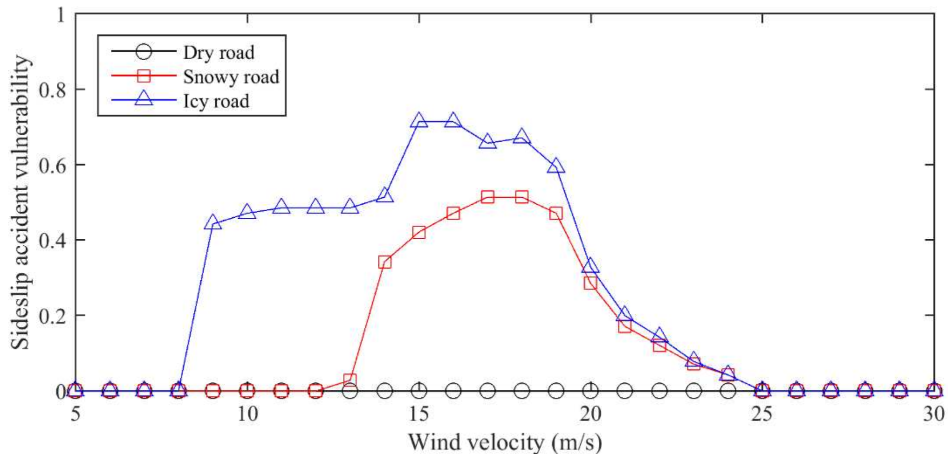

Figure 5.10 Sideslip accident vulnerability index of vehicles under different road surface conditions

5.3.4 Influence of different road geometry

As a major component of road geometric design, curved road segments typically contribute to a much higher accident rate than their straight counterparts, especially under adverse driving conditions, such as windy weather and a snow/ice-covered road surface (Chen and Chen 2010; Xi et al. 2014). Compared to bridges with open surrounding environments, wind fields around roadways can be significantly influenced by nearby topography such as hills, trees, bushes and buildings due to the wind sheltering effect. Depending on the specific roadside environment, wind velocity near the roadways could be reduced to different extents (Li et al. 2007). In this regard, under crosswind conditions, vehicles moving on bridges may be more likely to experience accidents than those moving on roadways. In order to understand the influence of different road geometries on vehicle accidents, accident vulnerabilities of vehicles on straight roads, bridges and curved roads of the highway system are investigated. A reduction factor (*RF*) of wind velocity is used to approximately consider the wind sheltering effect on vehicle safety due to the roadside environments, which is defined in Eq. (5.18) (Li et al. 2007).

$$RF = \frac{U}{\overline{U}_\infty} \tag{5.18}$$

where U is the velocity of wind acting on the vehicles; $\overline{U}_\infty$ is the incoming free stream velocity.

In order to conduct a parametric study, RF is assumed to be 1.0 or 0.6 for vehicles on roadways subjected to different levels of shielding effects due to hills, bushes, trees or wind barriers. It is assumed there is no wind barrier installed on the bridge, so the RF is 1.0 for vehicles on the bridge. Without losing generality, the influence of dynamic interactions between the bridge and vehicles on vehicle accidents is not considered in this study because such effects can be very bridge-specific and hard to generalize. Accident vulnerability results from the traffic flow in the moderate traffic through different road segments are shown in Fig. 5.11. As shown in Fig. 5.11a, the accident vulnerabilities of vehicles on the straight road are very close to those of vehicles on the bridge under the dry surface condition when the wind sheltering effect is not considered.

Compared to vehicles on the bridge and straight road, those on the curved road are more likely to experience accidents without considering the sheltering effect. The possible reason is that the effect of road superelevation on the vehicle instability is far greater than that of reduced wind forces due to road curvature. When the wind sheltering effect is considered, the accident vulnerability of vehicles on the straight road and the curved road decreases significantly because of the reduced wind forces. As expected, when the wind sheltering effect is not considered, accident vulnerability of vehicles on the bridge and the straight road under icy surface conditions are very close, as shown in Fig. 5.11b. However, vehicles on the straight road, in general, have a slightly smaller probability of accidents than those on the bridge and the curved road, likely due to the fact that sideslip accidents on the icy road are mainly influenced by reduced wind forces due to road curvature. When the wind sheltering effect is considered, the accident vulnerability of vehicles on the straight and curved roads reduce considerably. Such results suggest that it may become possible to improve vehicle safety under strong crosswinds in some vulnerable areas through providing wind sheltering.

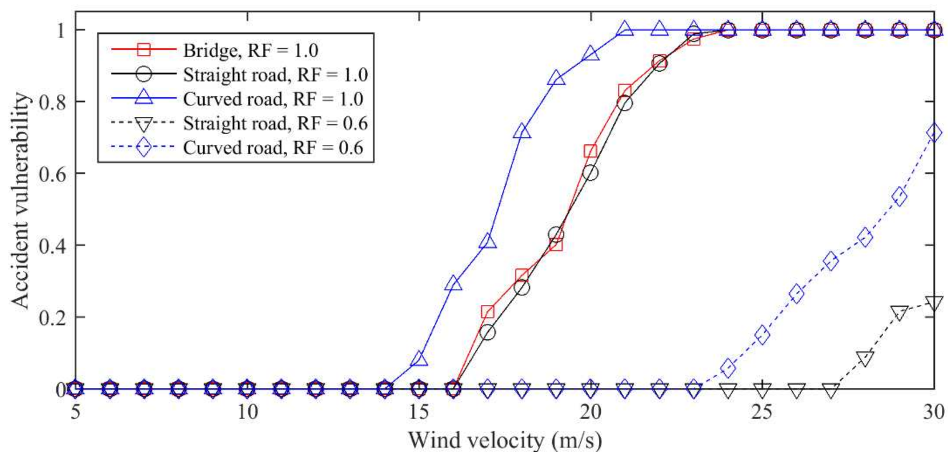

(a) Dry road surface

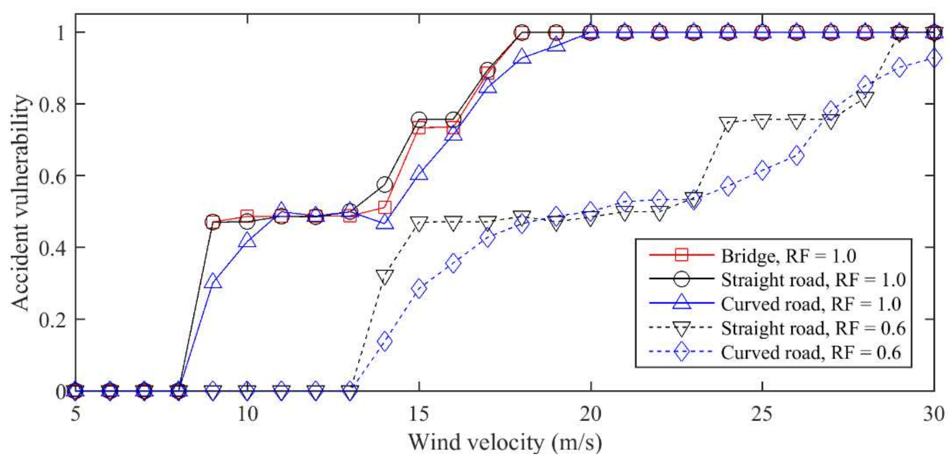

(b) Ice-covered road surface

Figure 5.11 Accident vulnerability index of vehicles in traffic through different road segments

5.3.5 Influence of vehicles with different types

As discussed earlier, different types of vehicles have different safety performances even under the same hazardous condition. In order to further investigate the influence of vehicle types, accident vulnerabilities of cars, vans, and trucks in moderate traffic flow through the highway system are compared in this section.

Critical driving speed (CDS) of accidents is the highest driving speeds under which an accident will occur based on the accident criteria (Chen and Chen 2010). The CDS for three representative vehicles on a straight road with icy surface conditions are shown in Fig. 5.12. Fig. 5.13 gives the accident vulnerability of vehicles of different types under different road surface conditions. It can be seen in Fig. 5.13a that the accident vulnerability presents a very similar trend for all three types of vehicles under dry surface conditions. This is partly because rollover accidents are dominant on the dry road for all three types of vehicles. In general, trucks are slightly more vulnerable to an accident than vans. Compared to trucks and vans, cars have a much smaller probability to rollover, likely due to the fact that they have a lower center of gravity and smaller frontal area. Different from the case of dry surface conditions, cars have greater accident vulnerability than trucks and vans on snow-covered roads, as shown in Fig. 5.13b. This is because, under snowy surface conditions, sideslip accidents dominate when the wind velocity is relatively small, and cars are more likely to sideslip than trucks and vans.

A very similar trend can be observed for trucks and vans, although vans have greater accident vulnerability than trucks when the wind velocity is between 18 m/s and 21 m/s. It is found from Fig. 5.13c that the accident vulnerability is very sensitive to the wind velocity for all three types of vehicles on the ice-covered road. For example, the accident vulnerability of cars increases from 0 to 0.9 as the wind velocity increases from 8 m/s to 9 m/s. As discussed earlier, sideslip accidents are dominant under the icy surface and relatively low wind speed condition. Meanwhile, as shown in Fig. 5.12, sideslip accidents on the icy road are not sensitive to the driving speeds of vehicles. This means that sideslip accidents on icy roads are mainly controlled by the wind velocity, instead of the varying driving speeds of vehicles in the traffic flow.

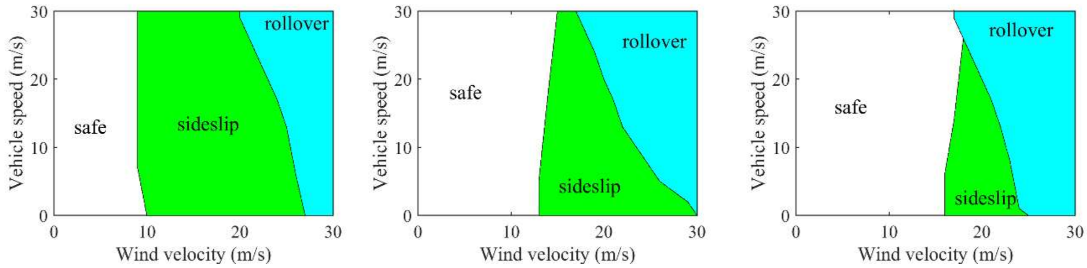

(a) Car (b) Van (c) Truck

Figure 5.12 CDS of accidents for three vehicles on a straight, icy road

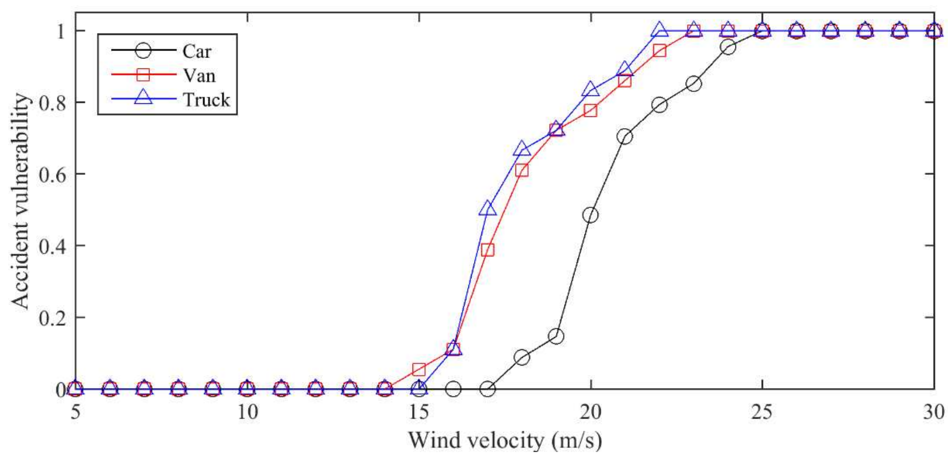

(a) Dry road surface

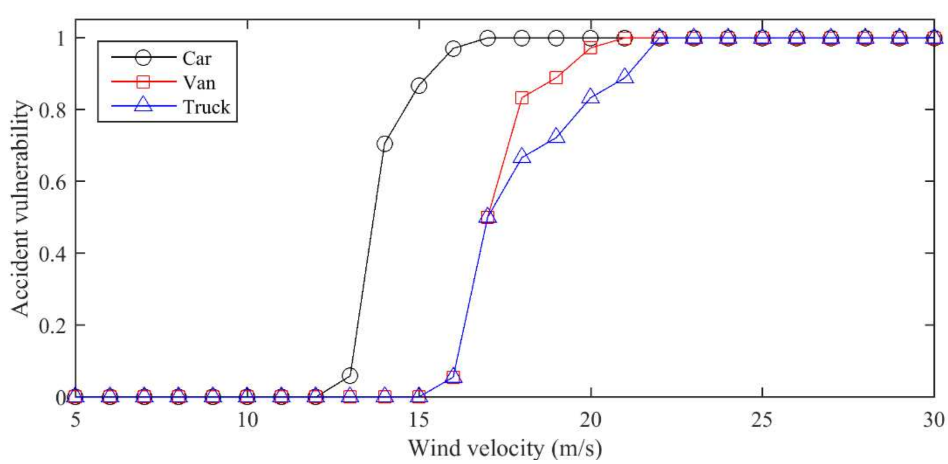

(b) Snow-covered road surface

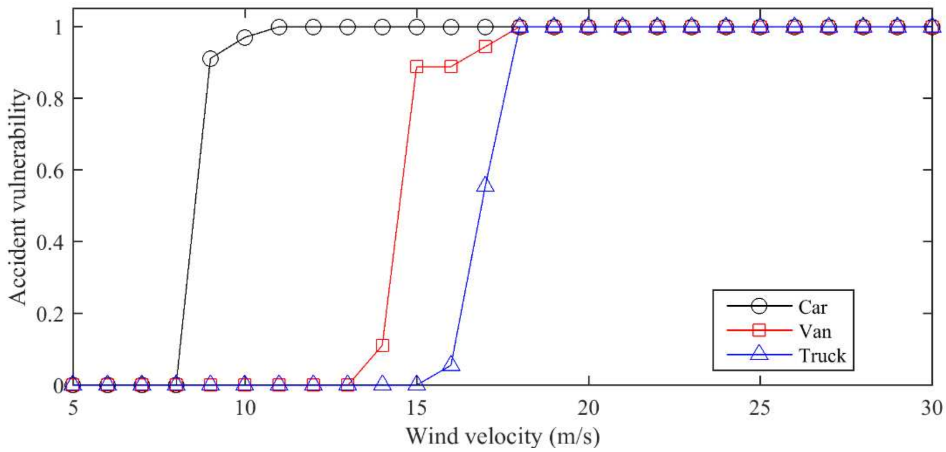

(c) Ice-covered road surface

Figure 5.13 Accident vulnerability index of vehicles with different types

5.3.6 Influence of traffic flow with different occupancy

Drivers in free flow tend to drive with their desired speeds and rarely brake, whereas they must drive with relatively low speeds and apply brakes frequently in busy flow. The vehicle driving speed has a great influence on the instability of a vehicle under crosswinds due to its contribution to the wind forces on the vehicle. Therefore, accident vulnerabilities of vehicles are likely to be influenced by traffic occupancy in terms of different driving speeds of vehicles in different traffic flow. To further assess the influence of traffic occupancy on accident vulnerability, accident simulations are performed for vehicles in free, moderate, and busy traffic flow. Accident vulnerabilities of vehicles in traffic flow with different occupancies are given in Fig. 5.14. It can be seen in Fig. 5.14a that, under the dry surface condition, the accident vulnerability of vehicles in free flow is the highest, while that of vehicles in busy flow is the lowest. This can be explained by the fact that vehicles in free flow generally have a higher driving speed than those in moderate or busy flow. Higher vehicle speeds lead to larger wind forces acting on the vehicles in general, which in turn contribute to higher accident vulnerability. It is also found in Fig. 5.14a that the accident vulnerability of vehicles in busy flow is less than 1 under a crosswind speed of 30 m/s. This is possibly because some vans with driving speeds less than 5 m/s in busy flow will not experience an accident even under a crosswind with relatively high velocity.

The accident vulnerability of vehicles on a snowy road exhibits a similar trend to vehicles on a dry road, as shown in Fig. 5.14b. It is shown the critical wind velocity of accidents on the snowy road is 13 m/s, which is 2 m/s less than that of accidents on the dry road. Moreover, compared to the dry surface condition, the differences between different occupancies become smaller under snowy surface conditions. This is partly because sideslip accidents, which are generally dominant on snowy roads, are not sensitive to driving speeds of vehicles.

The accident vulnerability of vehicles in free, moderate and busy flow under icy conditions are rather close (Fig. 5.14c). Compared to dry and snowy surface conditions, the critical wind velocity is much smaller on an icy road surface (9 m/s) and sideslip accidents dominate. For sideslip accidents on an icy road, the CDS of vans and trucks generally increases with the increase of wind velocity (Fig. 5.12b and 5.12c). This explains why vehicles in busy flow have the highest accident vulnerability, while those in the free flow have the lowest, as shown in Fig. 5.14c.

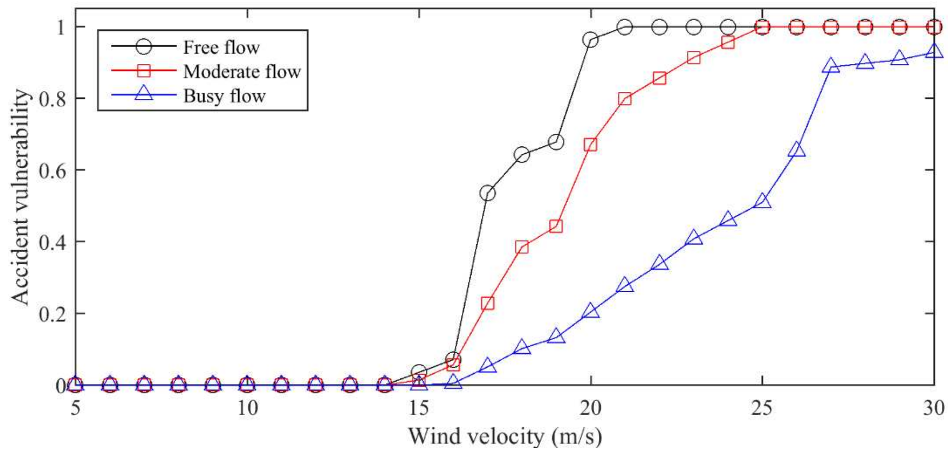

(a) Dry road surface

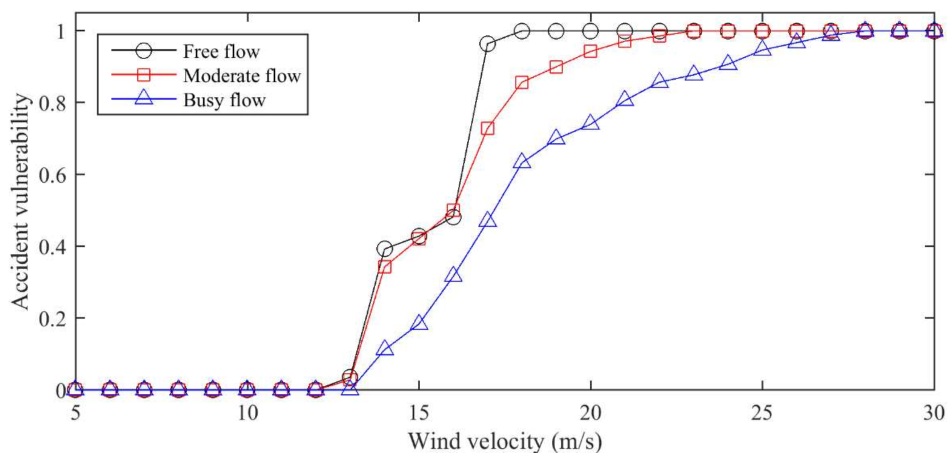

(b) Snow-covered road surface

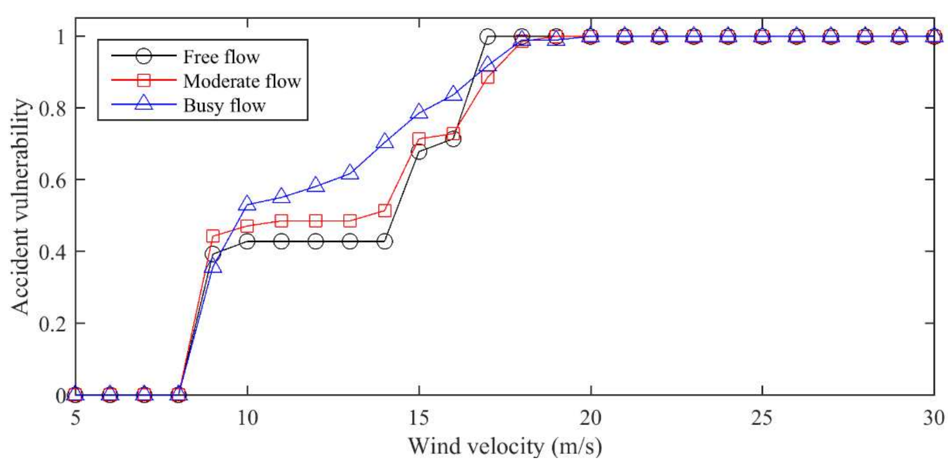

(c) Ice-covered road surface

Figure 5.14 Accident vulnerability index of vehicles in traffic with different occupancy

5.4 Conclusions

An integrated framework was proposed to evaluate the overall safety performance of vehicles in realistic stochastic traffic passing through highway infrastructure systems. Vehicle accident vulnerability was introduced as an overall safety index for the whole traffic, which may be used as an important resilience indicator for future resilience studies involving traffic safety. The proposed framework was applied to a bridge-roadway system for demonstration purposes. It was found that the proposed framework could provide rational estimation of the safety performance of traffic flow with findings consistent with existing studies and common observations. It is noted that with the site-specific data of traffic, road and environment, the proposed framework can provide more specific and insightful observations that may help traffic management under hazardous conditions. The main conclusions from the demonstrative study are summarized as follows:

(1) Among the three different road surface conditions, the icy road surface poses the greatest threat to vehicle accidents, whereas the dry road surface poses the least. Rollover accident vulnerability under the three road surface conditions are very close. On a dry road surface, only rollover accidents may occur. On icy or snow-covered roads, sideslip accidents are dominant when the wind velocity is relatively low, whereas rollover accidents are dominant when the wind velocity is high.

(2) Compared to vehicles on the bridge and the straight road, those on the curved road are more likely to experience accidents without considering the sheltering effect. When the wind sheltering effect is considered, the accident vulnerability of vehicles on the straight road and the curved road decreases significantly because of the reduced wind loads acting on the vehicles.

(3) Trucks are slightly more likely to experience an accident than vans on dry roads. However, vans have greater accident vulnerability than trucks on snowy and icy roads in general. Among the three types of vehicles, cars have the smallest possibility to experience an accident under dry road surface conditions, whereas they have the largest possibility to experience an accident under snowy and icy surface conditions.

(4) The accident vulnerability of vehicles is influenced by the traffic occupancies in terms of the driving speed of vehicles. Under dry and snowy road surface conditions, vehicles in free flow have the highest accident vulnerability, whereas those in busy flow have the lowest. However, under icy road surface conditions, in general, vehicles in busy flow have the highest accident vulnerability, whereas those in free flow have the lowest.

(5) This study has many potential applications, such as improved traffic planning and emergency response prioritization considering not only typical travel time, but also traffic safety risks and associated possible delay in adverse conditions. Driving safety of connected and autonomous vehicles (CAV) in hazardous driving environments is one major challenge. Another potential application of this study is to contribute to the development of more advanced algorithms of CAVs in the future.

(6) This study provides an innovative and promising simulation tool, but it also has some limitation for future improvement. The main limitation is the proposed traffic flow safety model needs better calibration and validation. Due to the rarity of traffic data in adverse driving conditions, this is expected to be conducted in the future when the data becomes available.

CHAPTER 6 PROBABILISTIC MODELING OF DISRUPTED INFRASTRUCTURES DUE TO FALLEN TREES SUBJECTED TO EXTREME WINDS IN URBAN COMMUNITY[5]

6.1 Introduction

Tree failures due to strong winds in urban areas cause extensive direct and indirect economic and environmental loss, including disrupting adjacent infrastructures, such as buildings, underground pipelines, roads and overhead powerlines. To effectively improve the resilience of a community subjected to extreme wind events through prevention, response and recovery, it becomes critical to rationally assess the risks of wind-induced tree failures and the disruptions to different types of infrastructures due to fallen trees. An integrated probabilistic methodology to model the performance of disrupted infrastructures is developed for fallen urban trees subjected to extreme winds in a typical community. Firstly, the finite-element modeling of the trees subjected to wind loads is conducted and based on which, the windthrow fragility curves of several typical urban tree species are developed. Secondly, a probabilistic framework is developed based on the fragility results to characterize the disrupted scenarios and further predict the disruption probability of some critical infrastructures due to fallen trees. The matrix-based system reliability (MSR) method is introduced to assess the transportation network performance. The proposed framework and MSR method are demonstrated in detail on studying the overhead powerline and transportation network of a small urban community in the city of Fort Collins, Colorado. In the demonstrative example, the probabilities of powerline disruption, road closure, and origin-destination (OD) disconnection and travel time reliability under different wind conditions are predicted. Finally, mitigation efforts such as crown thinning of trees are

[5] This chapter is submitted to a journal in a paper that is currently under review (Hou and Chen 2019b).

discussed to reduce possible risks of disrupting the infrastructures.

6.2 Fragility model of urban trees subjected to extreme winds

6.2.1 Description of urban trees

Depending on their species and ages, different trees have different profiles. To characterize a specific tree, there are some commonly used parameters, such as age, tree height, diameter at breast height (DBH), crown height and crown diameter. Tree allometry is widely used in forest management to establish the quantitative relationship between these parameters, with which some hard-measured parameters can be predicted with an easily measured one. With allometric equations, DBH can be predicted with age and total height. Crown diameter and crown height can be predicted with DBH. In urban forestry, allometric equations can help urban forest managers in selecting species, developing tree removal and replacement plans, and estimating management costs and ecosystem services (Peper et al. 2014). Measured field data are important in the development of reliable allometric equations. U.S. Forest Service Pacific Southwest Research Station measured 14,487 urban street and park trees in 17 U.S. cities, constructed the Urban Tree Database (UTD), and developed 365 sets of allometric equations for 171 distinct tree species (McPherson et al. 2016).

In this study, the measured tree data of the city of Fort Collins in Colorado from the UTD are used to develop allometric equations for three popular street tree species including American basswood, Green ash, and Ponderosa pine. Compared to other parameters, tree height is much easier to be measured, and is also a more intuitive input for a mechanistic tree model. In this study, we adopt tree height to estimate DBH, crown height, and crown diameter with the polynomial models developed by McPherson et al. (2016). A linear model is used to fit the data points of three tree species, which has the following form.

$$y_i = a + bx_i + \frac{\varepsilon_i}{\sqrt{w_i}} \tag{6.1}$$

where y_i is the measurement of tree i, which refers to DBH, crown diameter and crown height; a and b are constants to be estimated; x_i is the height of tree i; ε_i is the random error for tree i with $\varepsilon_i \sim N(0, \sigma^2)$; σ^2 is the variance of the random error; w_i is the weight and $w_i = 1/x_i^2$.

Statistical analysis was conducted using MATLAB and the regression plots for American basswood are given in Fig. 6.1. Regression results for three tree species are listed in Table 6.1. It is seen that the adjusted R^2 values are larger than 84% for DBH, crown diameter, and crown height, indicating good fitting results. With the developed allometric equations, a tree can be defined with tree height, facilitating the following development of fragility curves for different tree classes in terms of tree height.

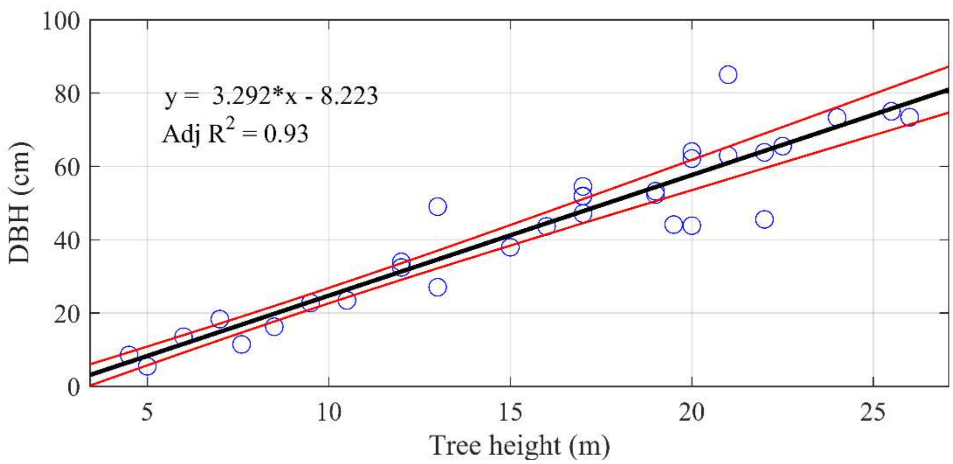

(a) DBH

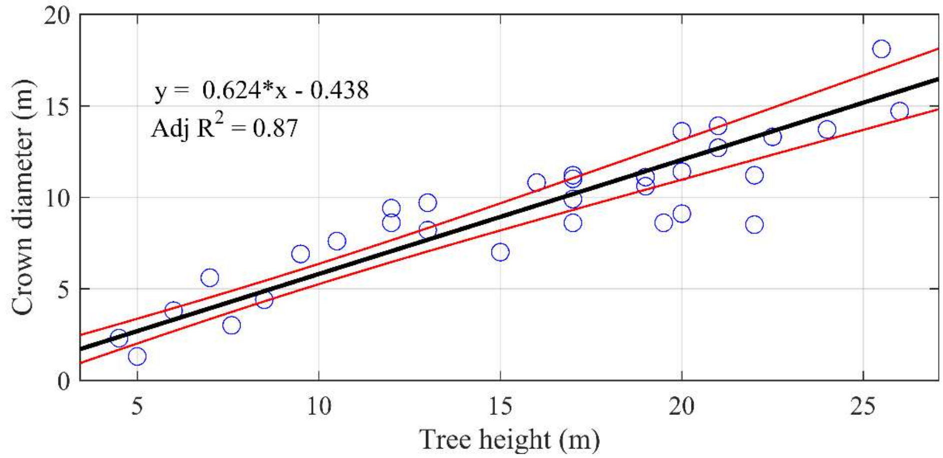

(b) Crown diameter

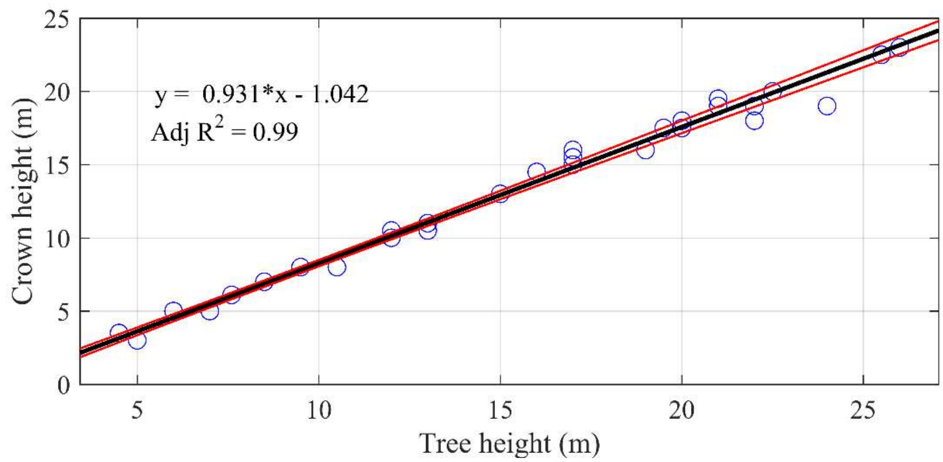

(c) Crown height

Figure 6.1 Regression plot for American basswood

Table 6.1 Regression results

Tree species	DBH			Crown diameter			Crown height		
	a	b	Adj R^2	a	b	Adj R^2	a	b	Adj R^2
American basswood	3.292	-8.223	0.93	0.624	-0.438	0.87	0.931	-1.042	0.99
Green ash	4.379	-10.41	0.89	0.892	-0.589	0.88	0.808	-0.383	0.97
Ponderosa pine	3.74	-2.195	0.84	0.673	0.388	0.86	0.815	0.252	0.94

6.2.2 Mechanistic tree model

A mechanistic tree model is built with direct stiffness method, which describes the behavior of a tree under winds, and computes the internal forces of the tree structure. With a sufficient number of elements, a tapered tree stem can be discretized into multiple beam elements with an approximate uniform cross section for each element as shown in Fig. 6.2. The properties of the uniform cross sections are defined based on those at the middle point of each element, following typical finite element modeling technique of tapered structures. Based on the applied external forces, element properties, and boundary conditions, the equilibrium equations of the discretized tree system are formulated into a matrix relationship. Then, free nodal displacements, support reactions and element forces are numerically solved with the tree finite element model (FEM).

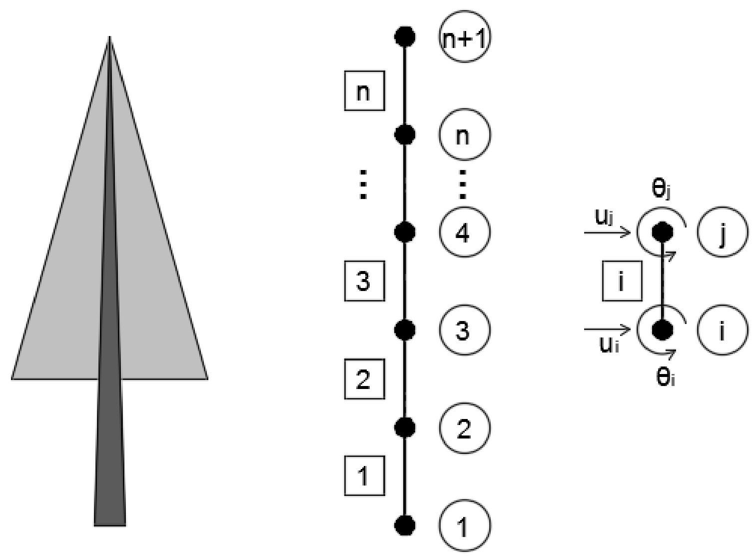

Figure 6.2 Finite element model of a tree

6.2.2.1 Wind loads

Although aerodynamic analysis of trees subjected to wind is supposed to generate more accurate results of tree response under winds, it requires tree-profile-specific wind coefficients typically obtained from wind tunnel tests, which are not yet available. In addition, the additional high computational cost of aerodynamic analysis will also cause overwhelming computational burden for the following fragility analysis. Therefore, in this study, only aerostatic analyses of the trees are conducted. The 3-s gust wind speed is used to calculate the wind forces acting on the tree in this study and the 3-s gust wind profile can be defined in the power-law form (Simiu and Miyata 2006) as expressed in Eq. (6.2):

$$V(z) = V(10)\left(\frac{z}{10}\right)^{\alpha} \tag{6.2}$$

where z is height (m); $V(z)$ is the 3-s gust wind speed at height z (m/s); α is the ground roughness coefficient, which is taken as 0.143 for suburban terrain and town.

The horizontal wind forces acting on both the stem and crown are considered, which are calculated based on the wind profile, the stem taper equation and the assumed crown shape. The uniformly distributed drag forces (Unit: N/m) acting on stem element i can be expressed as follows:

$$F_{WS,i} = 0.5\rho_{air}C_{dS}D_{S,i}V_i^2 \tag{6.3}$$

where ρ_{air} is the air density (kg/m^3); C_{dS} is the drag coefficient of the stem; $D_{S,i}$ is the diameter at the mid-height of stem element i (m), which is determined by the stem taper equation $D_S(h)$; h is the tree height (m) and V_i is the 3-s gust wind speed at the mid-height of element i (m/s).

Without specific tree profile data, the unstreamlined crown projection area against the wind is computed by assuming the tree crown has a triangular shape (Peltola et al. 1999). The canopy becomes streamlined as the wind speed increases, leading to a reduction of crown area, which is assumed to be controlled by a streamlining coefficient, S_t (Peltola et al. 1999). The uniform distributed drag forces (Unit: N/m) acting on the crown element i can be given by:

$$F_{WC,i} = 0.5\rho_{air}C_{dC}D_{C,i}S_tV_i{}^2 \tag{6.4}$$

where C_{dC} is the drag coefficient of the crown; $D_{C,i}$ is the diameter at the mid-height of crown element

i (m).

6.2.2.2 Self-weight

Self-weight of a tree does not only contribute to the normal compressive stress in the stem, but also brings additional moment due to the P-Delta effects under wind loads, which further increases the axial compressive stress. The total weight of each element is the sum of the weights of the stem and crown. The weight of stem element i is calculated as follows:

$$F_{GS,i} = 0.25\rho_S g L_i \pi D_{S,i}^2 \tag{6.5}$$

where ρ_S is the stem density (kg/m^3); g is the acceleration of gravity (m/s^2). Similarly, the weight of crown element i is calculated through Eq. (6.6):

$$F_{GC,i} = 0.25\rho_C g L_i \pi D_{C,i}^2 \tag{6.6}$$

where ρ_C is the crown density (kg/m^3), which is estimated by assuming a constant ratio between the crown and stem weights.

6.2.2.3 Application of direct stiffness method

To consider the P-Delta effects due to gravity forces, 1st order analysis is performed to obtain the axial forces in each element, based on the computed stem and crown weights. Then, the geometric stiffness matrix k_G of each element is calculated based on the obtained axial forces. For a beam element, k_G is only a function of the element's length and the axial force in the element, which can be computed by Eq. (6.7).

$$k_G = \frac{N}{30L}\begin{bmatrix} 36 & 3L & -36 & 3L \\ 3L & 4L^2 & -3L & -L^2 \\ -36 & -3L & 36 & -3L \\ 3L & -L^2 & -3L & 4L^2 \end{bmatrix} \tag{6.7}$$

where N is the axial force in a beam element; L is the element length.

By adding the geometric stiffness matrix k_G to the elastic stiffness matrix k_E as defined in Eq. (6.8), we can obtain the total stiffness matrix $k_E + k_G$ for each element, which will be assembled into the global stiffness matrix $K_E + K_G$. The wind forces acting on each element will be converted to equivalent nodal loads, and then assembled into the global nodal load vector F.

$$k_E = \frac{EI}{L^3}\begin{bmatrix} 12 & 6L & -12 & 6L \\ 6L & 4L^2 & -6L & 2L^2 \\ -12 & -6L & 12 & -6L \\ 6L & 2L^2 & -6L & 4L^2 \end{bmatrix} \tag{6.8}$$

where E is the modulus of elasticity; I is the moment of inertia.

Finally, the equations of the global system can be derived as Eq. (6.9).

$$(K_E + K_G)U = F \tag{6.9}$$

where U is the global nodal displacement.

By solving Eq. (6.9), the global nodal displacements can be obtained:

$$\mathrm{U} = (K_E + K_G)^{-1}F \tag{6.10}$$

With the global nodal displacements, the support reactions, and element forces can be calculated. Under the combined effect of bending moment and normal forces, the total compressive stress (Pa) in the outer fibers of stem element i is given as

$$\sigma_i = \frac{M_i}{I_i}\frac{D_{S,i}}{2} + \frac{N_i}{A_i} \tag{6.11}$$

where M_i is the moment in element i; N_i is the axial force; I_i is the moment of inertia; A_i is the area.

6.2.3 Limit state

There are two failure modes for a tree under strong winds: stem breakage and uprooting. Stem breakage occurs when the maximum compressive stress σ_{max} in the stem exceeds the stem modulus of rupture σ_R. The limit state defining the stem breakage of a tree can be expressed as

$$g_b = \sigma_R - \sigma_{max} \tag{6.12}$$

It is possible that stem breakage only occurs at a small portion of the crown top, for example, the top tip of the crown, which may not necessarily cause potential infrastructure disruption (e.g. road blockage). Therefore, the stem breakage condition is assessed based on the elements below the mid-crown height to avoid overrepresentation of infrastructure disruption. Once the stem breakage occurs, the breakage ratio, which is defined as the ratio of the length of the broken stem to the total tree height, will be recorded according to the breakage location.

Uprooting occurs when the critical turning moment M_o^{cri} provided by the root-soil plate anchorage is exceeded by the base turning moment M_{max} produced by wind. The critical overturning moment M_o^{cri} can be determined by tree pulling experiments and is strongly related to stem weight W_s (Gardiner et al. 2000). The relationship can be expressed as follows.

$$M_o^{cri} = C_{reg} W_s \tag{6.13}$$

where C_{reg} is the regression constant, which is dependent on species and soil conditions (NmKg^{-1}). Therefore, the limit state of uprooting of a tree can be expressed as

$$g_u = M_o^{cri} - M_{max} = C_{reg} W_s - M_{max} \tag{6.14}$$

6.2.4 Statistics of wind loads and mechanical properties of trees

Uncertainties exist in wind loads and mechanical properties of the trees, which need to be modeled probabilistically in fragility analyses. The statistics of the wind load-related parameters for different tree species are summarized in Table 6.2. It should be noted that the crown characteristics of deciduous trees (e.g. American basswood and Green ash) change between seasons. For example, the drag coefficient and weight of the crowns of deciduous trees in summer are larger than those in winter, making them more susceptible to windthrow. The crown characteristics of trees in summer are used in this study to be conservative. The drag coefficients of tree crown and stem, and the streamlining coefficient are assumed to follow normal distributions. For the three tree species studied here, the drag coefficient of the stems with cylinder cross sections is assumed to have a mean value of 1.0 and coefficient of variation (COV) of 0.1. According to Horacek (2003), the mean values of the drag coefficients of crowns for American basswood, Green ash and Ponderosa pine are 0.25, 0.25 and 0.3, respectively. The COVs for the three species are assumed to be 0.2. The mean values of the streamlining coefficients of three tree species are 0.4 following the study by Peltola et al. (1999), and the COV is assumed to be 0.2. Triangle has been proved to be an appropriate shape to model the reconfigured frontal crown shape under wind, which is used to calculate the wind loads acting on the crown. Deterministic stem taper equations for the three tree species developed by Westfall and Scott (2010) are used in this study.

Table 6.2 Wind load statistics of different tree species

Variables	Mean			COV	CDF	Source
	AB	GA	PP			
Drag coefficient of crown	0.25	0.25	0.30	0.2	Normal	Horacek (2003)
Drag coefficient of stem		1		0.1	Normal	Anderson Jr (2010)
Streamlining coefficient		0.4		0.2	Normal	Peltola et al. (1999)
Crown shape		Triangle			Deterministic	Peltola et al. (1999)
Stem taper equation		/			Deterministic	Westfall and Scott (2010)

(Note: AB, GA, and PP represent American basswood, Green ash, and Ponderosa pine, respectively.)

Table 6.3 summarizes the statistics of the mechanical properties for different tree species. Mechanical properties of trees are species-dependent and are usually obtained from extensive sampling and analysis procedures. In this study, without more statistical information, all these parameters are assumed to follow normal distributions. The statistics of the stem density, modulus of rupture, and modulus of elasticity for green wood of three tree species can be found in the Wood handbook (Ross 2010). The mean value and

COV of the crown to stem weight ratio, which can determine the crown density, are taken from the previous study by Peltola et al. (1999). The regression constant of Ponderosa pine is obtained from the pulling experiments (Gardiner et al. 2000), but no such data has been found for American basswood and Green ash in previous studies. It was found by Dupuy et al. (2005) that the tap root is twice as resistant as plate-like root of hardwood trees, such as American basswood and Green ash. Therefore, the regression constants of American basswood and Green ash are assumed to be half of that of Ponderosa pine in this study.

Table 6.3 Mechanical properties statistics of different tree species

Variables	Mean			COV	CDF	Source
	AB	GA	PP			
Stem density (kg/m^3)	320	530	380	0.1	Normal	Ross (2010)
Modulus of rupture (MPa)	34	66	35	0.16	Normal	
Modulus of elasticity (MPa)	7200	9700	6900	0.22	Normal	
Crown to stem weight ratio	0.4	0.3	0.4	0.25	Normal	Peltola et al. (1999)
Regression constant (NmKg^{-1})	67	67	134	0.2	Normal	Gardiner et al. (2000) Dupuy et al. (2005)

6.2.5 Development of fragility curves

Fragility function represents the probability of exceeding a limit state under a given hazard intensity:

$$Fragility = \Phi\left(\frac{\ln(im/m_R)}{\xi_R}\right) = P(EDP > LS|IM = im) \tag{6.15}$$

where $\Phi(\cdot)$ is the standard normal distribution function; $P(\cdot)$ is the probability function; IM is hazard intensity measure; im is a particular value of IM; EDP is the engineering demand parameter; LS is the limit state value associated with the EDP being considered; m_R is the median capacity; ξ_R is the logarithmic standard deviation.

For the two limit states defined in Eqs. (6.12) and (6.14), EDP and LS refer to the maximum compressive stresses of the stem σ_{max} and the stem modulus of rupture σ_R for the stem breakage limit state and base bending moment M_{max} and critical overturning moment M_o^{cri} for the uprooting limit state, respectively. 3-s gust wind speed at the height of 10 m is chosen as IM.

In order to avoid performing fragility analysis for every single tree, which will require cost-forbidden computational and modeling efforts, mean fragility is estimated for tree classes grouped according to tree heights. Trees with heights ranging from 7 m to 29 m are divided into 11 classes and each class covers a height range of 2 m. Tree heights within each class follow uniform distributions. Other tree profile parameters such as DBH, crown height, and crown diameter are determined with the developed allometric equations. For each tree class of a tree species, Monte Carlo simulation is used to generate 10,000 random samples including data related to mechanical properties, wind load, and tree profile according to their statistics in Table 6.2 and 6.3. Each sample builds a tree mechanistic model under a given wind condition, and then the simulation results are checked against the two limit state functions, respectively. With the simulation results from all generated samples, fragility curves for stem breakage and uprooting can be obtained. Fig. 6.3 shows the flowchart of developing the fragility curves of the trees subjected to winds.

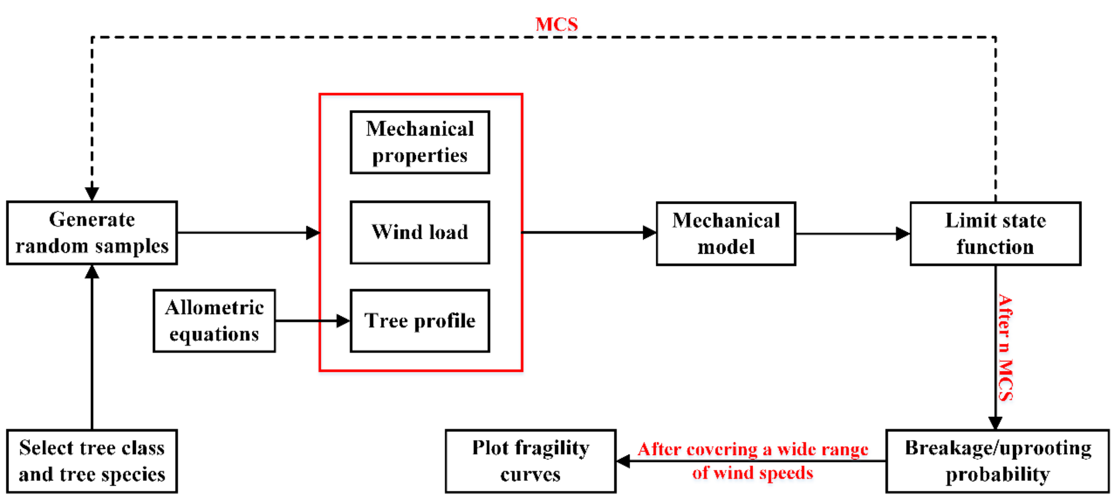

Figure 6.3 Flowchart of generating fragility curves of trees

Fig. 6.4 illustrates the stem breakage fragility for three tree species. Five selected tree classes with different tree heights, namely 9 - 11 m, 13 - 15 m, 17 - 19 m, 21 - 23 m, and 25 - 27 m, are considered. The calculated fragility results, which are represented by the black circles in Fig. 6.4, are compared with lognormal cumulative distributions obtained by best-fit analysis. It is seen that lognormal distribution can capture the general trend of fragilities obtained by the Monte Carlo simulation. As might be expected, the vulnerability of stem breakage increases with the increase of tree heights for all three tree species. Generally, Green ash is less vulnerable to stem breakage than the other two tree species, due to its higher modulus of rupture.

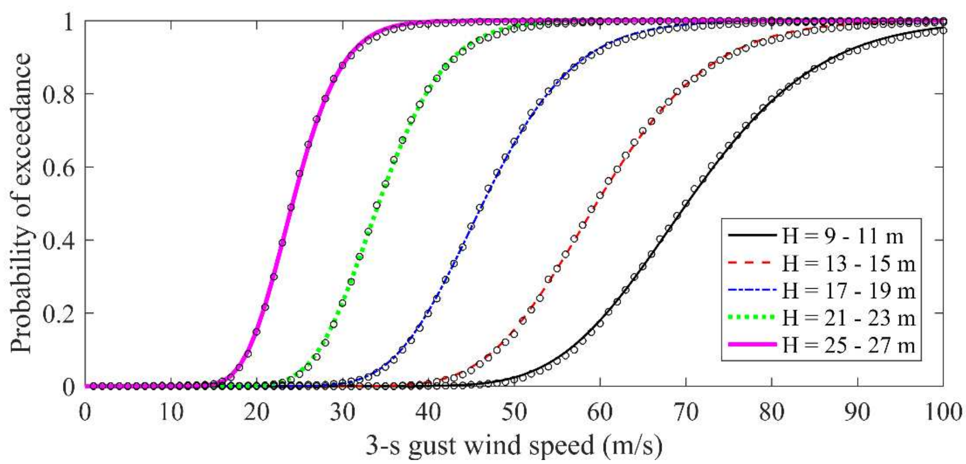

(a) American basswood

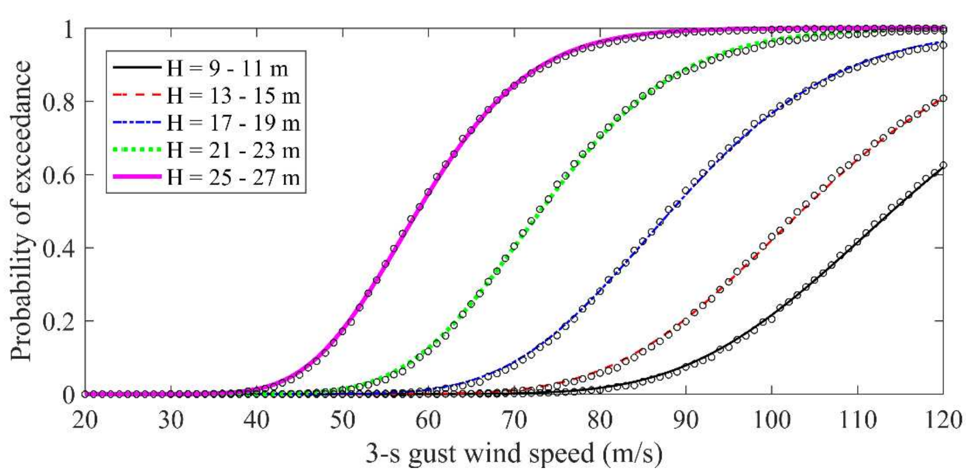

(b) Green ash

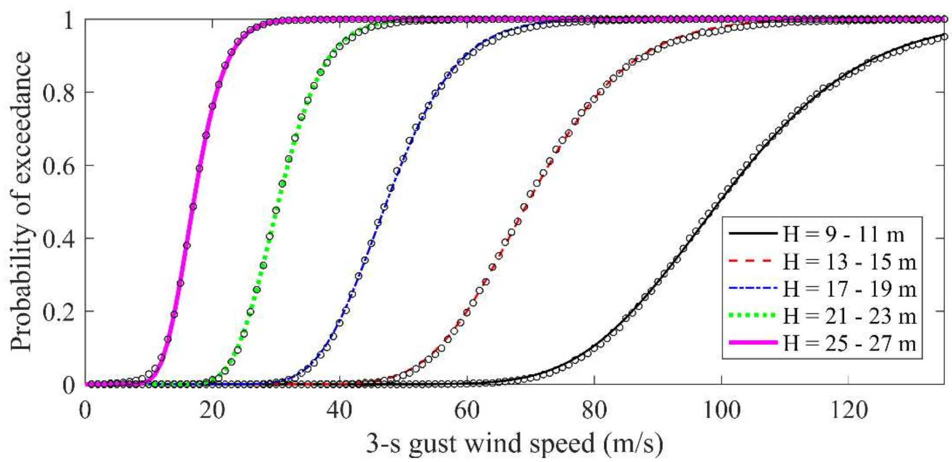

(c) Pondarosa pine

Figure 6.4 Stem breakage fragility for three tree species

Fig. 6.5 presents uprooting fragility curves for three tree species. Unlike American basswood and Ponderosa pine, uprooting fragility curves of Green ash show decreasing vulnerability with the increase of tree heights. According to the uprooting limit state defined in Eq. (6.14), stem weight contributes to both the demand and capacity. It is likely that the contribution to the capacity outweighs that to the demand when the tree height for Green ash increases. Ponderosa pine is less vulnerable than the other two tree species, due to its higher resistive moment. Meanwhile, when the tree height is larger than 17 m, the fragility curves of different classes are very close, indicating that the effect of tree height on the uprooting fragility is insignificant.

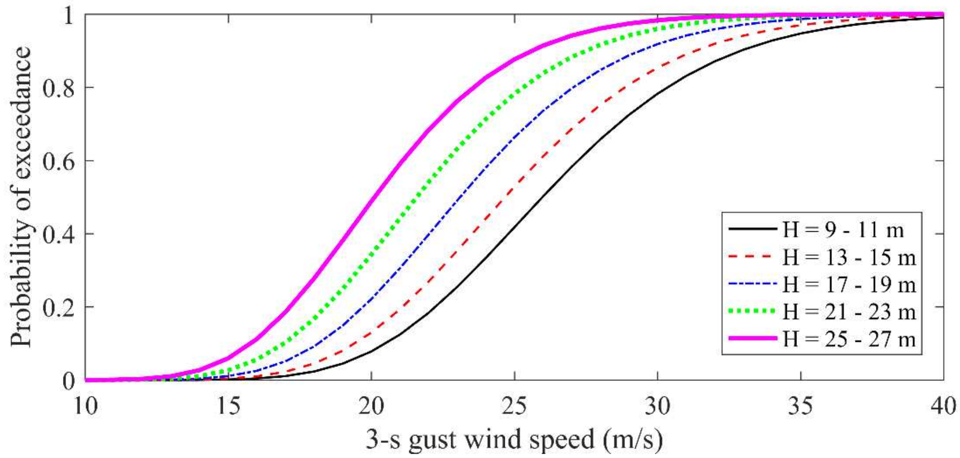

(a) American basswood

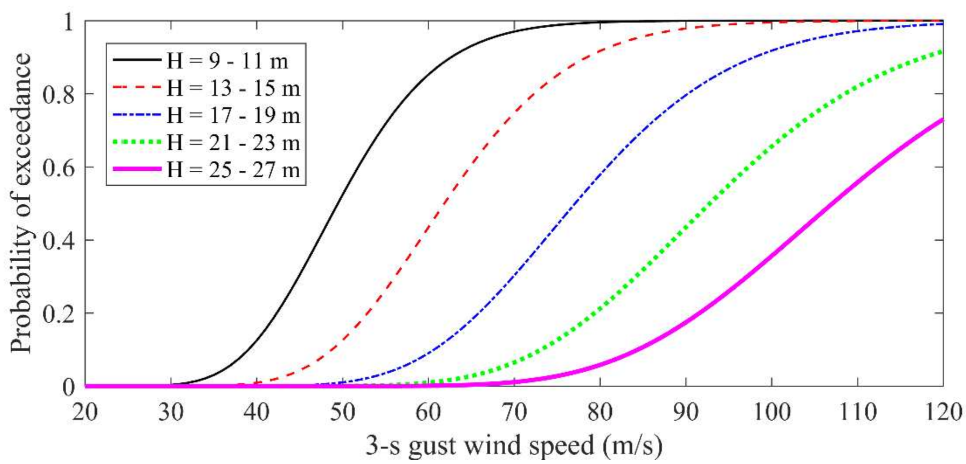

(b) Green ash

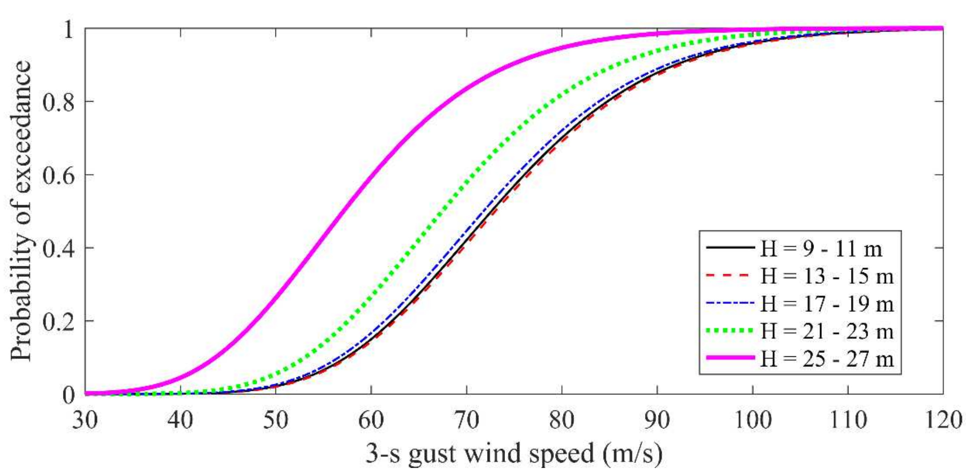

(c) Pondarosa pine

Figure 6.5 Uprooting fragility curves for three tree species

Windthrow includes stem breakage and uprooting. If at least one of the two failure modes occur, windthrow is deemed to occur. The windthrow fragility of a tree can be derived by assembling fragility of two failure modes. Fig. 6.6 shows the windthrow fragility curves for the three tree species. It is found that windthrow of American basswood is dominated by uprooting failure, while windthrow of Ponderosa pine is mainly dominated by the stem breakage failure except for those trees with heights below 11 m. The windthrow probabilities of American basswood and Ponderosa pine increase with the increase of tree height. For Green ash, the fragility curves of different tree classes don't exhibit a clear trend with tree heights. By comparing Fig. 6.6(b) with Figs. 6.4(b) and 6.5(b), it is found that uprooting dominates when tree height ranges from 9 to 19 m, whereas stem breakage dominates when tree height ranges from 21 to 27 m. Generally, the results show that American basswood is most vulnerable to wind, while Green ash is least vulnerable to wind among the three tree species. This is consistent with previous research findings regarding the wind resistance classification for different tree species by Duryea and Kampf (2007): American basswood and Ponderosa pine are considered to have the least and medium-low wind resistance, respectively, while Green ash have a medium-high wind resistance.

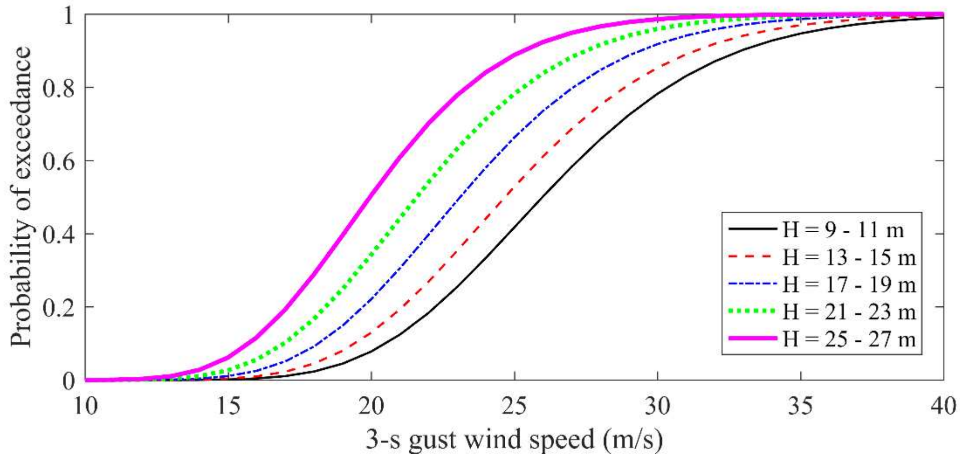

(a) American basswood

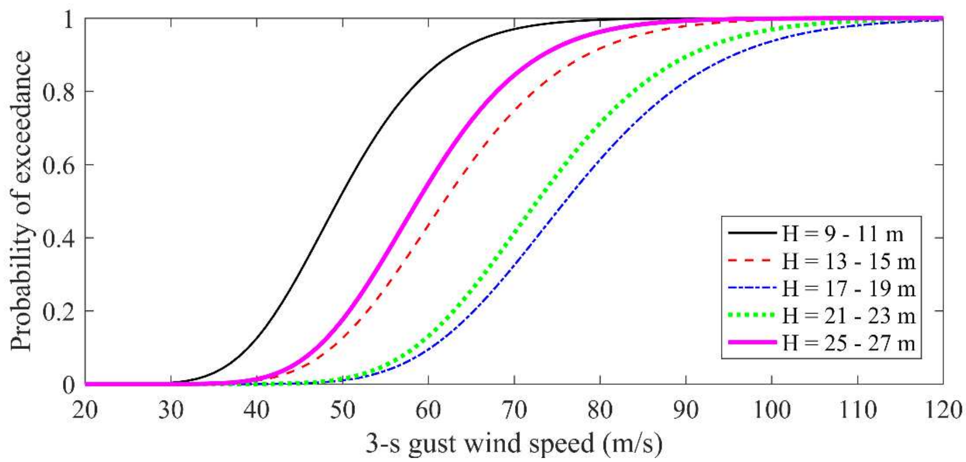

(b) Green ash

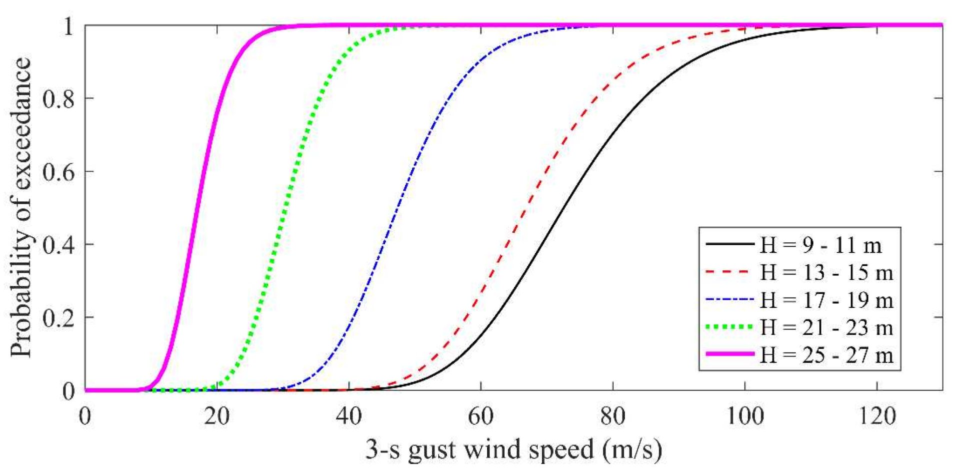

(c) Pondarosa pine

Figure 6.6 Windthrow fragility curves for three tree species

6.3 Probabilistic methodology of modeling disrupted infrastructure due to fallen trees

6.3.1 Probabilistic model of infrastructure disruption

The tree fragility curves developed in the previous section can be used to study the disruption of various infrastructure systems (e.g. transportation system, electrical transmission system, water pipe systems and building system) in urban areas subjected to extreme winds. A probabilistic framework is proposed to estimate the probability of infrastructure disruption due to downed trees. The flowchart of the proposed framework is shown in Fig. 6.7. Under a certain wind condition, the probability of breakage/uprooting of a tree adjacent to an infrastructure can be developed based on the windthrow fragility curves of trees. It should be noted that the windthrow mode of a tree under a given wind speed is determined by the larger one between the probabilities of stem breakage and uprooting. If the probability of stem breakage is higher than that of uprooting, stem breakage will occur first; otherwise, uprooting will occur before breakage. Based on the damage mode of the tree, the infrastructure disruption status due to the fallen tree is determined accordingly based on some predefined criteria. After the probabilities of windthrow of all the trees along the infrastructure and the corresponding disruption scenarios of the infrastructure under a given wind condition are obtained, Monte Carlo simulations are used to generate a large number of possible disrupted scenarios of the infrastructure by considering possible windthrow risks of all the trees. Finally, the probability of the infrastructure disruption can be obtained according to the Monte Carlo simulation results.

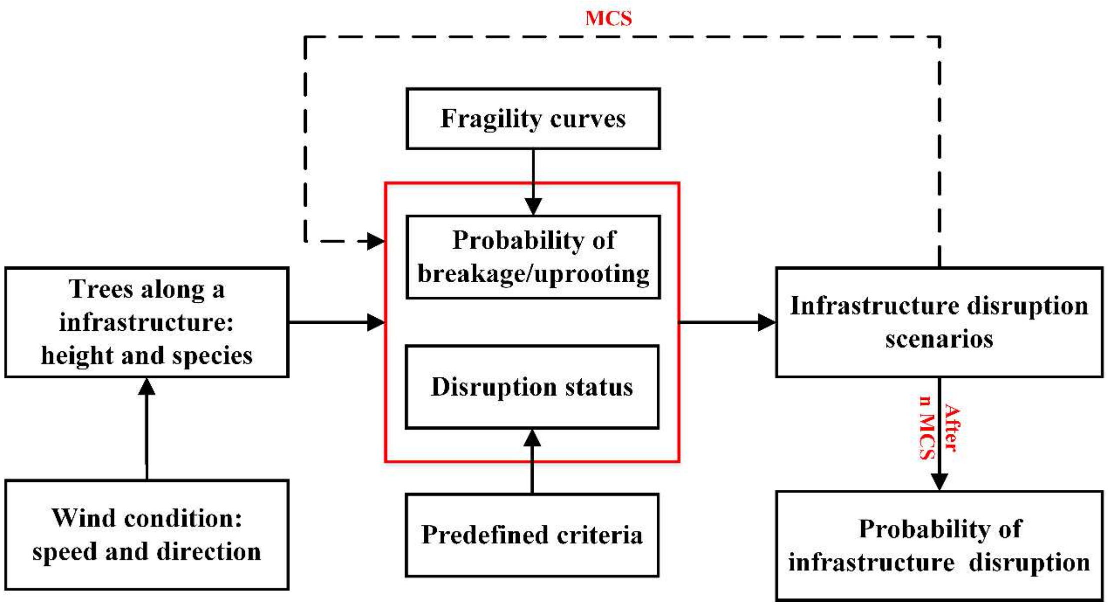

Figure 6.7 Flowchart of the probabilistic framework to estimate probability of infrastructure disruption

Road blockage and overhead powerline failure induced by fallen trees are demonstrated in detail with the proposed framework, and the corresponding schematic diagrams are shown in Figs. 6.8 and 6.9. As shown in Fig. 6.8, assuming 2.5 m is the minimum open width across the road to enable typical vehicles to pass, a road is deemed being fully blocked by an uprooted or broken tree as long as at least one of Eqs. (6.16) and (6.17) is satisfied:

$$\text{Road blockage by an uprooted tree: } Hsin(\theta) > D + L - 2.5 \tag{6.16}$$

$$\text{Road blockage by a broken tree: } H_b sin(\theta) > D + L - 2.5 \tag{6.17}$$

where H is the tree height (m); H_b is the length of the broken part of the tree (m), which can be obtained from the mechanical model; θ is the angle between the wind direction and the road direction (°); D is the distance between the tree and the road (m); L is the road width (m).

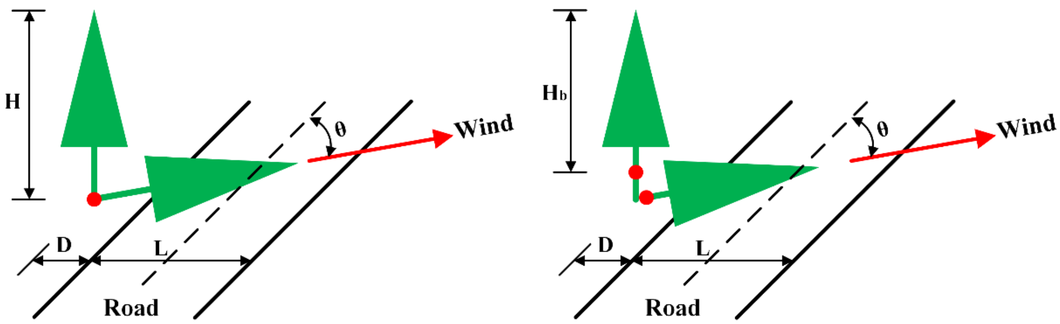

(a) Uprooting (b) Breakage

Figure 6.8 Schematic diagrams of road blockage induced by fallen trees

As shown in Fig. 6.9, if Eq. (6.18) or Eq. (6.19) is satisfied, a powerline failure will occur due to the disruption caused by an uprooted or broken tree.

Powerline failure by an uprooted tree: $H > H' = \sqrt{h^2 + d'}$ (6.18)

Powerline failure by a broken tree: $H_b > H' = \sqrt{h'^2 + d'}$ (6.19)

where h is the height of the powerline (m); $d' = d/sin(\theta)$, d is the distance between the tree and the powerline (m); $h' = h - (H - H_b)$.

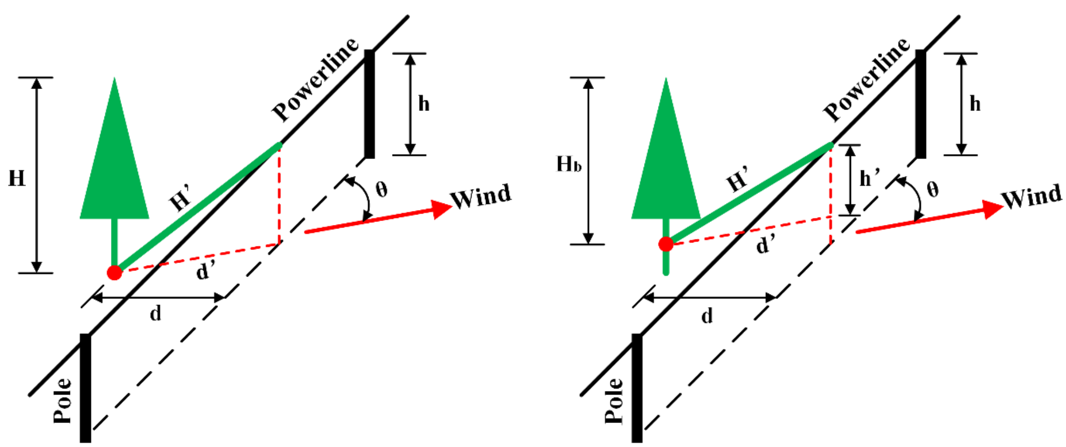

(a) Uprooting (b) Breakage

Figure 6.9 Schematic diagrams of powerline disruption induced by fallen trees

6.3.2 Transportation network analysis in emergency response stage

During and after an extreme wind event, first responders, rescue teams and emergency vehicles often need to be dispatched to the impacted area through accessible (unblocked) routes as soon as possible. People are interested in knowing not only whether a specific origin-destination (OD) pair is connected, but also whether emergency vehicles can arrive at the destination within expected time frame. Therefore, it is crucial to predict both the connectivity and travel time reliability of potentially disrupted transportation systems due to fallen trees during and following a major wind storm. Such information, which is very different from that in normal conditions and provided by popular map navigation services, will be very helpful for emergency responders as well as general passengers to identify the optimal travel routes and predicting actual travel time following an extreme wind event. The matrix-based system reliability (MSR) method proposed by Kang et al. (2008) is found to be a convenient and efficient tool to compute the connectivity reliability and other quantitative performance measures (e.g. network flow capacity) of a complex system, which will be adopted in the following study.

6.3.2.1 Connectivity analysis

For the MSR method, the sample space of component events with d_i distinct states, $i = 1, \dots, n$, is divided into $m = \prod_{i=1}^{n} d_i$ mutually exclusive and collectively exhaustive (MECE) events. The probability of a general system event can be obtained with the following formulation:

$$P(E_{sys}) = P_{sys} = \mathbf{c}^{\mathbf{T}}\mathbf{P} \tag{6.20}$$

where E_{sys} is a general system event; P_{sys} is the probability of the system event; $\mathbf{c}$ is the event vector whose element is 1 if its corresponding MECE event is included in E_{sys}, and 0 otherwise; $\mathbf{P}$ is the probability vector that contains the probabilities of all the MECE events. In this study each component in the infrastructure system (e.g. powerline, road link) has two states due to fallen trees: disrupted and undisrupted, so there will be a total of 2^n MECE events. Since the disruption probability of each component of the infrastructure system can be calculated with the probabilistic framework in Section 6.3.1, the probability vector $\mathbf{P}$ can be easily constructed with simple matrix operations. Then the event vector $\mathbf{c}$ can also be identified separately. Finally, the disconnection probability between two areas can be computed by Eq. (6.20) with the identified $\mathbf{c}$ and $\mathbf{P}$ vectors. Full details of MSR methods can be found in the reference (Kang et al. 2008).

6.3.2.2 Travel time reliability analysis

For a specific wind scenario, we perform shortest path analysis for each of the m disruption cases and find the shortest time for an OD pair. For each of the distinct values obtained from the shortest path analysis, t, the probability mass function (PMF) and cumulative distribution function (CDF) of the shortest time T for an OD pair can be expressed by Eqs. (6.21) and (6.22), respectively.

$$P_T(t) = P(T = t) = \sum_{i:t_i=t}^{m} p_i \tag{6.21}$$

$$F_T(t) = P(T \leq t) = \sum_{i:t_i \leq t}^{m} p_i \tag{6.22}$$

where t_i is the shortest OD time for the ith disruption case, p_i is the ith element in the probability vector $\mathbf{P}$. Since it is now focused on emergency response stage shortly following a windstorm when the traffic demands on the roads are very low, free flow travel time for each passable link is used in the shortest path analysis. For the convenience of presenting the results, a large travel time value, which is 10 times of the free flow time on the link, is assigned to a blocked link in the shortest path analysis. Thus, a large OD time instead of an infinite value will be obtained for a disconnected case. Once the CDF is determined, the travel time reliability, R, which is the probability that the OD time does not exceed an acceptable threshold level tt, can be obtained as

$$R(T \leq tt) = F_T(tt) \tag{6.23}$$

6.3.3 Demonstrative study

Downslope windstorms usually occur several times each year along Colorado's Front Range. Winds of 30 to 50 m/s are commonly observed. One severe downslope windstorm event occurred on July 3rd, 1993 in Fort Collins, Colorado, during which wind gusts reached 40 m/s, causing extensive tree and roof damage (Cotton et al. 1995). Given the potential risk due to windthrow on the infrastructures and the availability of data, city of Fort Collins in Colorado is selected as the demonstrative area in this study. The proposed probabilistic framework which considers the developed fragility curves of urban trees is demonstrated through an application to a portion of the transportation network and powerline system in Fort Collins (Fig. 6.10). The transportation network consists of 9 nodes (solid circles) and 24 links (solid lines). A residential area (dashed circle with a letter "R") is located close to node 7, and there is a hospital (dashed circle with a letter "H") near node 3. The residential area and the hospital are connected with nearby nodes by subjunctive links (dashed lines), which are assumed to be not affected by fallen trees due to the lack of large roadside trees along these secondary roads. In addition, there is an overhead powerline system between node 4 and node 6, which consists of two parts: P1 and P2. P1 is located along link 5, and P2 is located along link 8.

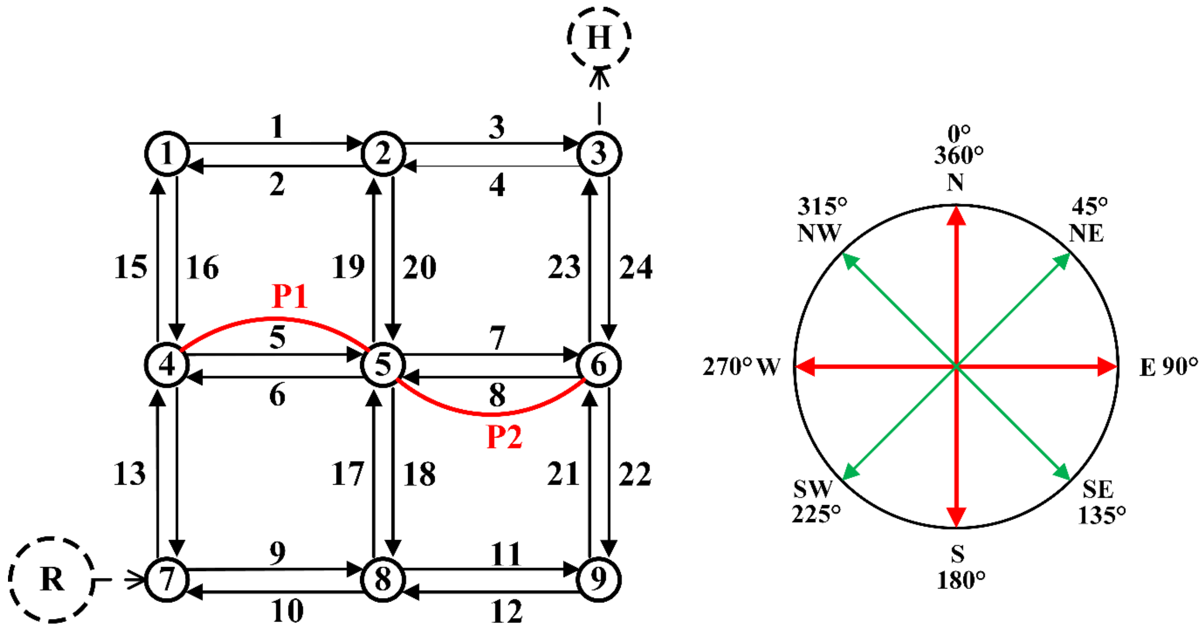

Figure 6.10 An abstracted transportation network and powerline system in City of Fort Collins

Three popular tree species in the city of Fort Collins are considered in this demonstration. Information of these trees along the links of the transportation network are collected based on Google Earth, mainly including tree heights and tree positions. There are totally 418 trees in this network selected from the city of Fort Collins, with the heights ranging from 8 m to 28 m and the height of the powerline is found to be 12m.

6.3.3.1 Powerline disruption

The disruptions (failures) of the overhead powerline system under different wind conditions are investigated. For the overhead powerline system with 2 parts (P1 and P2) as shown in Fig. 6.10, disruptions will occur if at least one part is hit by at least one fallen tree. Following the proposed framework in Section 6.3.1, the failure probability of the powerline system under different wind conditions are obtained and plotted in Fig. 6.11. Three unfavorable wind directions, α = 180°, 240° and 360°, are investigated considering that the powerline system is along the EW direction. As expected, the failure probability increases with the increase of wind speed. It is also found that south winds (α = 180°) are the most unfavorable events to the powerline system while north winds (α = 360°) are the least. Therefore, south winds control the powerline performance and this is because the trees along powerline P2 are more vulnerable to winds than those along powerline P1. To reduce the failure risk of the powerline system during an extreme event in a community, it is advised that the city should pay more attention to vulnerable trees along powerline P2.

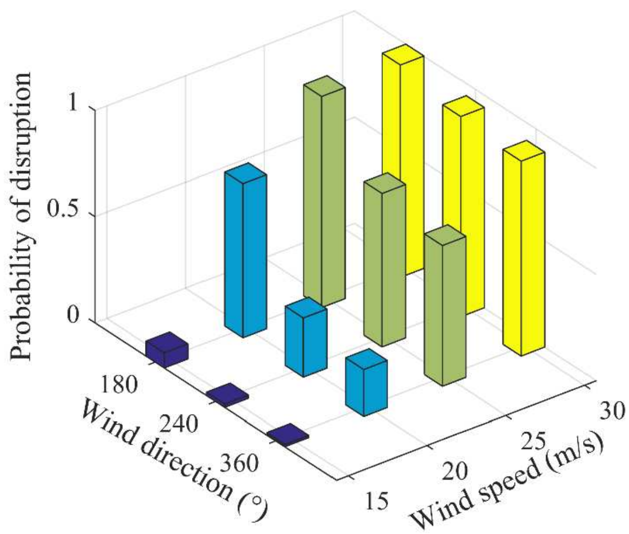

Figure 6.11 Probability of failure of powerline under different wind conditions

6.3.3.2 Road closure

Compared to the powerline system, the transportation system is more complicated given a much higher number of roads and different road orientations. Following the proposed framework in Section 6.3.1, the road closure probability of some selected links is obtained and plotted in Fig. 6.12. Firstly, the road closure probability of 4 links under winds with different speeds but at the same direction ($\alpha = 45°$) is shown in Fig. 6.12(a). As shown in Fig. 6.12(a), the road closure probability increases with the increase of wind speeds for those links. Depending on the species, size and distribution of adjacent trees, some links are more vulnerable to winds than others, while some links have very low probability of being blocked. For example, it is found in Fig. 6.12(a) that Link 7 and 20 have higher closure probability than Link 9 and 22 under same wind direction and speed. Then, road closure probability of the four links under winds with different directions but the same speed (U = 20 m/s) is shown in Fig. 6.12(b), from which it is found that the closure probability of links is sensitive to wind direction.

As shown in Fig. 6.12(b), for a specific link, closure probability varies with different wind directions. We further find that the road closure probability is influenced by the angle between the wind direction and the link orientation. When the wind direction is perpendicular/parallel to the link orientation, the road closure probability is high/low respectively, because a fallen tree will cover a large/small road width in this situation. For example, as shown in Fig. 6.12(b), closure probability of Link 6 and 8 in the EW direction is zero under west winds (α = 270°) but is the highest under south winds (α = 180°) among the four directions. Similarly, the closure probabilities of Link 13 and 21 in the NS direction under south winds (α = 180°) are zero, but become the highest under west winds (α = 270°) among all four directions. Therefore, it is recommended that the city should pay more attention to the vulnerable trees along links that are nearly perpendicular to the prevailing wind directions in windy seasons, including applying some preventive measures.

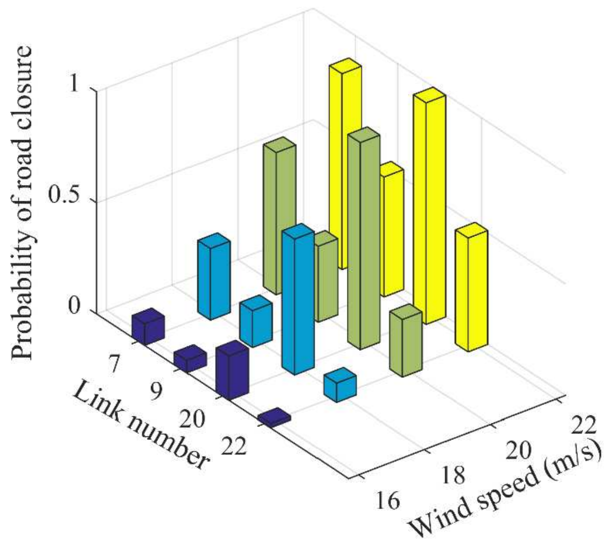

(a) Different wind speeds

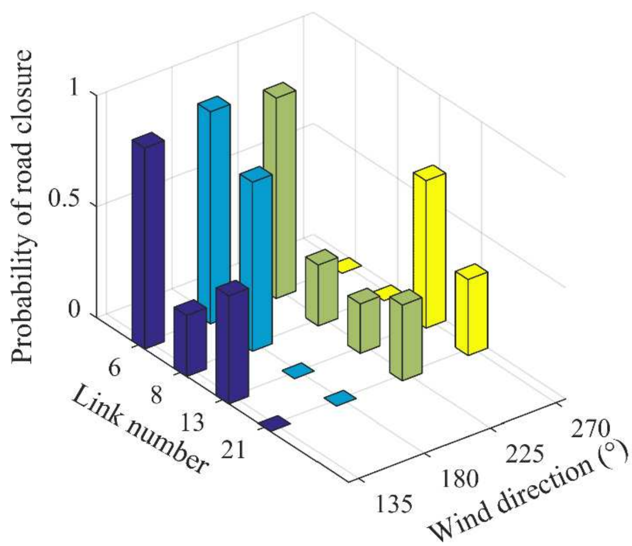

(b) Different wind directions

Figure 6.12 Probability of road closure under different wind conditions

6.3.3.3 Transportation network performance

It is of interest for the decision-makers to know the disconnection probability and travel time reliability between the studied residential area and some specific critical infrastructures in the transportation network, such as the hospital, during a forthcoming wind event. The MSR method introduced in Section 6.3.2.1 is employed to conduct the connectivity analysis of the prototype traffic network for demonstration. After the event vector and probability vector of disconnection between the studied residential area and the hospital are all identified, the disconnection probability of the specific OD pair can be obtained through Eq. (6.20). The probabilities of disconnections between the residential area and the hospital under different wind conditions are plotted in Fig. 6.13.

According to the simulation results, disconnections occur between the OD pair (i.e. the residential area and hospital) under wind directions ranging from -60° (300°) to 45°, mainly around the north direction (Fig. 6.13). Additionally, it is found in Fig. 6.13 that north winds cause higher disconnection probability than other winds. This indicates that the trees along the links that are easier to be impacted by north winds (α = 360°), such as Link 1, 3, 5, 7, 9 and 11, may pose higher risks of blocking these links and disconnecting the residential area and the hospital than the rest trees. With this information, the decision-makers may apply some preventive measures before wind hazards, such as identifying the critical and vulnerable trees, which can be strengthened or trimmed, to reduce the windthrow risk and in turn disconnection probability of the traffic network following the particular wind event. In the meantime, they may plan out some optimal routes by avoiding those vulnerable links for post-event emergency response, such as police, fire, medical service and emergency repair etc.

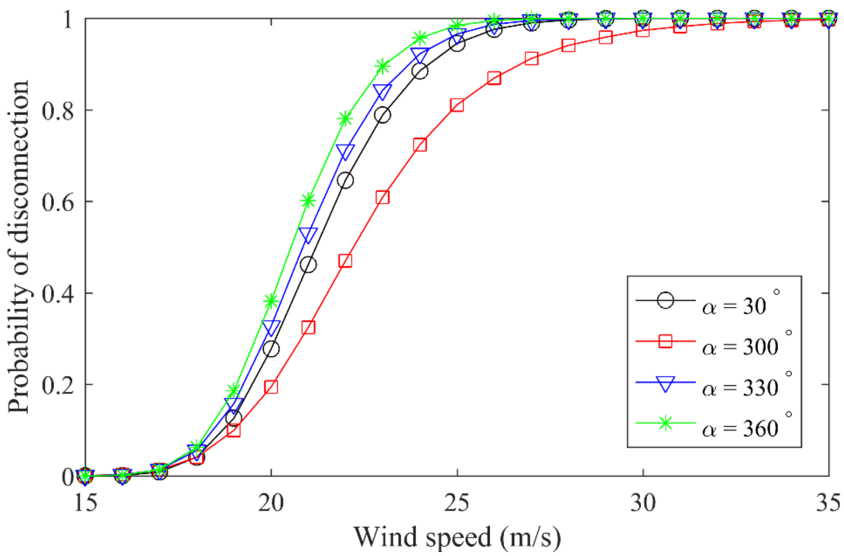

Figure 6.13 Probability of disconnection of the OD pair

Compared to connectivity, travel time reliability, i.e. the probability that a trip between a given OD pair can be successfully made within a specified interval of time, can provide more useful information for the travelers. We then conduct the travel time reliability analysis for the OD pair between the residential area and the hospital with the MSR method introduced in Section 6.3.2.2.

Firstly, the PMF of the OD travel time under winds with direction α = 30° and speed U = 20 m/s is obtained with Eq. (6.21) and shown in Fig. 6.14. It is found that the minimum travel time is equal to the shortest OD travel time under normal conditions tt_0 = 6.03 min, and the corresponding PMF value is 0.435. This indicates that there is a 43.5% chance that the shortest OD path between the residential area and the hospital will not be disrupted in this wind event. It needs to be noted that very large values of travel time (t $\geq$ 19.53 min) in Fig. 6.14 indicates that the all paths between the residential area and the hospital are blocked, since we assume a large instead of infinity value of travel time for blocked links. When the OD travel time is between 6.03 and 19.53 min, a detour has been taken because one or more links on the shortest path are blocked.

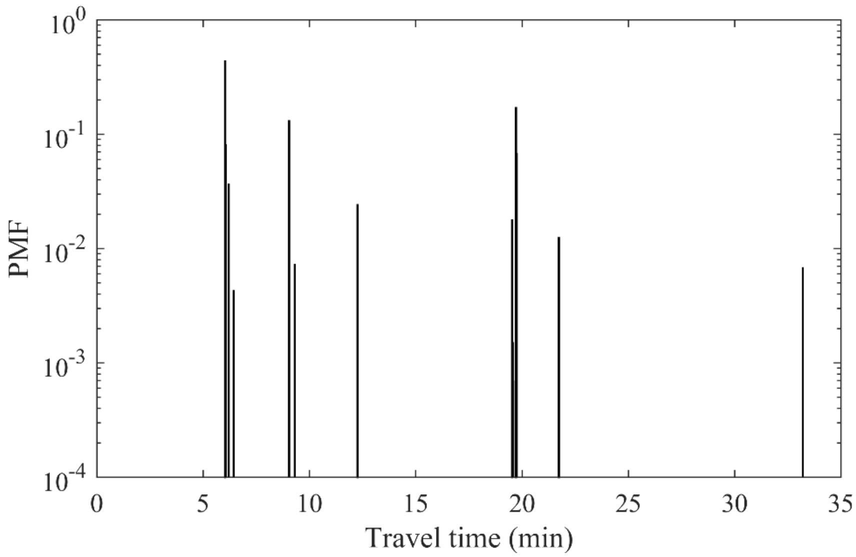

Figure 6.14 The probability mass function of OD travel time

Secondly, the CDFs of the OD travel time under winds with direction α = 30° and speed U = 18, 20 and 22 m/s are obtained with Eq. (6.22) and shown in Fig. 6.15. It can be seen from the figure that the CDF, i.e. the probability that the OD travel time does not exceed a given threshold value and decreases significantly as the wind speed increases. For instance, for the three wind speeds U = 18, 20 and 22 m/s, the probabilities that the OD travel time does not exceed 10 min (vertical line), are 0.955, 0.699, and 0.324, respectively. Meanwhile, the optimal path during a specific wind event, on which the total travel time does not exceed a given time, can be identified by finding the path with short OD travel time and high probability of OD travel time (PMF) based on the derived travel time distribution. It is found that the optimal path under a given time of 10 mins for the three wind scenarios (i.e. α = 30° and U = 18, 20 and 22 m/s) are the same: Link 9 → Link 11 → Link 21 → Link 23, which is also the optimal path under normal conditions. It should be noted that the optimal path is sensitive to wind directions and varies with different wind conditions.

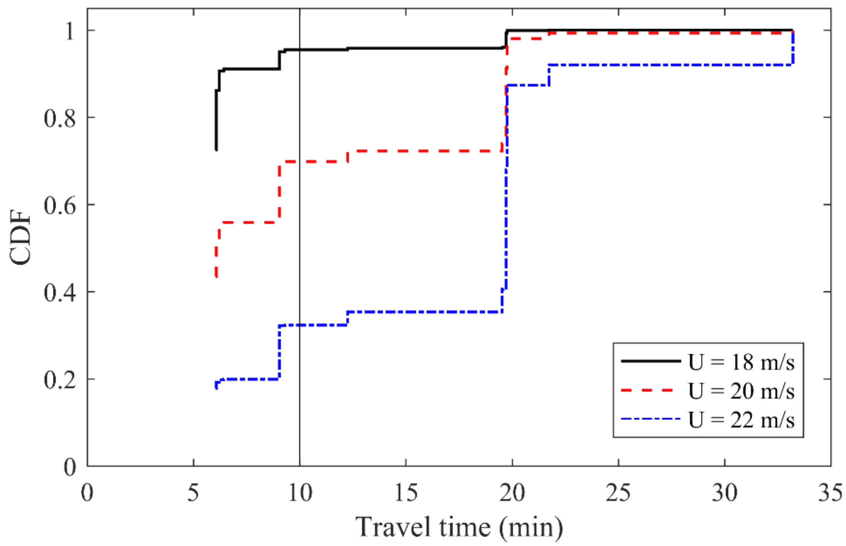

Figure 6.15 The cumulative distribution function of OD travel time

Finally, based on the CDF of OD travel time obtained previously, travel time reliability between the residential area and the hospital for two given wind directions α = 30° and 330° are obtained with Eq. (6.23) and the results are given in Fig. 6.16. Here two acceptable threshold levels are defined: $tt = tt_0$ in level 1and $tt = 2tt_0$ in level 2. From the figure, it is found that travel time reliability decreases greatly with the increase of wind speed. In addition, travel time reliability at level 2 is much higher than that at level 1. This means if a traveler wants to arrive at the hospital from the residential area on time with a higher probability after a strong wind event needs to plan more time for travel. It is also found that travel time reliability under winds direction α = 30° is higher than that under wind direction α = 330°, which is consistent with the connectivity results in Fig. 6.13. Moreover, by comparing Fig. 6.16 with Fig. 6.13, it is found that under same wind conditions, the OD travel time reliability is smaller than the OD connection probability. For example, for a given wind scenario α = 30° and U = 20 m/s, the connection probability is 0.723, while the travel time reliability is 0.435 at level 1 and 0.699 at level 2. This indicates that the travel time reliability will be equal to the connection probability when the acceptable travel time is very large.

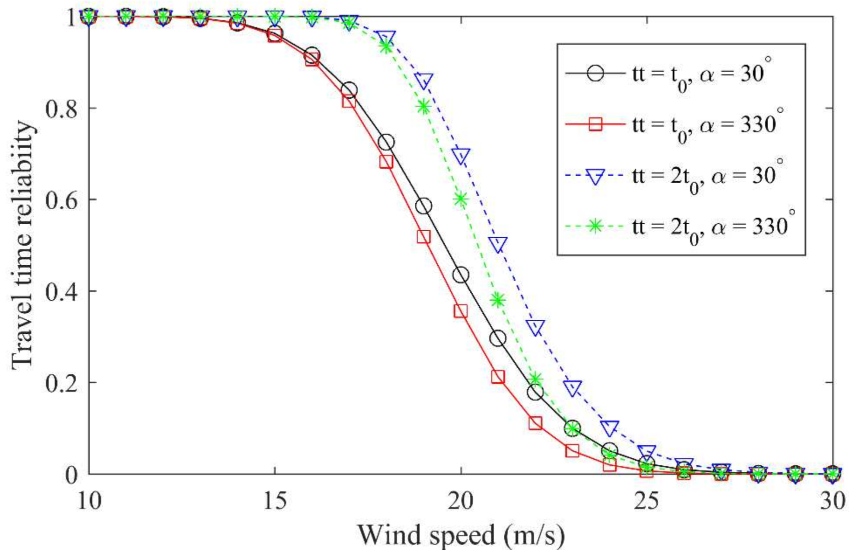

Figure 6.16 Travel time reliability

6.3.3.4 Measures for improving infrastructure performance

Removal of all vulnerable trees threatening infrastructures is neither desirable nor feasible. Crown thinning (CT) is a common measure to reduce the windthrow likelihood by reducing crown weight and wind loads acting on the crown. Usually the extent of thinning in a year does not exceed 25% of the crown of a tree. In this study, the measure of crown thinning is investigated in terms of its effect on the infrastructure performance, where 25% of crown is removed for identified dangerous roadside trees in the transportation network of Fort Collins. We assume the crown density and effective crown area will be reduced by 25% and other tree parameters will keep the same after crown thinning. As a result, there will be a 25% reduction in both crown weight and wind loads acting on the crown. Furthermore, the windthrow fragility of trees will be affected by the reduced crown weight and wind loads.

Fig. 6.17 gives the breakage and uprooting fragility curves for American basswood with a height of 15-17 m before and after crown thinning. It is found that both the breakage and uprooting fragility can be improved significantly after crown thinning. Moreover, the effects of crown thinning on the infrastructure performance, such as powerline disruption, road closure, OD connectivity and OD travel time reliability, are investigated.

Fig. 6.18 shows the disruption probability of powerline and road closure probability of link 8 under north winds (α = 360°). Fig. 6.19 shows the disconnection probability and travel time reliability at level 2 between the hospital and the residential area under wind direction α = 300° before and after crown thinning. It is observed from Figs. 6.18 and 6.19 that the network performance is greatly improved after crown thinning, as reflected by the reduced powerline disruption probability, decreased road closure probability, reduced OD disconnection probability and increased OD travel time reliability.

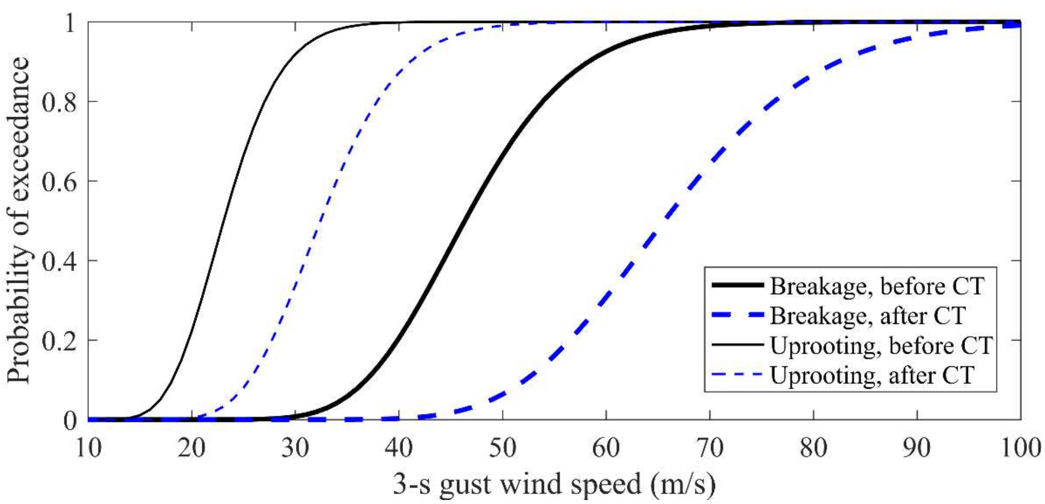

Figure 6.17 Windthrow fragility curves for basswood before and after crown thinning

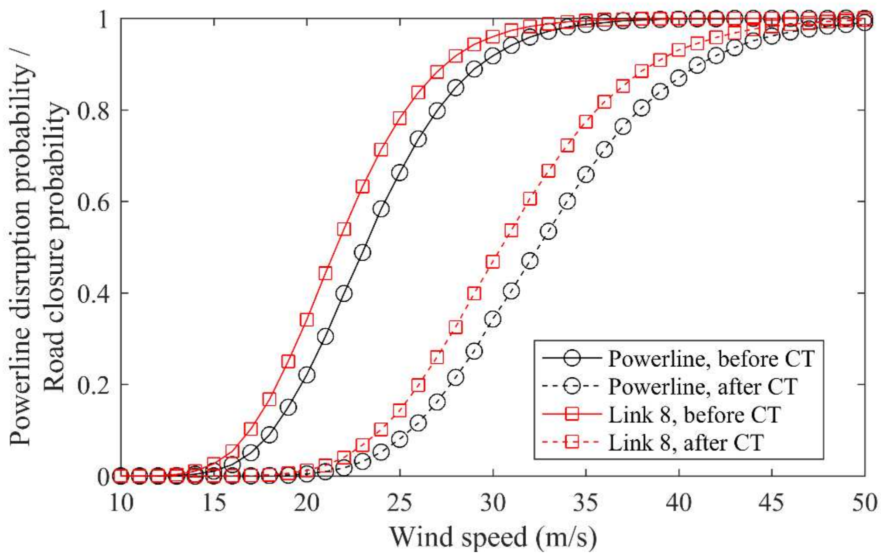

Figure 6.18 Powerline disruption probability and road closure probability before and after crown thinning

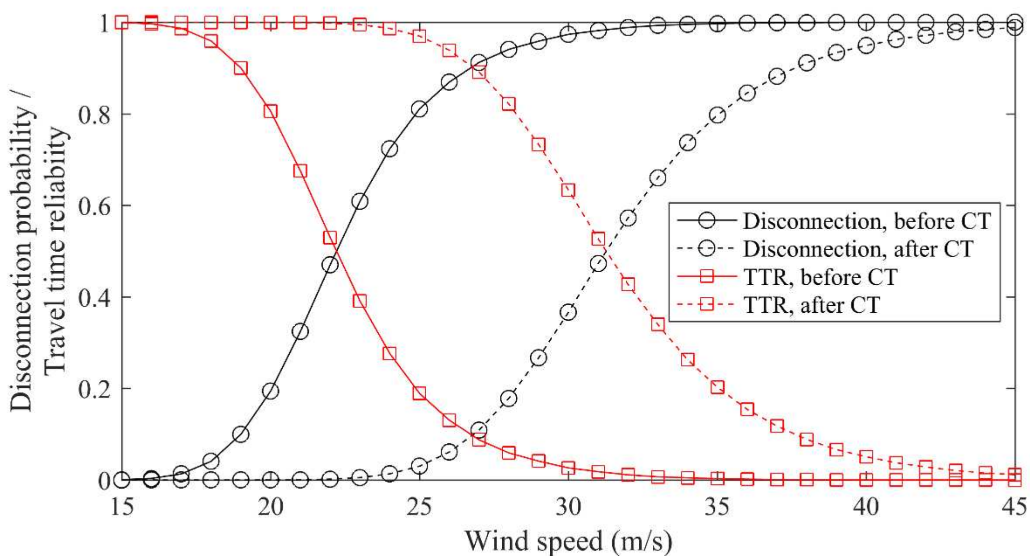

Figure 6.19 Disconnection probability and travel time reliability before and after crown thinning

6.4 Conclusions

This study proposed a probabilistic methodology to model the disrupted infrastructures due to fallen trees during wind events. Firstly, windthrow fragility analyses of typical urban trees under extreme winds were developed with considerations of the uncertainties of the wind loads and mechanical properties of trees. FEM-based mechanistic tree model was developed to compute the tree response subjected to wind loads, based on which both uprooting and stem breakage fragility curves of three tree species with different height classes were generated through Monte Carlo simulations. Secondly, the probabilistic impact on a powerline system and a transportation network is derived with the proposed framework and the MSR method by adopting the developed fragility curves. The proposed methodology was numerically demonstrated in a prototype community in the city of Fort Collins with following findings:

(1) Windthrow fragility of trees is species-dependent, which is strongly related to the wind characteristics and mechanical properties of particular tree species. Generally, higher stem modulus of rupture leads to lower stem breakage vulnerability, while higher critical overturning moment leads to lower uprooting vulnerability.

(2) Because species, sizes and distributions of trees vary considerably at different locations, the powerline disruption probability, road closure probability, OD disconnection probability and travel time reliability under strong winds were found to be sensitive to wind directions. To reduce the wind risk, the city should pay attention to the vulnerable trees along powerlines and links that are nearly perpendicular to prevailing wind directions.

(3) Crown thinning of trees was found to be an effective measure to improve infrastructure performance by reducing the probability of powerline disruption, road closure and OD disconnection, and increasing the OD travel time reliability.

CHAPTER 7 SUMMARY OF THE DISSERTATION AND FUTURE STUDIES

7.1 Summary and conclusions

The contributions and findings of this dissertation are summarized in the following, which correspond to Chapter 2 to 6:

(1) A new CA-based traffic flow simulation framework for hazardous driving environments is proposed, which considers more reasonable vehicle properties, anticipation effect, and different driving behaviors among drivers. This framework can provide traffic flow simulation under both normal traffic and hazardous (panic) traffic conditions. Compared to the proposed model, the mean flow rate is overestimated if limited deceleration is not incorporated, while underestimated if anticipation effect is not incorporated. Compared to the traffic under normal driving conditions, hazardous driving conditions can increase the mean traffic velocity when the occupancy is low. The standard deviation of the vehicle velocity is larger in the panic flow than the corresponding value in the normal flow. There are more congestion clusters distributed on the bridge under panic driving conditions than those under normal driving conditions, leading increased local concentrations of live loads on the bridge under high-occupancy traffic. Panic driving behavior is found to lead to larger extreme values and fluctuation of vehicle driving speeds and may significantly influence the extreme dynamic response of vehicles.

(2) A new methodology was proposed to study the traffic performance of degraded road links being partially blocked following extreme events. In the numerical demonstrative study, the fundamental diagrams, time-space diagrams and lane-changing frequency were developed to investigate the traffic

flow characteristics and traffic dynamics under various scenarios. The impact of truck proportion, blockage configuration and traffic control were also studied. Four regions are found in the fundamental diagrams of disrupted traffic with single extended partial blockage (scenario A), namely, unsaturated traffic, transition traffic, saturated traffic, and oversaturated traffic. For scenario A, the truck proportion has a negative effect on the flow and velocity; traffic control of buses and trucks can improve the traffic safety in terms of lower speed variation, although the traffic flow efficiency is reduced. There are three regions in the fundamental diagrams, namely, unsaturated traffic, saturated traffic, and oversaturated traffic for the scenario with scattered multiple small partial blockages (scenario B). For scenario B, as the distance between two partial blockages increases, the traffic flow is improved by more evenly distributed lane change; traffic control in the accident area could improve traffic safety but reduce the flow, and an appropriate speed limit in the accident scene is deemed necessary.

(3) By overcoming the limitations of previous studies, this study proposed a methodology for developing travel time functions of PBR in urban areas based on microscopic traffic simulation. Firstly, an improved CA model was proposed for heterogeneous traffic flow on partially blocked arterial roads by extending the two-lane SD model. With the proposed model, two types of unrealistic deceleration behaviors in most existing CA models can be avoided. Meanwhile, driver's behaviors during traffic signal change intervals were realistically replicated by determining the vehicle status based on the vehicle's distance to the intersection, driving speed and stopping probability. Secondly, the proposed model was calibrated and validated with the collected field traffic data in both macroscopic and microscopic scales. The validation results show that the proposed model can simulate the disrupted traffic flow with acceptable accuracy. Finally, the traffic data under various scenarios with different

traffic volumes, truck ratios and blockage ratio were generated through microscopic simulation experiments. The experiment results demonstrate that both blockage ratio and truck ratio have significant influence on the travel time. A continuous traffic time function was proposed for the disrupted traffic flow to capture the effect of the blockage ratio and truck ratio on the travel time. Its parameters were then estimated through a nonlinear regression analysis with the generated traffic data. Comparison results show that the developed travel time functions can provide more flexible and accurate predictions of travel time for PBR than the standard BPR function.

(4) An integrated framework was proposed to evaluate the overall safety performance of vehicles in realistic stochastic traffic passing through highway infrastructure systems. Vehicle accident vulnerability was introduced as an overall safety index for the whole traffic, which may be used as an important resilience indicator for future resilience studies involving traffic safety. The proposed framework was applied to a bridge-roadway system for demonstration purposes. It was found that the proposed framework could provide rational estimation of the safety performance of traffic flow with findings consistent with existing studies and common observations. The main conclusions from the demonstrative study are summarized as follows. Among the three different road surface conditions, the icy road surface poses the greatest threat to vehicle accidents, whereas the dry road surface poses the least. Compared to vehicles on the bridge and the straight road, those on the curved road are more likely to experience accidents without considering the sheltering effect. Trucks are slightly more likely to experience an accident than vans on dry roads. However, vans have greater accident vulnerability than trucks on snowy and icy roads in general. Among the three types of vehicles, cars have the smallest possibility to experience an accident under dry road surface conditions, whereas they have the largest

possibility to experience an accident under snowy and icy surface conditions. The accident vulnerability of vehicles is influenced by the traffic occupancies in terms of the driving speed of vehicles.

(5) This study proposed a probabilistic methodology to model the disrupted infrastructures due to fallen trees during wind events. Firstly, windthrow fragility analyses of typical urban trees under extreme winds were developed with considerations of the uncertainties of the wind loads and mechanical properties of trees. FEM-based mechanistic tree model was developed to compute the tree response subjected to wind loads, based on which both uprooting and stem breakage fragility curves of three tree species with different height classes were generated through Monte Carlo simulations. Secondly, the probabilistic impact on a powerline system and a transportation network is derived with the proposed framework and the MSR method by adopting the developed fragility curves. The proposed methodology was numerically demonstrated in a prototype community in the city of Fort Collins with following findings. Windthrow fragility of trees is species-dependent, which is strongly related to the wind characteristics and mechanical properties of particular tree species. Generally, higher stem modulus of rupture leads to lower stem breakage vulnerability, while higher critical overturning moment leads to lower uprooting vulnerability. Because species, sizes and distributions of trees vary considerably at different locations, the powerline disruption probability, road closure probability, OD disconnection probability and travel time reliability under strong winds were found to be sensitive to wind directions. To reduce the wind risk, the city should pay attention to the vulnerable trees along powerlines and links that are nearly perpendicular to prevailing wind directions. Crown thinning of trees was found to be an effective measure to improve infrastructure performance by reducing the

probability of powerline disruption, road closure and OD disconnection, and increasing the OD travel time reliability.

7.2 Directions for future research

Some possible improvements and extensions in future based on the current research are discussed in the following.

a) Post-earthquake performance of urban transportation systems

Earthquakes may cause significant damage to buildings and bridges. Debris from damaged buildings and collapsed bridges will cause full or partial road disruption and deteriorate the performance of transportation systems. A framework of earthquake-specific road disruption and its application on the network performance assessment and traffic management can be developed following this study, in which road disruption due to bridge failure and fallen building debris can be considered. Travel time functions of partially blocked roads links are necessary for traffic demand modeling, which can be developed based on the framework proposed in Chapter 4. The accessibility, travel time and planning will be conducted for a prototype community.

b) Impact of tree damage on other infrastructures

Although demonstrated only on overhead powerline and transportation systems in detail, the proposed methodology in Chapter 6 can be extended to the performance assessment of other disrupted infrastructures related to windthrow of trees in wind events, such as underground pipeline systems and buildings, once their potential vulnerability posed by fallen trees being appropriately characterized. In this demonstrative study, three typical urban tree species were studied in terms of fragility curves and the same procedure of conducting tree fragility analysis and disruption modeling can be easily applied to other tree species and communities by considering site-specific tree, wind and network conditions.

c) Microscopic traffic flow simulation of urban transportation networks

Microscopic traffic simulation models in the dissertation are focused on the link level. A microscopic traffic simulation model for urban transportation networks will be developed in future considering its potential application in post-hazard network performance assessment. Macroscopic traffic simulation models (e.g. user equilibrium and system optimal models) are suitable for transportation networks under normal conditions, but not practical for those under hazardous conditions. Firstly, lots of important information are missing in the macroscopic models, such as traffic signals, differences between different vehicles, drivers and pedestrians. This is feasible when simulating traffic under normal conditions, because normal traffic in a network is nearly deterministic and can be modeled in an aggregated way. However, those information may change significantly during and after hazards and cannot be easily incorporated in the macroscopic model. For example, traffic lights may be damaged in an earthquake or a hurricane and lose their function; drivers may change their normal driving behaviors and normal routes. Secondly, macroscopic models can not consider damaged roads (e.g. partially blocked roads (PBR)) directly. The performance of a PBR can be modeled with a travel time function in macroscopic models. However, travel time functions of PBR are not readily available and are very hard to develop due to rare real traffic data and complexity of different disruption scenarios. The above-mentioned shortcomings of macroscopic models can be avoided in the microscopic models, because of their ability of directly simulating traffic signals, individual vehicles and intact or partially blocked roads. Potential application of microscopic network traffic simulation model may include: 1) resilience analysis of transportation networks; (2) identification of critical roads; (3) optimization of evacuation plan after hazards.

REFERENCES

AAA Foundation for Traffic Safety (2009). Aggressive driving: Research update. Washington, DC, http://www.aaafoundation.org/pdf/AggressiveDrivingResearchUpdate2009.pdf.

AASHTO (2004). A policy on geometric design of highways and streets, AASHTO, Washington, D.C.

Adeli, H., and Jiang, X. M. (2003). "Neuro-fuzzy logic model for freeway work zone capacity estimation." J Transp Eng-Asce, 129(5), 484-493.

Ai, X. Q., Cheng, Y. Y., and Peng, Y. B. (2016). "Nonlinear dynamics and failure wind velocity analysis of urban trees." Wind Struct, 22(1), 89-106.

Anastassiadis, A.J. and Argyroudis, S.A. (2007). "Seismic vulnerability analysis in urban systems and road networks. Application to the city of Thessaloniki, Greece." Int. J. of Sus. Dev. Plann., 2 (3), 287-301.

Ancelin, P., Courbaud, B., and Fourcaud, T. Y. (2004). "Development of an individual tree-based mechanical model to predict wind damage within forest stands." Forest Ecol Manag, 203(1-3), 101-121.

Anderson Jr, J. D. (2010). Fundamentals of aerodynamics, Tata McGraw-Hill Education.

Argyroudis, S., Selva, J. and Gehl, P. (2015). "Systemic seismic risk assessment of road Networks considering interactions with the Built Environment." Computer-aided Civil and Infrastructure Engineering, 30, 524-540.

Baker, C. J. (1986). "A Simplified Analysis of Various Types of Wind-Induced Road Vehicle Accidents." J Wind Eng Ind Aerod, 22(1), 69-85.

Baker, C. J. (1987). "Measures to Control Vehicle Movement at Exposed Sites during Windy Periods." J Wind Eng Ind Aerod, 25(2), 151-161.

Baker, C. J. (1991). "Ground Vehicles in High Cross Winds .1. Steady Aerodynamic Forces." J Fluid Struct, 5(1), 69-90.

Baker, C. J. (1994). "The quantification of accident risk for road vehicles in cross winds." J Wind Eng Ind Aerod, 52, 93-107.

Barlovic, R., Santen, L., Schadschneider, A., and Schreckenberg, M. (1998). "Metastable states in cellular automata for traffic flow." Eur Phys J B, 5(3), 793-800.

Batista, M., and Perkovic, M. (2014). "A simple static analysis of moving road vehicle under crosswind." J Wind Eng Ind Aerod, 128, 105-113.

Benjamin, S. C., Johnson, N. F., and Hui, P. M. (1996). "Cellular automata models of traffic flow along a highway containing a junction." J Phys a-Math Gen, 29(12), 3119-3127.

Bham, G. H. (2002). "Comparison of Characteristics and Computational Performance: CarFollowing Versus Cellular Automata Models." TRB 2003 Annual Meeting CD-ROM, Washington, DC, USA

Bham, G. H., and Benekohal, R. F. (2004). "A high fidelity traffic simulation model based on cellular automata and car-following concepts." Transport Res C-Emer, 12(1), 1-32.

Bureau of Public Roads (1964). Traffic assignment manual, U.S. Dept. of Commerce, Urban Planning Division, Washington D.C.

Bureau of Transportation Statistics (BTS) website, U.S. Department of Transportation, www.bts.gov, as downloaded 29 March 2019.

Cai, C. S., and Chen, S. R. (2004). "Framework of vehicle-bridge-wind dynamic analysis." J Wind Eng Ind Aerod, 92(7-8), 579-607.

Calvert, S. C., and Snelder, M. (2015). "A methodology for road traffic resilience analysis and review of related concepts." 6th International Symposium on Transportation Network Reliability (INSTR), Nara, Japan.

Cassidy, M. J., and Han, L. D. (1993). "Proposed Model for Predicting Motorist Delays at 2-Lane Highway Work Zones." J Transp Eng-Asce, 119(1), 27-42.

Chen, F., and Chen, S. R. (2011). "Reliability-based assessment of vehicle safety in adverse driving conditions." Transport Res C-Emer, 19(1), 156-168.

Chen, J. Z., Peng, Z. Y., and Fang, Y. (2014). "Effects of Car Accidents on Three-Lane Traffic Flow." Math Probl Eng, 2014, 413852.

Chen, N., Li, Y. L., Wang, B., Su, Y., and Xiang, H. Y. (2015). "Effects of wind barrier on the safety of vehicles driven on bridges." J Wind Eng Ind Aerod, 143, 113-127.

Chen, S. R., and Cai, C. S. (2004). "Accident assessment of vehicles on long-span bridges in windy environments." J Wind Eng Ind Aerod, 92(12), 991-1024.

Chen, S. R., and Cai, C. S. (2007). "Equivalent wheel load approach for slender cable-stayed bridge fatigue assessment under traffic and wind: Feasibility study." Journal of Bridge Engineering, 12(6), 755-764.

Chen, S. R., and Chen, F. (2010). "Simulation-Based Assessment of Vehicle Safety Behavior under Hazardous Driving Conditions." J Transp Eng-Asce, 136(4), 304-315.

Chen, S. R., and Wu, J. (2010). "Dynamic Performance Simulation of Long-Span Bridge under Combined Loads of Stochastic Traffic and Wind." Journal of Bridge Engineering, 15(3), 219-230.

Chen, S. R., and Wu, J. (2011). "Modeling stochastic live load for long-span bridge based on microscopic traffic flow simulation." Comput Struct, 89(9-10), 813-824.

Chen, S. R., Chen, F. and Wu, J. (2011). "Multi-scale traffic safety and operational performance study of large trucks on mountainous interstate highway." Accident Analysis and Prevention, 43, 535-544.

Chen, Y. B., Feng, M. Q., and Tan, C. A. (2006). "Modeling of traffic excitation for system identification of bridge structures." Comput-Aided Civ Inf, 21(1), 57-66.

Chisolm, E. I., and Matthews, J. C. (2012). "Impact of hurricanes and flooding on buried infrastructure." Leadership and Management in Engineering, 12(3), 151-156.

Chowdhury, D., Wolf, D. E., and Schreckenberg, M. (1997). "Particle hopping models for two-lane traffic with two kinds of vehicles: Effects of lane-changing rules." Physica A, 235(3-4), 417-439.

Ciftci, C., Arwade, S. R., Kane, B., and Brena, S. F. (2014). "Analysis of the probability of failure for open-grown trees during wind storms." Probabilist Eng Mech, 37, 41-50.

Coleman, S. A., and Baker, C. J. (1994). "An Experimental-Study of the Aerodynamic Behavior of High Sided Lorries in Cross Winds." J Wind Eng Ind Aerod, 53(3), 401-429.

Cotton, W. R., Weaver, J. F., and Beitler, B. A. (1995). "An Unusual Summertime Downslope Wind Event in Fort-Collins, Colorado, on 3 July 1993." Weather Forecast, 10(4), 786-797.

Cucchi, V., Meredieu, C., Stokes, A., Berthier, S., Bert, D., Najar, M., Denis, A., and Lastennet, R. (2004). "Root anchorage of inner and edge trees in stands of Maritime pine (Pinus pinaster Ait.) growing in different podzolic soil conditions." Trees-Struct Funct, 18(4), 460-466.

Davis, G., and Xiong, H. (2007). Access to destinations: travel time estimation on arterials, Minnesota Department of Transportation.

Deng, L., and Cai, C.S. (2010). "Development of dynamic impact factor for performance evaluation of existing multi-girder concrete bridges." Engineering Structures, 32(1), 21-31.

Deng, L., Yu, Y., Zou, Q.L., and Cai, C.S. (2015). "State-of-the-art Review on Dynamic Impact Factors of Highway Bridges." Journal of Bridge Engineering (ASCE), 20(5), 04014080.

Dupuy, L., Fourcaud, T., and Stokes, A. (2005). "A numerical investigation into the influence of soil type and root architecture on tree anchorage." Plant Soil, 278(1-2), 119-134.

Duryea, M, and Kampf, E. (2007). "Wind and Trees: Lessons Learned from Hurricanes." University of Florida FOR-118, Gainesville.

Edrissi, A., Nourinejad, M., Roorda, M.J. (2015). "Transportation network reliability in emergency response." Transportation Part E: 80, 56-73.

Elefteriadou, L. (2014). An introduction to traffic flow theory. New York: Springer.

Esser, J., and Schreckenberg, M. (1997). "Microscopic simulation of urban traffic based on cellular automata." Int J Mod Phys C, 8(5), 1025-1036.

Evans, L. (2004). Traffic safety, Science Serving Society, Bloomfield Hills, MI.

Fambro, D., Fitzpatrick, K., and Koppa, R. (1997). "NCHRP Report 400: Determination of Stopping Sight Distances." Transportation Research Board, National Research Council, Washington, DC.

Fei, L., Zhu, H. B., and Han, X. L. (2016). "Analysis of traffic congestion induced by the work zone." Physica A, 450, 497-505.

Fotouhi, H., Moryadee, S. and Miller-Hooks, E. (2017). "Quantifying the resilience of an urban traffic-electric power coupled system." Reliability Engineering and System Safety, 613, 79-94.

Fukui, M., and Ishibashi, Y. (1996). "Traffic flow in 1D cellular automaton model including cars moving with high speed." J Phys Soc Jpn, 65(6), 1868-1870.

Gardiner, B., Peltola, H., and Kellomaki, S. (2000). "Comparison of two models for predicting the critical wind speeds required to damage coniferous trees." Ecol Model, 129(1), 1-23.

Gaspar, P., Szaszi, I., and Bokor, J. (2004). "The design of a combined control structure to prevent the rollover of heavy vehicles." Eur J Control, 10(2), 148-162.

Gaspar, P., Szaszi, I., and Bokor, J. (2005). "Reconfigurable control structure to prevent the rollover of heavy vehicles." Control Eng Pract, 13(6), 699-711.

Gastaldi, M., and Rossi, R. (2011). "A methodology for calibrating road link travel time functions using data from driving simulator experiments." State of the Art in the European Quantitative Oriented Transportation and Logistics Research, 2011, 20, 656-665.

Goretti, A., and Sarli, V. (2006). "Road network and damaged buildings in urban areas: Short and long-term interaction." B Earthq Eng, 4(2), 159-175.

Greenshields, B. D. (1934). "The photographic method of studying traffic behavior." Proceedings of the 13th annual meeting of the highway research board, 382–399.

Greenshields, B. D. (1935). "A study in highway capacity." Proceedings of the 14th annual meeting of the highway research board, 448-477.

Guo, W. H., and Xu, Y. L. (2006). "Safety analysis of moving road vehicles on a long bridge under crosswind." J Eng Mech-Asce, 132(4), 438-446.

Hafstein, S. F., Chrobok, R., Pottmeier, A., Schreckenberg, M., and Mazur, F. C. (2004). "A high-resolution cellular automata traffic simulation model with application in a freeway traffic information system." Comput-Aided Civ Inf, 19(5), 338-350.

Hamdar, S. H. (2004). "Towards modeling driver behavior under extreme conditions." Master's Thesis, University of Maryland.

Horácek, P. (2003). "Introduction to Tree Statics & Static Assessment." Tree statics and dynamics seminar, interpreting the significance of factors affecting tree structure & health, Westonbirt, UK.

Hou, G. Y., and Chen, S. R. (2019a). "An improved cellular automaton model for work zone traffic simulation considering realistic driving behavior". Journal of the Physical Society of Japan, 88(8), 084001.

Hou, G. Y., and Chen, S. R. (2019b). "Probabilistic modeling of disrupted infrastructures due to fallen trees subjected to extreme winds in urban community". Natural Hazards, under review.

Hou, G. Y., Chen, S. R., and Bao, Y. L. (2019). "Development of travel time functions for disrupted urban arterials with microscopic traffic simulation". Transportation Science, under review.

Hou, G. Y., Chen, S. R., and Chen, F. (2019). "Framework of simulation-based vehicle safety performance assessment of highway system under hazardous driving conditions". Transportation Research Part C: Emerging Technologies, 105, 23-36.

Hou, G. Y., Chen, S. R., and Han, Y. (2019). "Traffic performance assessment methodology of degraded roadway links following hazards." Journal of Aerospace Engineering, ASCE, 32(5), 04019055.

Hou, G. Y., Chen, S. R., Zhou, Y. F. and Wu, J. (2017). "Framework of microscopic traffic flow simulation on highway infrastructure system under hazardous driving conditions." Sustainable and resilience infrastructure, 2 (3), 136-152.

Hsu, C. C., and Chiou, Y. C. (2018). "A Modified Cellular Automaton Model for Accounting for Traffic Behaviors during Signal Change Intervals." J Adv Transport.

Huang, D. W., and Huang, W. N. (2002). "The influence of tollbooths on highway traffic." Physica A, 312(3-4), 597-608.

Immers, L. H., and Logghe, S. (2002). Traffic flow theory, lecture notes of the course basics of traffic engineering (Katholieke Universiteit Leuven, Belguim)

Jia, B., Jiang, R., and Wu, Q. S. (2003). "The traffic bottleneck effects caused by the lane closing in the cellular automata model." Int J Mod Phys C, 14(10), 1295-1303.

Kajalic, J., Celar, N., and Stankovic, S. (2018). "Travel Time Estimation on Urban Street Segment." Promet-Zagreb, 30(1), 115-120.

Kang, W. H., Song, J. H., and Gardoni, P. L. (2008). "Matrix-based system reliability method and applications to bridge networks." Reliab Eng Syst Safe, 93(11), 1584-1593.

Kerner, B. S., Klenov, S. L., and Wolf, D. E. (2002). "Cellular automata approach to three-phase traffic theory." J Phys a-Math Gen, 35(47), 9971-10013.

Kim, S. J., Yoo, C. H., and Kim, H. K. (2016). "Vulnerability assessment for the hazards of crosswinds when vehicles cross a bridge deck." J Wind Eng Ind Aerod, 156, 62-71.

Knospe, W., Santen, L., Schadschneider, A., and Schreckenberg, M. (2000). "Towards a realistic microscopic description of highway traffic." J Phys a-Math Gen, 33(48), L477-L485.

Kocatepe, A., Ulak, M. B., Kakareko, G., Ozguven, E. E., Jung, S., and Arghandeh, R. (2018). "Measuring the accessibility of critical facilities in the presence of hurricane-related roadway closures and an approach for predicting future roadway disruptions." Nat Hazards, 1-21.

Kucharski, R., and Drabicki, A. (2017). "Estimating Macroscopic Volume Delay Functions with the Traffic Density Derived from Measured Speeds and Flows." J Adv Transport.

Kurata, S., and Nagatani, T. (2003). "Spatio-temporal dynamics of jams in two-lane traffic flow with a blockage." Physica A, 318(3-4), 537-550.

Laefer, D. F., and Pradhan, A. R. (2006). "Evacuation route selection based on tree-based hazards using light detection and ranging and GIS." J Transp Eng-Asce, 132(4), 312-320.

Lan, L. W., and Chang, C. W. (2005). "Inhomogeneous cellular automata modeling for mixed traffic with cars and motorcycles." J Adv Transport, 39(3), 323-349.

Lan, L. W., Chiou, Y. C., Lin, Z. S., and Hsu, C. C. (2009). "A refined cellular automaton model to rectify impractical vehicular movement behavior." Physica A, 388(18), 3917-3930.

Larraga, M. E., and Alvarez-Icaza, L. (2010). "Cellular automaton model for traffic flow based on safe driving policies and human reactions." Physica A, 389(23), 5425-5438.

Larraga, M. E., del Rio, J. A., and Schadschneider, A. (2004). "New kind of phase separation in a CA traffic model with anticipation." J Phys a-Math Gen, 37(12), 3769-3781.

Laval, J. A., and Leclercq, L. (2010). "A mechanism to describe the formation and propagation of stop-and-go waves in congested freeway traffic." Philos T R Soc A, 368(1928), 4519-4541.

Lavoie, S., Ruel, J. C., Bergeron, Y., and Harvey, B. D. (2012). "Windthrow after group and dispersed tree retention in eastern Canada." Forest Ecol Manag, 269, 158-167.

Lee, H. K., Barlovic, R., Schreckenberg, M., and Kim, D. (2004). "Mechanical restriction versus human overreaction triggering congested traffic states." Phys Rev Lett, 92(23).

Li, W., Wang, F., and Bell, S. (2007). "Simulating the sheltering effects of windbreaks in urban outdoor open space." J Wind Eng Ind Aerod, 95(7), 533-549.

Li, X. B., Wu, Q. S., and Jiang, R. (2001). "Cellular automaton model considering the velocity effect of a car on the successive car." Phys Rev E, 64(6).

Li, X. G., Jia, B., Gao, Z. Y., and Jiang, R. (2006). "A realistic two-lane cellular automata traffic model considering aggressive lane-changing behavior of fast vehicle." Physica A, 367, 479-486.

Li, X., Li, X. G., Xiao, Y., and Jia, B. (2016). "Modeling mechanical restriction differences between car and heavy truck in two-lane cellular automata traffic flow model." Physica A, 451, 49-62.

Lu, C. X. (2010). "A Travel Time Estimation for Planning Models Considering Signalized Intersections." Ite J, 80(10), 34-39.

Lu, Z. Y., Meng, Q., and Gomes, G. (2016). "Estimating link travel time functions for heterogeneous traffic flows on freeways." J Adv Transport, 50(8), 1683-1698.

Ma, L., Han, W. S., Ji, B. H., and Liu, J. X. (2015). "Probability of Overturning for Vehicles Moving on a Bridge Deck in a Wind Environment Considering Stochastic Process Characteristics of Excitations." J Perform Constr Fac, 29(1), 04014034.

Mattsson L.G., Jenelius E. (2015). "Vulnerability and resilience of transport systems – a discussion of recent research." Transp Res Part A Policy Pract, 81:16–34.

McPherson, E. G., van Doorn, N. S., and Peper, P. J. (2016). "Urban tree database and allometric equations." General Technical Report PSW-253, U.S. Department of Agriculture, Forest Service, Pacific Southwest Research Station, Albany, CA.

Meng, Q., and Weng, J. X. (2011). "An improved cellular automata model for heterogeneous work zone traffic." Transport Res C-Emer, 19(6), 1263-1275.

Mitchell, J. K., Devine, N., and Jagger, K. (1989). "A Contextual Model of Natural Hazard." Geogr Rev, 79(4), 391-409.

Moses, R., Mtoi, E., Ruegg, S., and McBean, H. (2013). Development of speed models for improving travel forecasting and highway performance evaluation, Florida State University.

Mtoi, E. T., and Moses, R. (2014). "Calibration and evaluation of link congestion functions: applying intrinsic sensitivity of link speed as a practical consideration to heterogeneous facility types within urban network." Journal of Transportation Technologies, 4(02), 141.

Muller, S., and Schiller, C. (2015). "Improvement of the volume-delay function by incorporating the impact of trucks on traffic flow." Transport Plan Techn, 38(8), 878-888.

Nagel, K., and Schreckenberg, M. (1992). "A Cellular Automaton Model for Freeway Traffic." J Phys I, 2(12), 2221-2229.

Nassab, K., Schreckenberg, M., Boulmakoul, A., and Ouaskit, S. (2006). "Effect of the lane reduction in the cellular automata models applied to the two-lane traffic." Physica A, 369(2), 841-852.

O'Connor, A., and O'Brien, E. (2005). "Mathematical traffic load modeling and factors influencing the accuracy of predicted extremes." Can. J. Civ. Eng., 32(1), 270–278.

Oketch, T., Delsey, M., and Robertson, D (2004). "Evaluation of Performance of Modern Roundabouts Using Paramics Microsimulation Model." TAC Conference, Quebec City, Canada.

Ouyang, M. (2014). "Review on modeling and simulation of interdependent critical infrastructure systems." Reliability Engineering and System Safety, 121, 43-60.

Peltola, H., Kellomaki, S., Vaisanen, H., and Ikonen, V. P. (1999). "A mechanistic model for assessing the risk of wind and snow damage to single trees and stands of Scots pine, Norway spruce, and birch." Can J Forest Res, 29(6), 647-661.

Peper, P. J., Alzate, C. P., McNeil, J. W., and Hasherni, J. (2014). "Allometric equations for urban ash trees (Fraxinus spp.) in Oakville, Southern Ontario, Canada." Urban for Urban Gree, 13(1), 175-183.

Pottmeier, A., Barlovic, R., Knospe, W., Schadschneider, A., and Schreckenberg, M. (2002). "Localized defects in a cellular automaton model for traffic flow with phase separation." Physica A, 308(1-

4), 471-482.

Poulos, H. M., and Camp, A. E. (2010). "Decision Support for Mitigating the Risk of Tree Induced Transmission Line Failure in Utility Rights-of-Way." Environ Manage, 45(2), 217-226.

Poulos, H. M., and Camp, A. E. (2011). "Mapping Threats to Power Line Corridors for Connecticut Rights-of-Way Management." Environ Manage, 47(2), 230-238.

Rajeswaran, S., and Rajasekaran, S. (2013). "Modeling and Simulation of Traffic Flow Using Cellular Automata." International Journal of Mathematical and Computer Modelling, 18(1), 1103-1108.

Ross, R. J. (2010). "Wood handbook: Wood as an engineering material." Forest Products Laboratory, Madison, Wisconsin.

Sampson, D. J. M. (2000). "Active roll control of articulated heavy vehicles." Ph.D. thesis, University of Cambridge, Cambridge, U.K.

Shin, J., and Lee, I. (2014). "Reliability-Based Vehicle Safety Assessment and Design Optimization of Roadway Radius and Speed Limit in Windy Environments." J Mech Design, 136(8), 081006.

Shin, J., and Lee, I. (2015). "Reliability analysis and reliability-based design optimization of roadway horizontal curves using a first-order reliability method." Eng Optimiz, 47(5), 622-641.

Simu, E., and Miyata, T. (2006). "Design of buildings and bridges for wind a practical guide for ASCE-7 standard users and designers of special structures." John Wiley & Sons.

Snaebjornsson, J. T., Baker, C. J., and Sigbjornsson, R. (2007). "Probabilistic assessment of road vehicle safety in windy environments." J Wind Eng Ind Aerod, 95(9-11), 1445-1462.

Sullivan, J., Aultman-Hall, L. and Novak, D. (2009). "A review of current practice in network disruption analysis and an assessment of the ability to account for isolating links in transportation networks." Transportation Letters, 1:4, 271-280.

Tamima, U., and Chouinard, L. (2017). "Systemic Seismic Vulnerability of Transportation Networks and Emergency Facilities." J Infrastruct Syst, 23(4).

Tian, Z. Z., Urbanik, T., Engelbrecht, R., and Balke, K. (2002). "Variations in capacity and delay estimates from microscopic traffic simulation models." Transportation Research Record 1802, Transportation Research Board, Washington, D.C., 23-31.

Transportation Research Board, National Academies (2010). Highway capacity manual 2010. Transportation Research Board, National Academies, Washington, DC.

Treiber M., and Kesting A. (2013). Traffic Flow Dynamics: Data, Models and Simulation, Springer.

Wang, B., and Xu, Y. L. (2015). "Safety analysis of a road vehicle passing by a bridge tower under crosswinds." J Wind Eng Ind Aerod, 137, 25-36.

Wang, B., Xu, Y. L., and Li, Y. L. (2016). "Nonlinear Safety Analysis of a Running Road Vehicle under a Sudden Crosswind." J Transp Eng, 142(2), 04015043.

Wang, R., Liu, M., Kemp, R., and Zhou, M. (2007). "Modeling driver behavior on urban streets." Int J Mod Phys C, 18(5), 903-916.

Weng, J. X., and Meng, Q. (2011). "Modeling speed-flow relationship and merging behavior in work zone merging areas." Transport Res C-Emer, 19(6), 985-996.

Westfall, J. A., and Scott, C. T. (2010). "Taper Models for Commercial Tree Species in the Northeastern United States." Forest Sci, 56(6), 515-528.

Xi, J. F., Liu, H. Z., Cheng, W., Zhao, Z. H., and Ding, T. Q. (2014). "The Model of Severity Prediction of Traffic Crash on the Curve." Math Probl Eng., 832723.

Xie, D., and Zhao, X. "Cellular Automaton Modeling with Timid and Aggressive Driving Behavior." ICTIS 2013: Improving Multimodal Transportation Systems-Information, Safety, and Integration, ASCE, Wuhan, China.

Xu, Y. L., and Guo, W. H. (2003). "Dynamic analysis of coupled road vehicle and cable-stayed bridge systems under turbulent wind." Eng Struct, 25(4), 473-486.

Yamg, M. L., Liu, Y. G., and You, Z. S. (2007). "A new cellular automata model considering finite deceleration and braking distance." Chinese Phys Lett, 24(10), 2910-2913.

You, K. S., Sun, L., and Gu, W. J. (2012). "Reliability-Based Risk Analysis of Roadway Horizontal Curves." J Transp Eng-ASCE, 138(8), 1071-1081.

Yun, S., White, W. W., Lamb, D. R., and Wu, Y. Q. (2005). "Accounting for the impact of heavy truck traffic in volume-delay functions in transportation planning models." Planning and Analysis 2005(1931), 8-17.

Zamith, M., Leal-Toledo, R. C. P., Clua, E., Toledo, E. M., and de Magalhaes, G. V. P. (2015). "A new stochastic cellular automata model for traffic flow simulation with drivers' behavior prediction." J Comput Sci-Neth, 9, 51-56.

Zanini, M. A., Faleschini, F., Zampieri, P., Pellegrino, C., Gecchele, G., Gastaldi, M., and Rossi, R. (2017). "Post-quake urban road network functionality assessment for seismic emergency management in historical centres." Struct Infrastruct E, 13(9), 1117-1129.

Zhang, X., and Waller, S. T. (2018). "Link performance functions for high occupancy vehicle lanes of freeways." Transport-Vilnius, 33(3), 657-668.

Zhao, H. T., Nie, C., Li, J. R., and Wei, Y. A. (2016). "A two-lane cellular automaton traffic flow model with the influence of driver, vehicle and road." Int J Mod Phys C, 27(02), 1650018.

Zhou, Y. F., and Chen, S. R. (2015a). "Dynamic Simulation of a Long-Span Bridge-Traffic System Subjected to Combined Service and Extreme Loads." J Struct Eng, 141(9).

Zhou, Y. F., and Chen, S. R. (2015b). "Fully coupled driving safety analysis of moving traffic on long-span bridges subjected to crosswind." J Wind Eng Ind Aerod, 143, 1-18.

Zhu, H. B., Lei, L., and Dai, S. Q. (2009). "Two-lane traffic simulations with a blockage induced by an accident car." Physica A, 388(14), 2903-2910.

CURRICULUM VITAE

Guangyang Hou

Education

Ph.D. Civil Engineering, 2014-2019
Colorado State University, Fort Collins, CO
Dissertation title: Multi-scale traffic performance modeling of transportation systems subjected to multiple hazards
Advisor: Professor Suren Chen

M.S. Civil Engineering, 2008-2011
Southwest Jiaotong University, Chengdu, China
Thesis title: Aerostatic and aerodynamic stability of super-long-span suspension bridges
Advisor: Professor Yongle Li

B.Eng. Civil Engineering, 2004-2008
Zhengzhou University, Zhengzhou, China

Publications

- Hou, G. Y., and Chen, S. R. (2019a). "An improved cellular automaton model for work zone traffic simulation considering realistic driving behavior". Journal of the Physical Society of Japan, 88(8), 084001.
- Hou, G. Y., and Chen, S. R. (2019b). "Probabilistic modeling of disrupted infrastructures due to fallen trees subjected to extreme winds in urban community". Natural Hazards, under review.
- Hou, G. Y., Chen, S. R., and Bao, Y. L. (2019). "Development of travel time functions for disrupted urban arterials with microscopic traffic simulation". Transportation Science, under review.
- Hou, G. Y., Chen, S. R., and Chen, F. (2019). "Framework of simulation-based vehicle safety performance assessment of highway system under hazardous driving conditions". Transportation Research Part C: Emerging Technologies, 105, 23-36.
- Hou, G. Y., Chen, S. R., and Han, Y. (2019). "Traffic performance assessment methodology of degraded roadway links following hazards." Journal of Aerospace Engineering, ASCE, 32(5), 04019055.
- Hou, G. Y., Chen, S. R., Zhou, Y. F. and Wu, J. (2017). "Framework of microscopic traffic flow simulation on highway infrastructure system under hazardous driving conditions." Sustainable and resilience infrastructure, 2 (3), 136-152.